Electro- and photo-production of muon pairs with μCLAS12: Double Deeply Virtual Compton Scattering, Timelike Compton Scattering, and J/ψ production

-

A Proposal to PAC53

N. Baltzell,* T. Cao, R. De Vita, L. Elouadrhiri, K. Gnanvo, F. Hauenstein, V. Kubarovsky,* R. Paremuzyan,* B. Raydo, S. Stepanyan,† R. Tyson, M. Ungaro, and X. Way

Thomas Jefferson National Accelerator Facility, Newport News, Virginia 23606

S. Niccolai,* E. Voutier, J. S. Alvarado, and M. Hoballah

Université Paris-Saclay, CNRS/IN2P3, IJCLab, 91405 Orsay, France

P. Chatagnon,* M. Defurne, and F. Bossù

IRFU, CEA, Université Paris-Saclay, F-91191 Gif-sur-Yvette, France

M. Bondi*

Instituto Nazionale di Fisica Nucleare

E. Cline, S. Frantzen, M. Kerr, R. Milner, Y. Wang, and N. Wuerfel

Massachusetts Institute of Technology, Cambridge, MA

D. Glazier and B. McKinnon

Glasgow University, Glasgow, Scotland

N. Liyanage and H. Nguyen

University of Virginia, Charlottesville, VA 22904

C. Fogler and M. Hattawy

Old Dominion University, Norfolk, Virginia 23529

S. Schadmand

GSI Helmholtzzentrum fur Schwerionenforschung GmbH

L. El Fassi

Mississippi State University

A. Vossen and Z. Zhao

Duke University, Durham, NC 27708-0305

P. Nadel-Turonski

University of South Carolina, Columbia, South Carolina 29208

A. D'Angelo

Istituto Nazionale di Fisica Nucleare Sezione di Roma Tor Vergata, Rome Italy

S. Diehl

II. Physikalisches Institut der Universität Giessen, 35392 Giessen, Germany

N. Dashyan, D. Martiryan, and H. Voskanyan

Artem Alikhanian National Laboratory, Yerevan, Armenia

M. Arratia

University of California Riverside, Riverside, California 92521

A. Schmidt

George Washington University, Washington, DC 20052

H.S. Jo

Kyungpook National University, Daegu 41566, Republic of Korea

(Dated: April 10, 2025)

Abstract

The CEBAF Large Acceptance Spectrometer (CLAS12) at Jefferson Lab continues to excel in a diverse physics program aimed at unraveling the internal structure of nucleons and nuclei. As significant scientific data continues to emerge, it becomes increasingly apparent that there are exciting scientific opportunities beyond the current capabilities of CLAS12. Building on the initial concept presented in LOI2-16-004 to PAC44, this proposal outlines a comprehensive set of measurements to explore the nucleon's quark-gluon structure using di-muon electro- and photo-production. Our primary focus lies on Double Deeply Virtual Compton Scattering (DDVCS). The large-acceptance, high-luminosity detector proposed for DDVCS enables an expanded research program, including studies of electro- and photo-production of vector mesons—particularly near-threshold J/ψ production—and high-statistics measurements of Timelike Compton Scattering (TCS).

To avoid ambiguities and anti-symmetrization issues, we will study DDVCS and vector meson production in the reaction $ep \to e'p'\gamma^\star/V \to e'\mu^-\mu^+(p')$. The TCS studies will follow the CLAS12 approach and use the reaction $ep \to p'\mu^-\mu^+(e')$. Essential requirements for conducting these measurements include high luminosity, a large acceptance detector, and excellent muon detection and identification. We envisioned an upgrade to CLAS12 to operate at significantly higher luminosities, $\geq 10^{37}$ cm^{-2} sec^{-1}. The main elements of the upgrade include replacing the CLAS12 high-threshold Cherenkov counter (HTCC) with a calorimeter and tungsten shield and enhancing the central and forward vertex tracking systems with high-rate capabilities. By converting the CLAS12 forward detector into a muon spectrometer (μCLAS12), employing a fast calorimeter for electron detection, and utilizing available high-intensity electron beams, μCLAS12 will be one of the unique detectors to carry out the proposed measurements (another detector being the planned SoLID detector in Hall A).

For the CLAS review committee: The proposal is in good shape, but we aim to improve it further. Below is a list of items we are still actively working on, and changes will be included in the next version of the proposal:

- complete the cost estimate for the upgrade to μCLAS12,
- continue optimization of the shield to lower rates in DC,
- find an alternative scintillator counter solution for the recoil detector as CND appears unsuitable,
- perform studies of μ/π separation with 30 cm lead shield,
- complete studies of extraction of the DDVCS $\cos\phi$ term using subtraction of BH contribution from the measured asymmetry.

* Co-spokesperson

† Contact-spokesperson: stepanya@jlab.org

CONTENTS

I. INTRODUCTION

The primary thrust of the 12 GeV science program and the future EIC lies in exploring nuclear *femtography* facilitated by the framework of Generalized Parton Distributions (GPDs) [1–4]. GPDs are universal non-perturbative objects, entering the description of hard exclusive electroproduction processes and greatly expanding the scope of the physics of traditional elastic form factors and PDFs. The program for studying GPDs with the JLAB 12 GeV facilities encompasses measurements of spin (beam/target) observables and cross sections in Deeply Virtual Exclusive Processes (DVEP) [5]. Among these processes, the Deeply Virtual Compton Scattering (DVCS) reaction, where the virtual photon generated by the incoming lepton is transformed into a real photon after interacting with a parton from the nucleon [1–3] stands out as the most straightforward and cleanest reaction for accessing GPDs. A wealth of data on DVCS has been produced and published since the early 2000s with 6 GeV [6–12] and recently from 12 GeV experiments [13, 14] at JLAB. Additionally, experimental studies of the second Compton process, Timelike Compton Scattering (TCS) [15–18], where the incoming photon is real, and the outgoing photon has large timelike virtuality, have already begun, and the first results on angular and beam helicity asymmetries have been published [19].

The fundamental limitation of these measurements is that they can access only two of the three variables, x, ξ, and t, which define the GPDs. Here, x is the quark internal momentum fraction, ξ is the longitudinal fraction of the momentum transfer (the skewness parameter), and t is the squared four-momentum transfer. For Compton reactions, the experimental observables depend on Compton Form Factors (CFFs), which encompass integrals of GPDs over x (representing the real part of Compton amplitude) or GPDs evaluated at a specific kinematical point, $x = \pm\xi$, (the imaginary part of Compton amplitude). This poses a significant challenge for inferring GPDs from DVCS/TCS data [20, 21]. As demonstrated in [22], extracting GPDs from CFFs is ambiguous due to the existence of a large class of functions known as shadow GPDs (SGPDs) with a null CFF and a null forward limit at a given scale, contributing to the solutions of any GPD extraction. Although the QCD evolution of GPDs (SGPDs) will limit the class of functions that can contribute [23], an experimental approach to the *deconvolution problem* is required, that is, acquiring data from other processes sensitive to the full kinematic dependence of GPDs.

Double Deeply Virtual Compton Scattering (DDVCS) [24–26], characterized by large virtualities of both incoming and outgoing photons, provides direct access to GPDs at $x \neq \pm\xi$ at leading order in α_s (LO), thereby offering invaluable insights into the x-dependence of GPDs, inaccessible otherwise. However, it is a challenging reaction to measure. The cross-section of DDVCS is about three orders of magnitude smaller than the DVCS cross-section. In addition, to eliminate the ambiguity of like leptons, beam and decay, and anti-symmetrization issues, the outgoing timelike photon must be reconstructed through the di-muon decays. Like DVCS and TCS, the Bethe-Heitler (BH) process will contribute to the same final state. Leveraging the interference of DDVCS and BH will enable us to map out GPDs extensively outside the $x = \pm\xi$ ridge.

Jefferson Lab at the luminosity frontier with large acceptance detectors is the only place where DDVCS can be measured. The CLAS12 detector [27] in Hall-B is particularly suited for such measurements. Here, we propose to study the electroproduction of muon pairs in the reaction $ep \to e'\mu^+\mu^-p'$, in a wide range of space-like and timelike virtualities of incoming and outgoing virtual photons, respectively. The primary focus of the upgrade involves converting the CLAS12 Forward Detector (FD) into a muon spectrometer by implementing heavy shielding at its entrance, in place of a High Threshold Cerenkov Counter (HTCC), to mitigate electromagnetic and hadronic backgrounds when the detector operates at luminosities $\geq 10^{37}$ cm^{-2} sec^{-1}. The shield will encompass a new $PbWO_4$ calorimeter that will be used to detect scattered electrons. We also envision a new tracking system for forward vertex tracking and recoil proton detection.

The di-muon final state provides an excellent setting to explore Timelike Compton Scattering (TCS) and vector meson production, explicitly emphasizing the J/ψ production near the threshold. These studies extend the existing JLAB program dedicated to TCS and J/ψ, which is currently underway. The initial experiments have yielded exciting new results, covering previously unexplored kinematic regions. In particular, the CLAS collaboration published pioneering experimental results on beam spin and angular asymmetries of TCS [19]. The GlueX collaboration [28, 29] and the Hall-C experiment E12-16-007 [30] have published the energy and the transferred momentum dependencies of the near-threshold J/ψ production, marking the first exploration of the proton's gluonic gravitational form factors (GFFs) and its mass-radius. We anticipate releasing results from CLAS12 experiments on J/ψ production in similar kinematic regions before the end of 2025. However, while data are being collected by ongoing 12 GeV experiments, both TCS and J/ψ measurements will be limited by statistics. For example, we anticipate approximately $\sim$ 2K J/ψ events from each of the ongoing programs, whereas, in the proposed DDVCS experiment, this number will be nearly 25 times higher. The high statistics data used for cross-sections and asymmetries extractions will provide the precision necessary for the aforementioned GPD deconvolution problem and for exploring nucleon GFF and mechanical properties. Finally, the J/ψ electro-production data will be used to search and study LHCb hidden charm pentaquarks where large statistics is imperative.

To summarize, we propose μCLAS12 to study the electro- and photo-production of $\mu^+\mu^-$ pairs using an 11 GeV longitudinally polarized electron beam, a liquid hydrogen target, and a modified CLAS12 detector in Hall-B. To perform the above-mentioned studies of DDVCS, TCS, and J/ψ production, we ask for a total of 245 days of beam time, for 200 days of production running with μCLAS12 at luminosity of $L = 10^{37}$ cm^{-2} sec^{-1}, a 30 days of low-luminosity calibration runs, and a 15 days for commissioning of μCLAS12.

II. PHYSICS MOTIVATION

Quantum Chromodynamics (QCD), the theoretical framework that describes the strong force that governs the interactions between quarks and gluons, is responsible for most of the mass we see in the universe. Yet, while we have made remarkable strides in understanding atoms and molecules, the breakdown of nucleons into their constituent quarks and gluons remains a daunting challenge. Electron scattering has played a pivotal role in our understanding of the momentum and spatial distributions of partons (quarks and gluons) within the nucleon, shedding light on its underlying quantum chromodynamic structure. For many decades, the measurements of elastic form factors (EFF) and parton distribution functions (PDFs) helped us to extract information separately on the shape of the nucleon in coordinate and momentum space, respectively, leaving us with an incomplete picture. The formalism of Generalized Parton Distributions (GPDs) offers a comprehensive framework to describe the internal structure of the nucleon in terms of quark and gluon degrees of freedom. GPDs generalize the concept of parton distribution functions (PDFs) and elastic form factors, providing a unified description of the nucleon's spatial and momentum structure. This new avenue allows us to see the nucleon's partonic picture in 3D and promises insights into the origin of the nucleon mass and spin.

A. The Generalized Parton Distributions and their properties

GPDs encode the probability amplitudes for finding a particular partonic configuration inside the nucleon and provide access to the transverse spatial distribution of partons and their longitudinal momentum distribution [31, 32]. The factorization theorem provides the basis for accessing GPDs experimentally through deeply virtual exclusive processes (DVEP), Compton scattering (CS), DVCS and TCS, and Deeply Virtual Meson Production (DVMP), as shown in Fig.1. In such processes, the scattering amplitude can be expressed as a convolution of perturbatively calculable complex-valued hard-scattering coefficients with the non-perturbative real-valued GPDs:

$$\mathcal{A} \sim \sum_q \int_{-1}^{1} dx\, C_q(x, \xi, Q^2) F^q(x, \xi, t), \tag{1}$$

where C_q are the hard-scattering coefficients, and $F^q(x, \xi, t)$ represents GPDs. Compton scattering with a large spacelike or timelike virtuality has long been recognized as a pivotal process within deep exclusive reactions in the experimental exploration of GPDs.

GPD is a function of three kinematic variables: the longitudinal momentum fraction x, defined

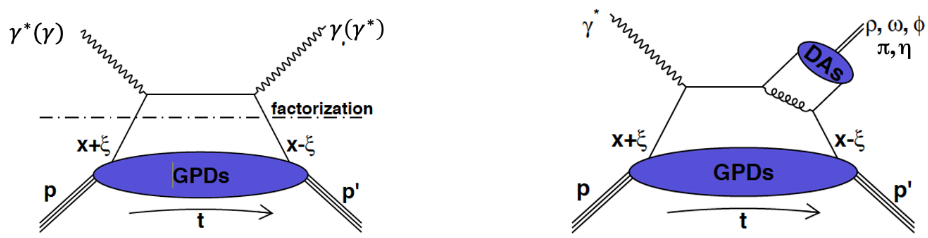

FIG. 1: The factorization concept for Compton scattering and deeply virtual meson production.

relative to the average nucleon momentum $P = (p+p')/2$. The skewness parameter ξ characterizes the difference in longitudinal momentum fractions between the incoming and outgoing partons $\xi = (p'-p)^+/(p'+p)^+$, and the invariant momentum transfer squared $t = (p'-p)^2$. They are defined through non-forward matrix elements of bilocal operators, connecting the initial and final nucleon states:

$$F(x,\xi,t) = \int \frac{dz^-}{4\pi} e^{ixP^+z^-} \langle p'|\bar{\psi}(-z/2)\gamma^+\psi(z/2)|p\rangle \tag{2}$$

where $F(x,\xi,t)$ represents the generalized parton distribution and $\psi(z)$ is the quark field operator.

At leading-twist, there are four chiral-even (parton helicity-conserving) GPDs - H^a, E^a, $\tilde{H}^a$, and $\tilde{E}^a$. Of the four off-forward parton distributions, H^a and $\tilde{H}^a$ conserve the nucleon helicity, while E^a and $\tilde{E}^a$ flip the nucleon helicity. The first moments of GPDs relate to elastic form factors:

$$\begin{aligned} &\int_{-1}^{1} dx H^a(x,\xi,t) = F_1^a(t), \qquad &&\int_{-1}^{1} dx E^a(x,\xi,t) = F_2^a(t), \\ &\int_{-1}^{1} dx \tilde{H}^a(x,\xi,t) = g_A^a(t), \qquad &&\int_{-1}^{1} dx \tilde{E}^a(x,\xi,t) = h_A^a(t), \end{aligned} \tag{3}$$

where $F_1(t)$ and $F_2(t)$ are the Dirac and Pauli form factors, and $g_A(t)$ and $h_A(t)$ are the axial-vector and pseudoscalar form factors of the nucleon. In the forward limit ($t \to 0$), the GPDs H and $\tilde{H}$ reduce to PDFs:

$$\begin{aligned} H^a(x,0,0) &= a(x) - \bar{a}(x), \\ \tilde{H}^a(x,0,0) &= \Delta a(x) - \Delta\bar{a}(x), \end{aligned} \tag{4}$$

Here the index (a) stands for quark spices and gluons.

Another remarkable property of GPDs is the connection to the form factors of the QCD energy-momentum tensor (EMT) (here we use notations from [33]):

$$\begin{aligned} \langle P'|T^{\mu\nu}_{q,g}|\rangle P\rangle = \bar{u}\left(P'\right)\Big[& A_{q,g}(t)\gamma^{(\mu}\bar{P}^{\nu)} + B_{q,g}(t)\bar{P}^{(\mu}i\sigma^{\nu)\alpha}\Delta_\alpha/2M \\ & + C_{q,g}(t)\left(\Delta^\mu\Delta^\nu - g^{\mu\nu}\Delta^2\right)/M + \bar{C}_{q,g}(t)g^{\mu\nu}M\Big]u(P)\ . \end{aligned} \tag{5}$$

The x-moments of the GPDs E and H play a specific role in defining the form factors A, B, and C:

$$\begin{aligned}\int_{-1}^{1} dx x H^a(x,\xi,t) &= A_a(t) + \xi^2 C_a(t),\\ \int_{-1}^{1} dx x E^a(x,\xi,t) &= B_a(t) - \xi^2 C_a(t),\end{aligned} \tag{6}$$

where the form factors A, B, and C (commonly referred to as gravitational form factors) define the mass distribution in the nucleon [34]:

$$G_m(t) = \left[M A_{q+g}(t) + B_{q+g}(t)\frac{t}{4M} - C_{q+g}(t)\frac{t}{M} \right]. \tag{7}$$

From which the mass radius can be constructed, $\langle r^2 \rangle_m = 6 \mid \frac{dG_m(t)/M}{dt} \mid_{t=0}$. The EMT form factors also offer crucial information about the proton spin carried by quarks and gluons [33]:

$$J_{q,g} = \frac{1}{2}[A_{q,g} + B_{q,g}]. \tag{8}$$

The form factors $C(t)$ (also referred to as D-term) and $\bar{C}(t)$ define pressure and shear force distributions inside the nucleon [35–37].

B. Compton scattering and GPDs

Deeply virtual Compton scattering (DVCS), denoting the exclusive electroproduction of a real photon $ep \to e'p'\gamma$, see Fig.2.(a), as initially proposed in [2–4], stands out as the primary avenue for probing GPDs. Experimental observables of DVCS are parameterized by Compton Form Factors (CFFs). GPDs enter CFFs as convolution integrals over a parton longitudinal momentum fraction x:

$$\mathcal{F}(\xi,t,Q^2) = \int dx F(\mp x,\xi,t)\left(\frac{1}{\xi - x + i\epsilon} \pm \frac{1}{\xi + x + i\epsilon}\right), \tag{9}$$

where, F is a generic GPD, and the top and bottom signs apply to the quark-helicity dependent and the quark-helicity independent GPDs, and $Q^2 = -q^2 = (e-e')^2$, where e and e' are incoming and outgoing electron four momenta.

At the leading twist, there are eight CFFs (four complex pairs) related to the four relevant GPDs, H, E, $\tilde{H}$, and $\tilde{E}$. The imaginary part of CFFs contains GPDs evaluated at a specific point $x = \pm\xi$ and are accessible in single spin asymmetry measurements:

$$\mathrm{Im}[\mathcal{F}] = i\pi \sum_q [F^q(\xi,\xi,t) \mp F^q(-\xi,\xi,t)], \tag{10}$$

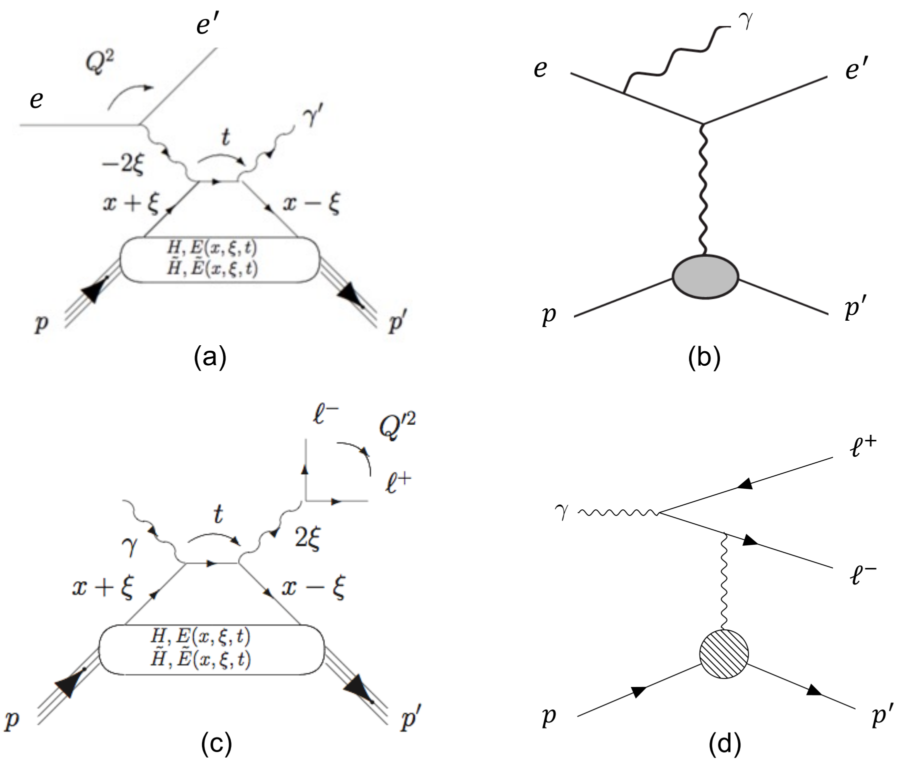

FIG. 2: Diagrams for Compton processes: (a) DVCS and (c) TCS processes, and accompanying Bethe-Heitler processes (b) and (d), respectively.

The real part of CFFs, accessible in cross-section or double spin asymmetry measurements, are defined as Cauchy principal value integrals of GPDs over x:

$$\mathrm{Re}[\mathcal{F}] = \mathcal{P}\int_{-1}^{1} dx \left(\frac{1}{\xi - x} \pm \frac{1}{\xi + x}\right) \sum_q [F^q(x,\xi,t) \mp F^q(-x,\xi,t)]. \tag{11}$$

In the experiment, one measures DVCS together with the Bethe-Heitler process (BH), where the photon emission is mediated by the electron, Fig. 2.(b). So the measured cross section is a coherent sum of two amplitudes, $\mathcal{T}_{DVCS}$ and $\mathcal{T}_{BH}$:

$$\sigma_{DVCS} = |\mathcal{T}_{BH}|^2 + |\mathcal{T}_{DVCS}|^2 + \mathcal{I}, \tag{12}$$

with the interference term defined as:

$$\mathcal{I} = \mathcal{T}_{BH}^* \mathcal{T}_{DVCS} + \mathcal{T}_{BH} \mathcal{T}_{DVCS}^*, \tag{13}$$

The $\mathcal{T}_{BH}$ depends on the nucleon FF and is fully calculable in QED, whereas the $\mathcal{T}_{DVCS}$ depends on CFFs in convolution with the nucleon FFs. In much of the JLAB kinematics, BH dominates the cross-section and poses a challenge to extracting CFF from cross-section measurements. Despite

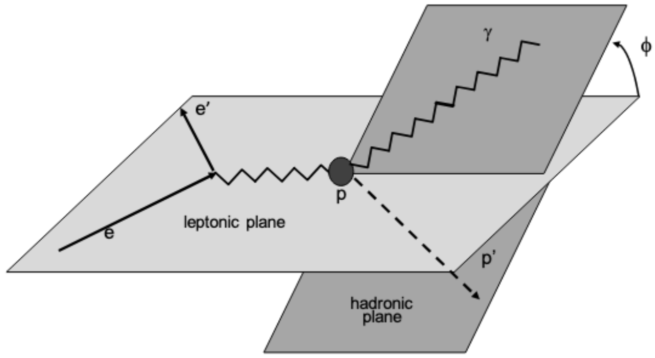

FIG. 3: Diagram of DVCS scattering planes. The angular harmonics of ϕ between the leptonic and hadronic planes project out the interference term of the scattering amplitude.

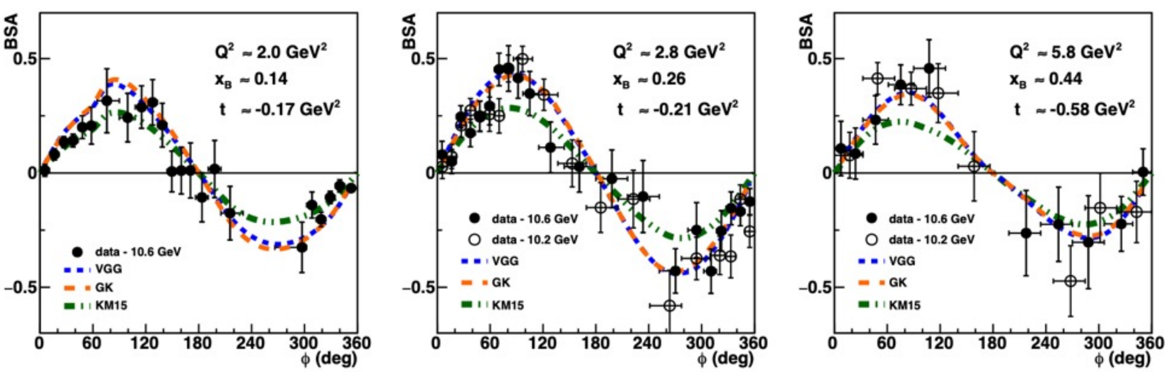

FIG. 4: Beam-spin asymmetries for bins only reachable with a 10 GeV electron beam, compared with the KM15, GK, and VGG GPD models.

its dominance, the interference between the BH and DVCS amplitudes provides a powerful tool for studying CFFs. The azimuthal angular dependencies of the interference term, accessible through spin (single or double) and lepton charge asymmetries, provide access to the linear combination of both the imaginary and real parts of the CFFs. Here, the azimuthal angle refers to the angle formed by the leptonic and hadronic planes, see Fig.3.

Various DVCS asymmetries and cross sections measured and published since the early 2000' (with JLab at 6 GeV [6–12], HERMES [38, 39], H1 [40], ZEUS [41], and COMPASS [42]) have so far provided the most extensive data set for studying GPDs experimentally. The JLAB 12 GeV program just started and produced the first results on DVCS [13, 14]. Both experiments produced more than 1000 points of helicity-dependent cross-section and asymmetries. In Fig.4, the beam spin asymmetries from [14] in two kinematic points are shown together with estimates with the KM15[43], GK[44], and VGG[45] GPD models. In contrast, Timelike Compton Scattering (TCS) has remained a subject of theoretical discourse [15, 17, 18] but has not been experimentally investigated until recently. In 2021, the CLAS collaboration at JLAB published the first-ever experimental results on the photon beam polarization asymmetry and the decay lepton angular asymmetries of TCS [19] using data obtained with the CLAS12 detector where a 10.6 GeV electron beam scattered off a hydrogen target. TCS mirrors DVCS in symmetry, featuring a real incoming photon and an outgoing photon with substantial timelike virtuality, $\gamma p \to p'\gamma^* \to p' l^+ l^-$, as shown in the diagram in Fig.2.(c). In TCS, the virtuality of the outgoing photon, denoted as $Q'^2 \equiv M^2(l^+l^-)$ (here $M(l^+l^-)$ stands for the invariant mass of the lepton pair) defines the hard scale. As in DVCS, the BH process, where the electron mediates lepton pair production (see Fig.2.(d)) contributes to the same final state and dominates the cross-section of exclusive lepton pair photoproduction. An essential feature of TCS is that the amplitudes for the Compton and Bethe-Heitler processes transform with opposite signs under the reversal of the lepton charge. Consequently, the interference term between TCS and BH in the cross-section is odd under the exchange of the l^+ and l^- momenta, while the individual contributions of the two are even. This property provides straightforward access to the real part of CFFs through the angular transformation of $\theta \to \pi + \theta$ and $\phi \to \pi - \phi$ of the decay leptons (see Fig.5) and, thus, the D-term in the parametrization of GPDs (this is similar to the lepton charge asymmetry in DVCS). On the other hand, the photon beam polarization asymmetry projects out the imaginary part of the Compton amplitude as the beam spin asymmetry in DVCS and tests the universality of GPDs. In Fig.6, the results obtained in [19] for both asymmetries and for a single kinematic point are shown as a function of transferred momentum squared t. The photon circular polarization asymmetry, $A_{\odot U}$, is in reasonable agreement with the predictions of GPD-based models that were tuned on the DVCS data supporting the universality of GPDs. The angular asymmetry, A_{FB}, is the first direct measurement of the real part of the VCS-BH interference term and shows a strong sensitivity to the D-term.

With experimental data flowing, the next crucial step is inferring information on GPDs from DVCS and TCS observables. The process is not straightforward. First, one has to extract CFFs from data and then obtain information on GPDs, primarily by constraining GPD models.

C. Inferring GPDs from experimental observables

Extracting CFFs from experimental observables, such as asymmetries and cross-sections, is a crucial first step in accessing GPDs. Several methodologies have been developed to extract CFFs. These methods involve analyzing observables under well-established theoretical frameworks

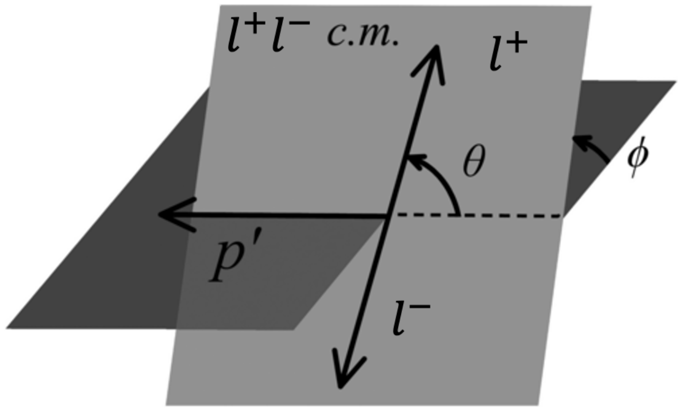

FIG. 5: Diagram of TCS scattering planes. Relevant angles for TCS θ and ϕ are, respectively, the angle between the leptonic plane (defined by the outgoing leptons momenta l^+ and l^-) and the hadronic plane (defined by the incoming and outgoing proton momenta p and p').

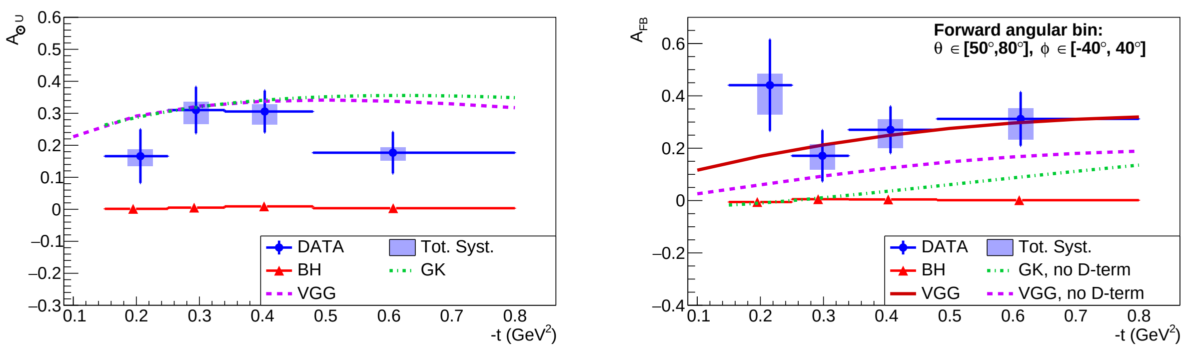

FIG. 6: The photon circular polarization (left) and forward-backward (right) asymmetries from [19]. A reasonable agreement of models with measured $A_{\odot U}$, the imaginary part of the Compton amplitude, points towards the universality of GPDs. The A_{FB} on the other hand is proportional to the real art of the Compton amplitude and shows sensitivity to the D-term.

incorporating the symmetries and kinematic dependencies specific to the scattering process.

A model-independent extraction of CFFs has been studied with local fits at specific kinematic points (x_B, t, Q^2) at which measurements are performed [46–52]. The advantage of local fits is their model-independence, as they directly measure the CFFs. This approach avoids biases introduced by specific GPD parametrizations and focuses solely on the experimental data. However, the drawback is that local fits do not inherently account for correlations across kinematic points or the global structure of GPDs, which can limit their scope for extracting comprehensive insights about the internal structure of hadrons.

Global fits [20, 50, 53, 54] aim to simultaneously describe all available data across the entire kinematic range. This approach uses a parameterized model for the GPDs, which implicitly defines the CFFs. The parameters of the GPD model are then optimized by fitting the entire dataset. Global fits offer several advantages: they provide a consistent description of the data, constrain the GPDs over a broader kinematic range, and often lead to smaller uncertainties due to the larger dataset used. However, there are challenges due to the complexity of the GPD parameterizations and the computational demands of the fitting procedure. Different theoretical models for GPDs exist, each with its own set of parameters that need to be determined through the global fit.

A promising approach in extracting CFFs involves using Artificial Neural Networks (ANNs) [55]. ANNs provide a flexible and model-independent way to parameterize CFFs by learning patterns directly from experimental data without imposing rigid functional forms. The works of M. Čuić, K. Kumerički, and A. Schäfer offer significant advancements in these techniques [56, 57]. They leverage global fits, neural networks, and advanced parameterizations to reconstruct CFFs from the measured data accurately. These approaches are particularly effective in reducing model dependence and ensuring compatibility with the constraints imposed by Quantum Chromodynamics (QCD).

The next step, inferring GPDs from CFFs, is a challenging task known as the deconvolution problem. The fundamental limitation is that observables in DVCS and TCS reactions can access only two of the three variables, x, ξ, and t, that define the GPDs. The variable x is integrated out in the convolution integrals, and CFFs do not contain it. This means there is no unique solution for going from CFFs to GPDs. Various GPD functions can explain experimental data at different scales, and experimental uncertainties will also limit filtering through various GPD models and parameters. As shown in Fig.7 from [58], two different GPD models have almost equal values for GPD H at $x = \xi$.

Moreover, recent studies of deconvolution have revealed the existence of a class of functions, shadow GPDs (SGPD) with a null CFF and a null forward limit at a given scale μ^2, that will contribute to solutions in the GPD extraction [22]. An example of SGPDs is shown in Fig.8 from [22]. The QCD evolution of GPDs in ξ and Q^2 can be used to exclude a large class of SGPDs [22, 23], and there is also a hope of the lattice QCD evaluation of the x dependence of GPDs [59]. Nevertheless, a process directly sensitive to the x dependence of GPDs is the only way to experimentally challenge the problem.

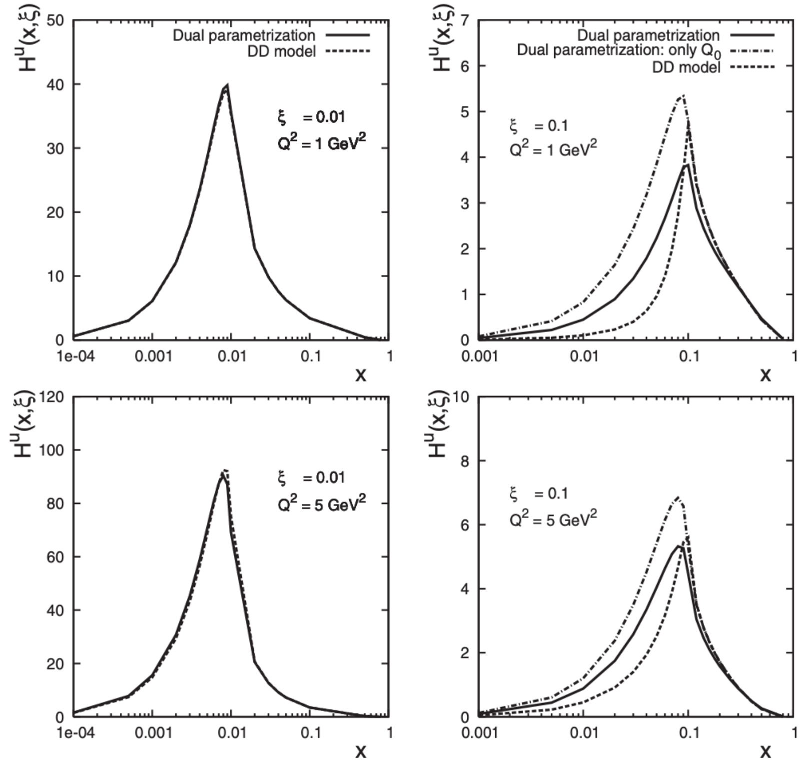

FIG. 7: The singlet GPD H^u as a function of x, ξ, and Q^2. The solid curves are dual parametrization; the dashed curve is a prediction of the DD model. See details in [58].

D. Double Deeply Virtual Compton Scattering

1. Overview

A significant limitation in existing measurements, such as DVCS or TCS, is their inability to fully decouple the three GPD variables x, ξ, and t. The observables in these processes can access GPDs at $x = \pm\xi$ point (imaginary part of CFF) or measure integrals of GPDs over x (the real part of CFF). In contrast, Double Deeply Virtual Compton Scattering (DDVCS) [24–26], where both the incoming and outgoing photons are virtual, introduces independent tunable scales via the spacelike, Q^2, and timelike $Q'^2 \equiv M^2(l^+l^-)$ virtualities, enabling the exploration of GPDs in the $x \neq \xi$ space.

The DDVCS process can be accessed in exclusive electro-production of lepton pairs:

$$ep \to e'p'\gamma^* \to e'p'l^+l^-. \tag{14}$$

At leading twist and leading α_s-order, DDVCS can be presented as the absorption of a spacelike photon by a parton inside the nucleon and emission of a timelike photon, which then decays to a

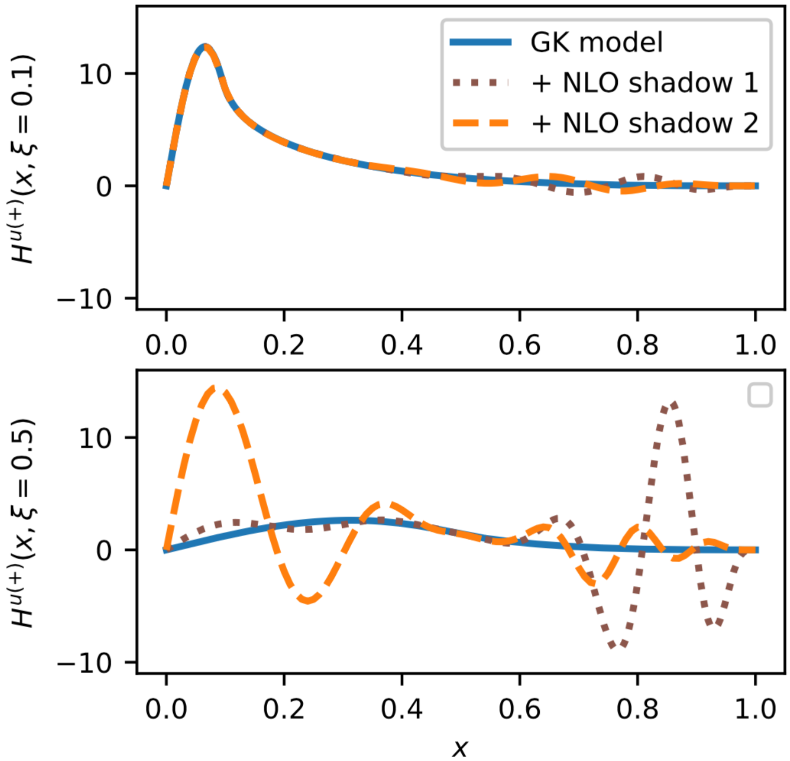

FIG. 8: The singlet GPD H^u as a function of x for $\xi = 0.1$ and 0.5, $-t = 0.5$ GeV^2, and $\mu_0^2 = 1$ GeV^2. The solid curves GK model with added two different SGPDs in dashed orange and dotted brown curves. See details in [22].

lepton pair, as shown in Fig.9.(a). The CFFs enter the DDVCS amplitude as convolution integrals over a parton longitudinal momentum:

$$\begin{aligned}\mathcal{F}(\xi', \xi, t) = \mathcal{P} \int dx \left(\frac{1}{\xi' - x} \pm \frac{1}{\xi' + x} \right) \sum_q [F^q(x, \xi, t) \mp F^q(-x, \xi, t)] \\ - i\pi \sum_q [F^q(\xi', \xi, t) \mp F^q(-\xi', \xi, t)].\end{aligned} \tag{15}$$

where the scaling variables, skewness (ξ) and the generalized Bjorken variable (ξ') (see Fig.9.(a)) are defined as:

$$\begin{aligned}\xi &= \frac{Q^2 + Q'^2}{2Q^2/x_B - Q^2 - Q'^2 + t}, \\ \xi' &= \frac{Q^2 - Q'^2 + t/2}{2Q^2/x_B - Q^2 - Q'^2 + t}.\end{aligned} \tag{16}$$

Varying the virtualities of the incoming (Q^2) and outgoing (Q'^2) photons, one can map out GPDs as a function of $x = \xi'$ and ξ, a yellow region in Fig.10, outside of the $x = \pm\xi$ ridge that DVCS and TCS offer. Note that for the case of DVCS, $Q'^2 = 0$, $\xi' \approx \xi$ (for $-t << Q^2$). For the case of TCS, $Q^2 = 0$, $\xi' \approx -\xi$ (for $-t << Q'^2$).

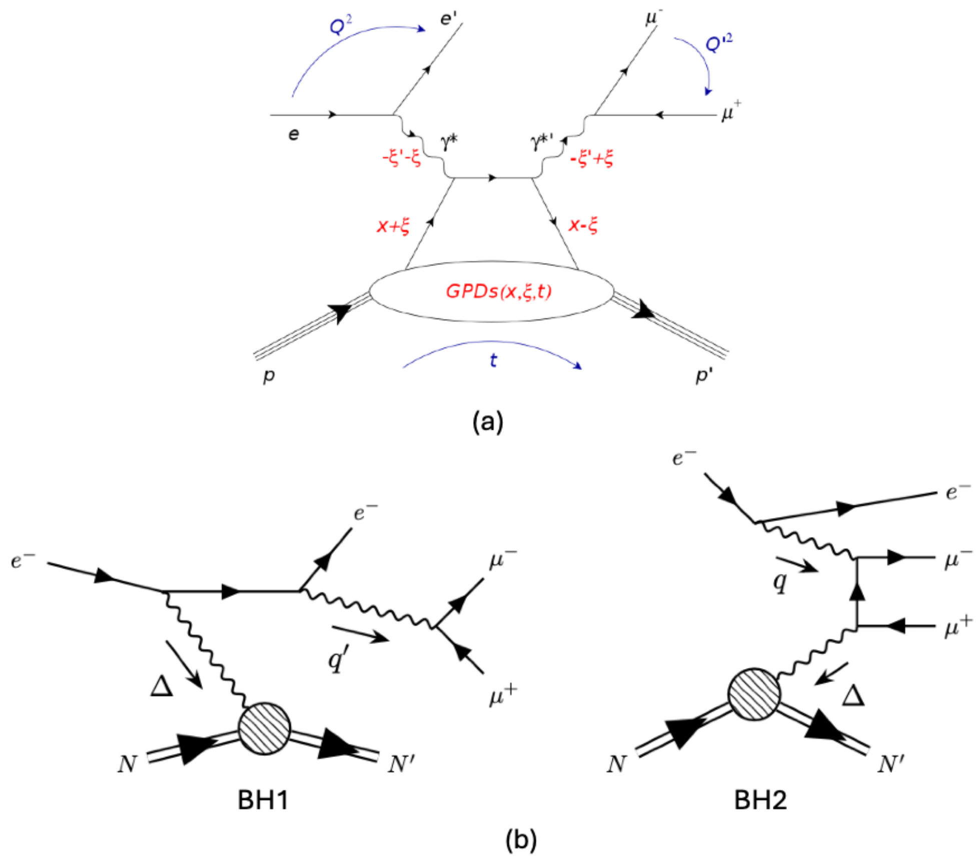

FIG. 9: Diagrams of DDVCS, (a), and BH processes, (b).

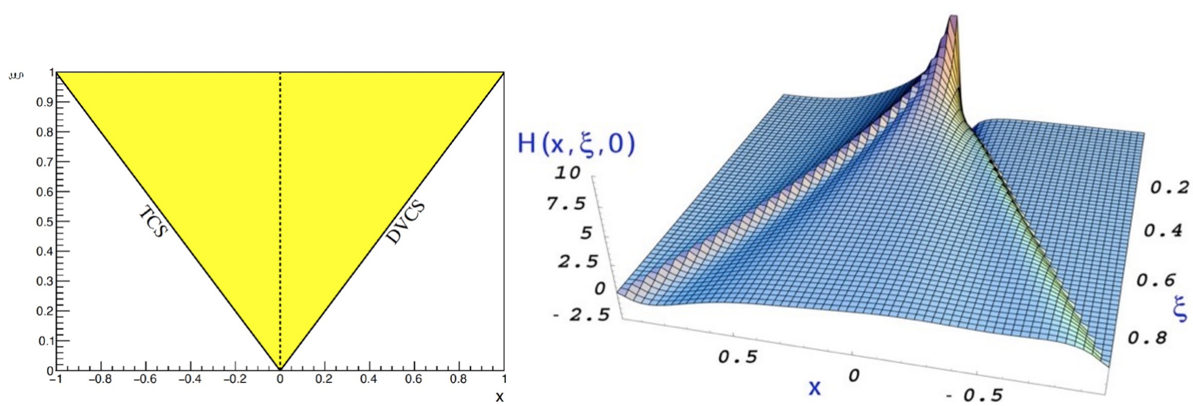

FIG. 10: On the left, the longitudinal momentum transfer ξ vs the longitudinal momentum fraction x for Compton scattering. The yellow region is accessible for DDVCS. The $x = \pm\xi$ correspond to DVCS and TCS limits. On the right, the GPD $H^u(x, \xi, t)$ as a function of x and ξ at $t = 0$ according to the VGG model.

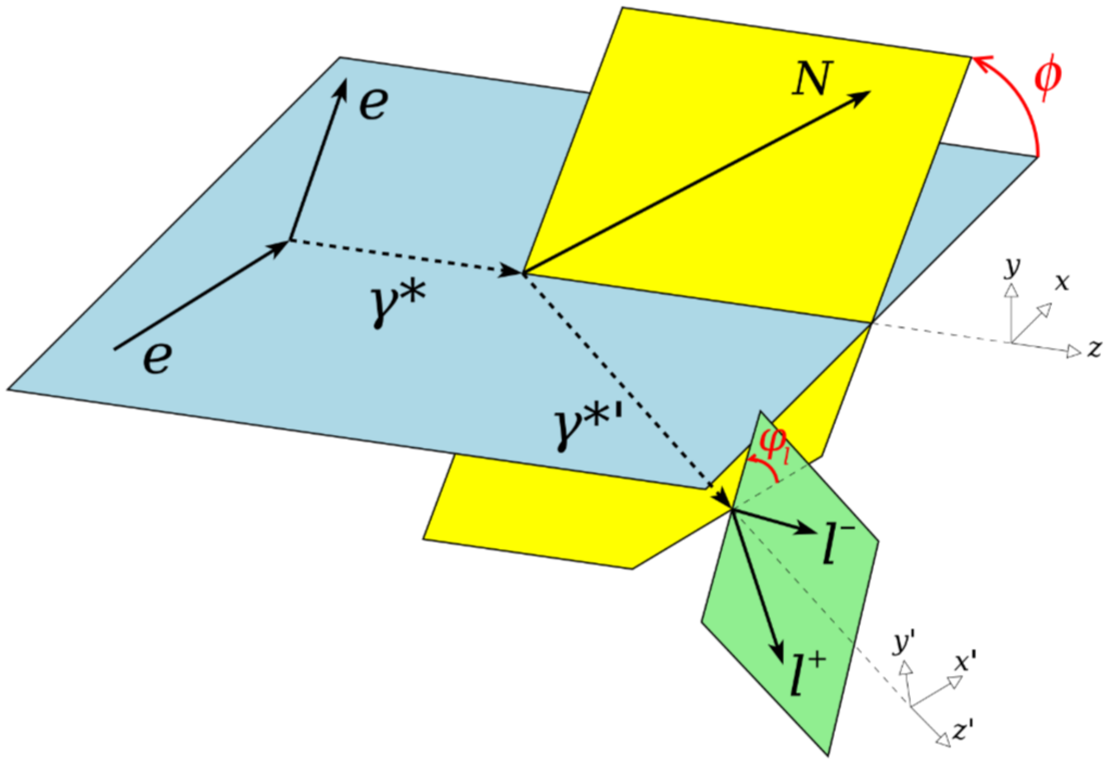

FIG. 11: Scattering planes and definition of angles in lepton pair electroproduction.

As in the case of DVCS and TCS, Bethe-Heitler interferes at the amplitude level. The diagrams of the two interfering BH processes are shown in Fig.9.(b). With these three interfering processes, the 7-fold differential cross section of electroproduction of lepton pairs can be expressed as [24–26]:

$$\frac{d\sigma^7}{dQ^2 dt dx_B d\phi dQ'^2 d\Omega_l} = \frac{\alpha}{16(2\pi)^3}\frac{x_B y}{Q^2}(|\mathcal{T}_{BH1}+\mathcal{T}_{BH2}|^2+\mathcal{T}^2_{VCS}+\mathcal{T}_{VCS}\cdot\mathcal{T}_{BH1}+\mathcal{T}_{VCS}\cdot\mathcal{T}_{BH2}), \quad (17)$$

where we use notations of [25] and $\mathcal{T}_{VCS}\cdot\mathcal{T}_{BH1(2)} = \mathcal{T}_{VCS}\cdot\mathcal{T}^*_{BH1(2)}+\mathcal{T}^*_{VCS}\cdot\mathcal{T}_{BH1(2)}$. The solid angle of the lepton pair is defined as $d\Omega_l = \sin\vartheta_l d\vartheta_l d\varphi_l$, α is the fine structure constant, and $y = p\cdot q/p\cdot k$. The definition of the angles ϕ, φ_l and ϑ_l is shown in Fig.11.

The most direct information on GPDs is encoded in the observables that arise from the interference of VCS and BH amplitudes. In DDVCS, isolating $\mathcal{T}_{VCS}\mathcal{T}^*_{BH}$ interference term is more intricate than in DVCS or TCS. There are two BH processes and three interference terms (including $\mathcal{T}_{BH1}\cdot\mathcal{T}_{BH2}$). The VCS amplitude is odd under the beam lepton charge interchange and even under the exchange of decay leptons momenta (l^+/l^- angle exchange). The first BH amplitude, BH1 in Fig.9, is even, while the second, BH2, is odd with respect to the interchange of both the beam lepton charge and the decay leptons momenta. These symmetries allow access to DVCS-like single-spin asymmetries, such as longitudinal beam spin asymmetry, in 5-five fold cross-section measurement where the integration over the solid angle of decay leptons, Ω_l, eliminates the contribution of the interference of BH2 with the other two amplitudes and only the interference term $\mathcal{T}_{VCS}\mathcal{T}^*_{BH1}$ ($d^5\sigma_{Int_1}$) remains:

$$\begin{aligned}\frac{d\sigma^5}{dQ^2dtdx_Bd\phi dQ'^2d\Omega_l} &= \int_0^{2\pi} d\varphi_l \int_0^{\pi} d\vartheta_l \sin\vartheta_l \frac{d\sigma^7}{dQ^2dtdx_Bd\phi dQ'^2d\Omega_l} \\ &= d^5\sigma_{BH1} + d^5\sigma_{BH2} + d^5\sigma_{VCS} + d^5\sigma_{Int_1} + \lambda(d^5\tilde{\sigma}_{VCS} + d^5\tilde{\sigma}_{Int_1}).\end{aligned} \tag{18}$$

Here $\tilde{\sigma_X}$ are beam polarization-dependent cross sections, and λ is the beam polarization. The polarized cross-section difference then will read:

$$\Delta\sigma_{LU} = d\overrightarrow{\sigma}^5 - d\overleftarrow{\sigma}^5 = \lambda[d^5\tilde{\sigma}_{VCS} + d^5\tilde{\sigma}_{Int_1}]. \tag{19}$$

The $d^5\tilde{\sigma_{VCS}} \propto \mathrm{Im}\mathcal{T}_{VCS}\mathcal{T}^*_{VCS}$ is expected to be negligible as it arises from twist-three Compton form factors [60] and the beam spin asymmetry proportional to $\mathcal{T}^*_{BH_1}\mathrm{Im}\mathcal{T}_{VCS}$ and depends on linear combination of Compton form factors:

$$\Delta\sigma_{LU} \propto \mathrm{Im}[F_1\mathcal{H}(\xi',\xi,t) + \xi'(F_1+F_2)\tilde{\mathcal{H}}(\xi',\xi,t) - \frac{t}{4M^2}F_2\mathcal{E}(\xi',\xi,t)]\sin\phi. \tag{20}$$

Here, the imaginary part of the CFFs relate to the GPDs at the ξ' and ξ point, as in Eq.15, and varying the virtualities of the spacelike and timelike photons can independently vary both scaling variables and map out the GPDs in the $x = \xi'$ and ξ space, offering a new sensitivity to GPDs beyond the $x = \pm\xi$ constraint of DVCS and TCS.

2. *Observables of interest*

Double Deeply Virtual Compton Scattering (DDVCS) has garnered significant attention in theoretical and phenomenological studies due to its potential to provide detailed insights into GPDs. Early theoretical frameworks laid the foundation for understanding DDVCS in terms of GPDs [24–26] and provided predictions for cross-sections and beam helicity asymmetries, emphasizing the feasibility of experimental measurements. More studies of DDVCS, incorporating advancements in GPD modeling and experimental capabilities, JLAB e^+ and 22 GeV, and the EIC, have followed, highlighting key measurements [61–63]. These studies stressed the importance of measuring the beam spin asymmetries in both space-like $Q^2 > Q'^2$ and time-like $Q^2 < Q'^2$ regions and observe sign change of A_{LU}:

$$A_{LU} = \frac{d\overrightarrow{\sigma}^5 - d\overleftarrow{\sigma}^5}{d\overrightarrow{\sigma}^5 + d\overleftarrow{\sigma}^5}. \tag{21}$$

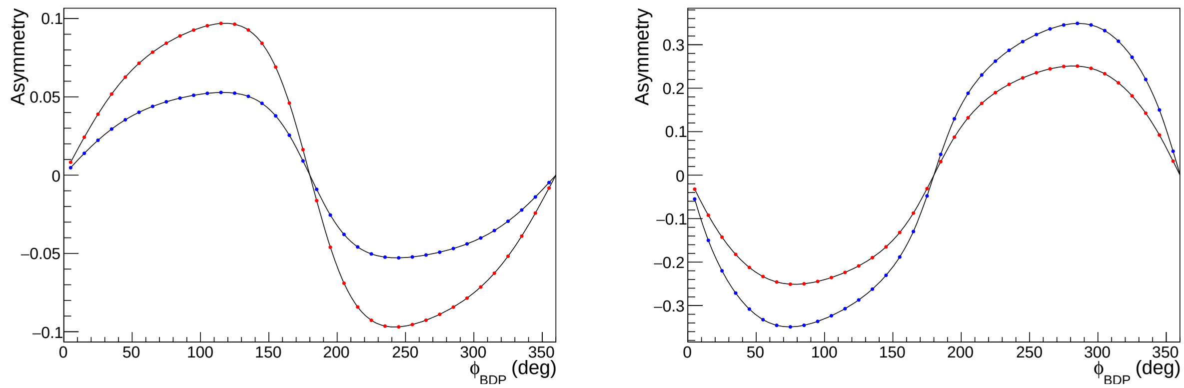

FIG. 12: Beam spin asymmetry predictions in DDVCS using the *PARTONS* framework with Goloskokov-Kroll model. On the left, asymmetries are shown in the space-like region where the red (blue) curve corresponds to kinematics $Q^2 = 3.5$ GeV^2 and $Q'^2 = 1.5$ GeV^2 ($Q'^2 = 2.5$ GeV^2), $x_B = 0.2$ and $-t = 0.5$ GEV^2. On the right are the predicted asymmetries for the time-like region where the red (blue) curve corresponds to $Q'^2 = 3.7$ GeV^2 and $Q^2 = 1.2$ GeV^2 ($Q'^2 = 2.8$ GeV^2 and $Q^2 = 0.5$ GeV^2).

The sign change, shown in Fig.12, is a consequence of the factorization and a strong test for the perturbative QCD regime. Studies in [61] show how one can combine measurements of beam charge and spin asymmetries with polarized e^- and e^+ beams to separate the interference ($d^5\tilde{\sigma}_{Int_1}$) and the DDVCS ($d^5\tilde{\sigma}_{VCS}$) terms in Eq.19. Moreover, combining beam charge and decay lepton angular asymmetries offers clean access to the real part of the DDVCS and BH interference part, $\mathrm{Re}\mathcal{T}_{VCS}\mathcal{T}^*_{BH1}$. In [62], numerical estimates of DDVCS observables at the kinematics of JLAB and of the EIC using the *PARTONS* framework [21] are presented comparing different GPD models, and the measurability of the DDVCS reaction in these experimental facilities is demonstrated. Finally, the most relevant study of the sensitivity of JLAB DDVCS measurements to GPDs has recently been published in [63], where expected results of the proposed upgraded CLAS12 and the future SoLID spectrometer are shown. The main challenge of studying DDVCS experimentally is its cross-section, a few orders of magnitude smaller than the one of DVCS. In Fig. 13, the differential cross-sections for DVCS+BH (left) and DDVCS+BH (right) are presented for $E = 10.6$ GeV electron scattering off a proton. The kinematics of the scattered electron is fixed at $Q^2 = 2.75$ GeV^2 and $x_B = 0.15$. For DDVCS, the virtuality of the outgoing photon is $Q'^2 = 1.4$ GeV^2. As it can be seen, in the whole t range of interest, cross sections for DVCS and DVCS+BH are about four orders of magnitude larger than that of DDVCS and DDVCS+BH. Moreover, the outgoing

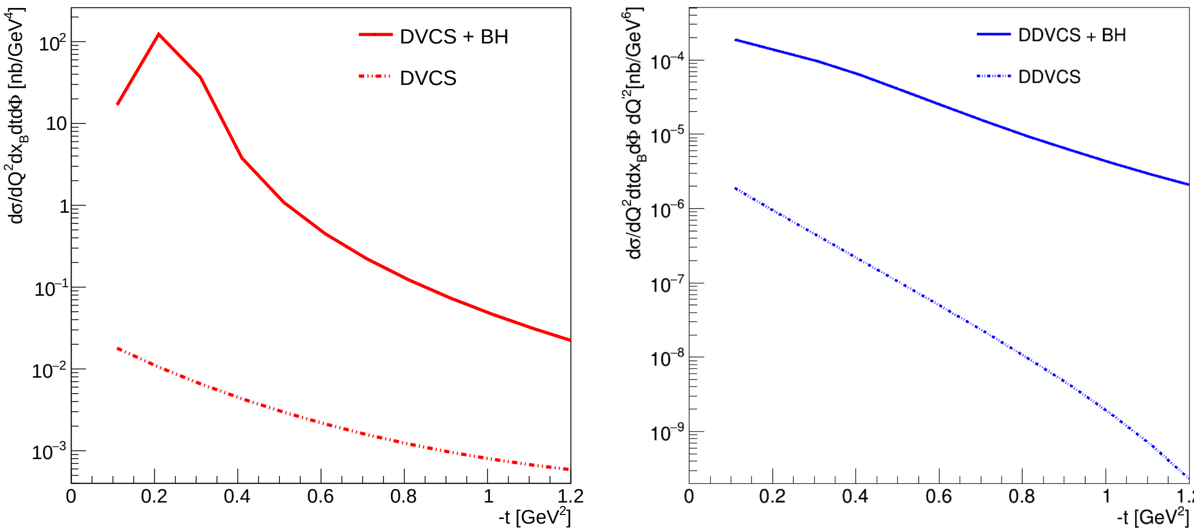

FIG. 13: Differential cross sections of DVCS (left) and DDVCS (right) processes with $E = 10.6$ GeV electron beam. The scattered electron kinematics is fixed at $Q^2 = 2.75$ GeV^2 and $x_B = 0.15$. The virtuality of the time-like photon in DDVCS is $Q'^2 = 1.4$ GeV^2.

time-like photon must be identified in a di-lepton decay of a different flavor than the beam to eliminate ambiguity and anti-symmetrization issues. Otherwise, additional cross terms will arise due to the identity of the beam and decay lepton.

To overcome these challenges, a large-acceptance detector capable of running at very high luminosities, $\geq 10^{37}$ cm^{-2} sec^{-1}, with good muon detection is required to study for DDVCS in the reaction $ep \to e'p'\mu^+\mu^-$. Jefferson Lab at the luminosity frontier is the only place in the world where DDVCS in the valence region can be measured.

E. Near threshold J/ψ production

1. *Overview*

In addition to the critical measurement of DDVCS, the experimental setup described previously will be capable of measuring the muon pair produced by the decay of J/ψ mesons. Given that the branching ratio of $J/\psi \to \mu\mu$ is only 6%, the large luminosity of this experiment combined with a good muon detection efficiency will allow to collect a large amount of J/ψ. This will allow to explore the gluon content of the proton in great details.

The photoproduction of the J/ψ meson off a nucleon (in the case of this experiment, a proton) has long been identified as an important process to probe the gluon distribution inside the nucleon [64]. Figure 14 shows the diagram of the reaction assuming the produced J/ψ interacts with the nucleon only by the exchange of gluons. Recent theoretical developments [65–69] have suggested that the gluon Gravitational Form Factors (GFFs) of the proton [70, 71] can be accessed via the measurement of the t-dependence of the cross section. Lattice QCD calculations have also recently provided good estimates for the gluon GFFs [72–74]. Comprehensive reviews of the theoretical and experimental results on GFFs can be found in [35, 75, 76].

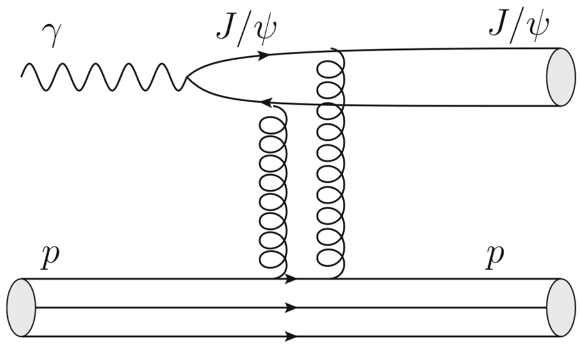

FIG. 14: Diagram representing the photoproduction of the meson J/ψ on the proton, assuming the interaction only involves the exchange of gluons.

2. *Existing experimental results*

While photoproduction of J/ψ on a proton target has already been measured both at HERA [77, 78] and at LHC experiments in ultra-peripheral collisions, this measurement near its energy threshold is only possible when the initial photon has an energy about 8.2 GeV in the lab frame. Measurement of this reaction in this kinematic regime with large statistics has been made possible by the 12-GeV upgrade of the CEBAF accelerator at JLab [79]. Two recent measurements at Jefferson Lab have been published: first by the GlueX collaboration [80], and by the E12-16-007 experiment in Hall C [81]. A third measurement, performed using data taken by CLAS12 with a proton target in 2018 and 2019, is currently under internal collaboration review.

In the case of the GlueX measurement reported in [80], a tagged-photon beam is incident on a hydrogen target and the J/ψ is reconstructed in its electron-positron final state. Both the total cross section as a function of the incoming real photon energy and the differential cross section as a function of t have been extracted. The total cross-section measured by GlueX is reported in Fig. 15.

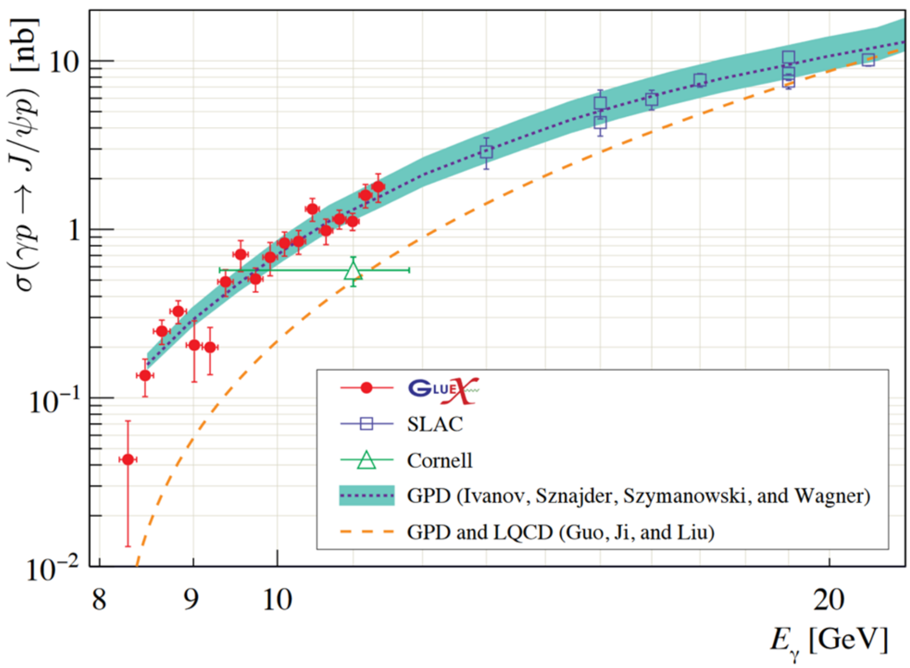

FIG. 15: Near threshold J/ψ photoproduction cross-section as a function of the incoming photon energy. The red data points are the measurement by the GlueX collaboration. Figure from [80]

The Hall C experiment (E12-16-007 or J/ψ-007) used an untagged photon beam scattering of a proton target. The electron-positron pair from the decay of J/ψ is then detected in the HMS and SHMS spectrometers, respectively. This experiment measured the differential cross-section as a function of the squared momentum transferred to the proton, $-t$, as shown in Fig.16 [81].

In Hall B, CLAS12 has gathered data on a proton target in 2018 and 2019. The results of the E12-12-001A experiment, aiming at measuring the photoproduction of J/ψ from these data are currently under internal collaboration review. Both the total cross-section and the t-differential cross section have been measured. Figure 17 shows the preliminary total cross-section using CLAS12 data.

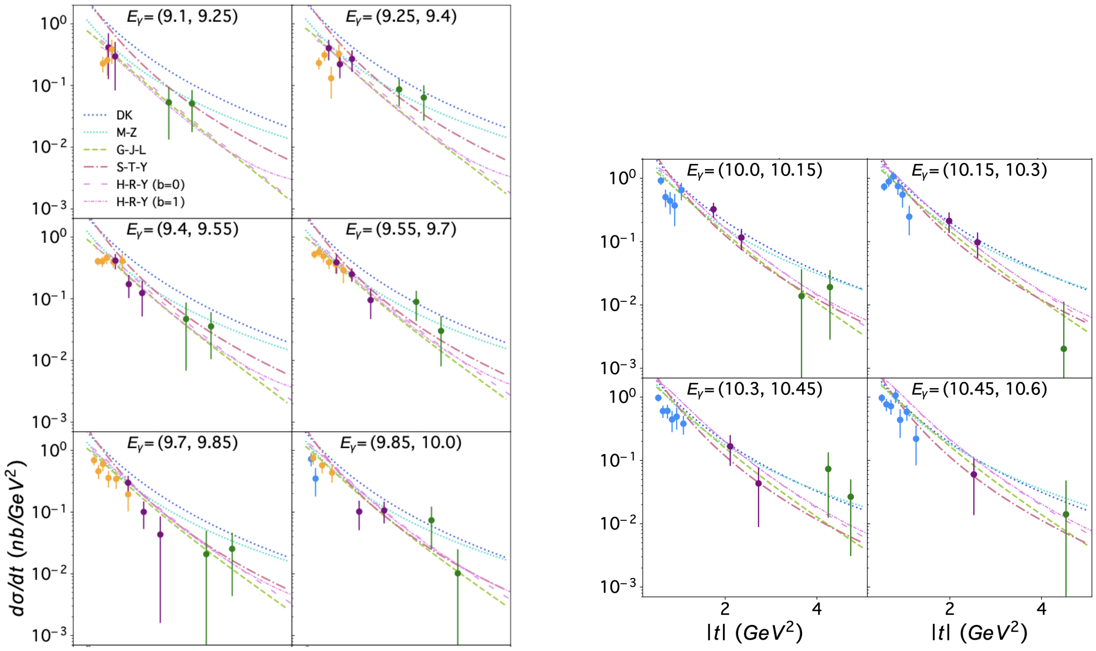

FIG. 16: Differential cross-section of the near-threshold photoproduction of J/ψ as a function of the Mandelstam variable $-t$, obtained by the E12-16-007 experiment in Hall C [81].

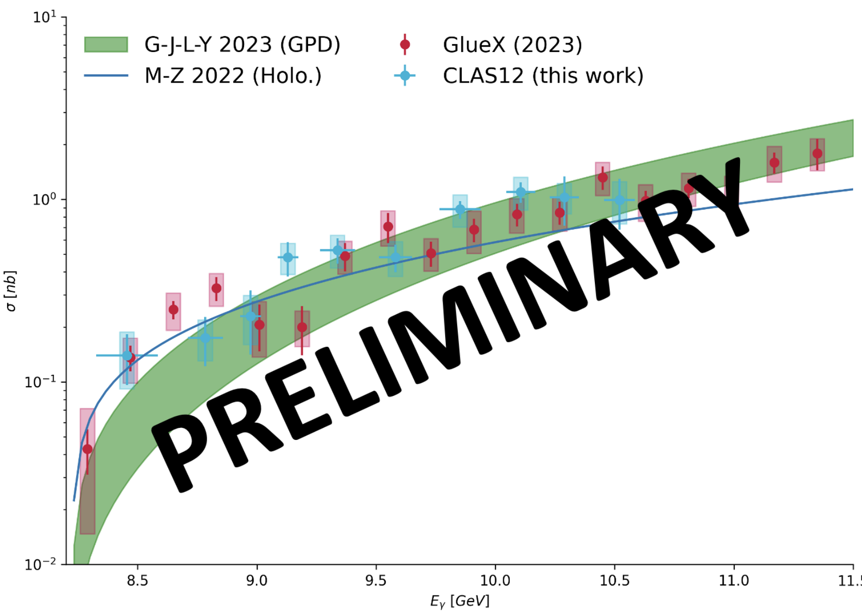

FIG. 17: Near threshold J/ψ photoproduction cross-section as a function of the incoming photon energy. The blue points are the preliminary results of CLAS12. The red data points are the measurement by the GlueX collaboration. The blue line and green bands are model predictions from holographic [68] and GPD [69] models respectively.

3. Theoretical models and interpretation in terms of gluons distribution in the proton

The Gravitational Form Factors (GFFs) of the proton have been an active topic of research recently. They appear in the matrix element of the QCD energy-momentum tensor which reads:

$$
\begin{aligned}
&\langle p_f, s_f | T^{\mu,\nu}_{q,g}(0) | p_i, s_i \rangle = \qquad (22)\\
&\bar{u}(p_f, s_f)\Big(A_{q,g}(t)\gamma^{\{\mu}P^{\nu\}} + B_{q,g}\frac{iP^{\{\mu}\sigma^{\nu\}\rho}\Delta_\rho}{2M_N} + C_{g,q}\frac{\Delta^\mu\Delta^\nu - g^{\mu\nu}\Delta^2}{M_N} + \bar{C}_{q,g}(t)M_N g^{\mu,\nu}\Big)u(p_i, s_i),
\end{aligned}
$$

where the GFFs are the functions $A_{q,g}(t)$, $B_{q,g}(t)$, $C_{g,q}$, and $\bar{C}_{q,g}(t)$ for gluons and quarks respectively. The gluon GFFs can be related to the gluon GPDs, via their integration of the momentum fraction x as:

$$\int_0^1 dx H_g(x, \xi, t) = A^g_{2,0}(t) + (2\xi)^2 C^g_2, \qquad (23)$$

$$\int_0^1 dx E_g(x, \xi, t) = B^g_{2,0}(t) - (2\xi)^2 C^g_2. \qquad (24)$$

Assuming Vector-Meson-Dominance, i.e. the exchange of a pair of gluons between the proton and the J/ψ, as depicted in Fig.14, various models have been develop to relate the differential cross-section of the near threshold J/ψ photoproduction to the gluon GFFs of the proton. Note that in all models so far, the $B_{q,g}(t)$ form factors are assumed to be small according to the LQCD findings [73, 74] and thus ignored. Because it is mostly unknown from lattice calculation, the $\bar{C}_g(t)$ form factors is ignored, while its true effect might be large [82, 83] as $\bar{C}(0)$ is related to the trace anomaly of the QCD EMT.

Models based on holographic QCD has been developed in [68, 84–86], and models based on GPDs has been detailled in [66, 69].

In both cases, the functional form of the GFFs is not given. Previous works have used a tripole dependence for both the A and C form factors:

$$A_g(t) = \frac{A(0)}{\left(1 - \frac{t}{m_A^2}\right)^3}, \quad C_g(t) = \frac{C(0)}{\left(1 - \frac{t}{m_C^2}\right)^3}. \qquad (25)$$

From the differential cross-section data obtained by the Hall C measurement, an extraction of the proton gluonic GFFs was performed using both the GPD-based model and the holographic QCD model. Figure 18 shows the extracted GFFs obtained from the J/ψ-007 results.

From the $D_g(t) = 4C_g(t)$ form factors, it is possible to extract the pressure distribution pro-

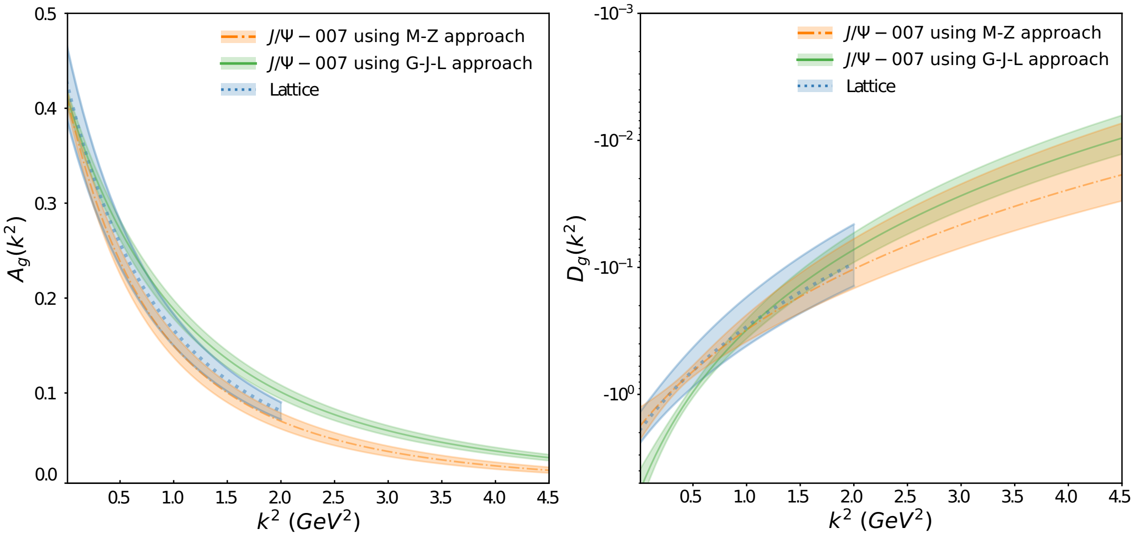

FIG. 18: Extraction of gluonic Gravitational Form Factors $A_g(t)$ and $D_g(t)$, performed using the differential cross-section extracted by the E12-16-007 experiment in Hall C. Fig. in [81], corrected in [87]

duced by the gluons in the proton. From the Fourier transform of $D_g(t)$ and assuming a tripole dependence, one gets:

$$\tilde{D}(r) = \int \frac{d^3\Delta}{(2\pi)^3} e^{-i\Delta\cdot r} D(\Delta, m_C) = \int \frac{d^3\Delta}{(2\pi)^3} e^{-i\Delta\cdot r} \frac{D(0)}{(1+\frac{\Delta^2}{m_C^2})^3} = D(0)\frac{m_C^3}{32\pi}(1+m_C r)e^{-m_C r}, \quad (26)$$

which can then be used to derive a transverse and shear pressure profile as:

$$r^2 p(r) = \frac{1}{6m_N}\frac{d}{dr}\left(r^2\frac{d}{dr}\tilde{D}(r)\right) = \frac{1}{6m_p}\frac{4C(0)\times m_C^5}{32\pi} \times r^2 \times (m_C \times r - 3)e^{-m_C\times r}, \quad (27)$$

and

$$r^2 s(r) = -\frac{1}{4m_N} r^3 \frac{d}{dr}\left(\frac{1}{r}\frac{d}{dr}\tilde{D}(r)\right) = \frac{-1}{4m_p}\frac{4C(0)\times m_C^6}{32\pi} \times r^3 e^{-m_C\times r}, \quad (28)$$

where the tripole dependence of the GFFs is assumed and Eq.26 is used to compute the derivative.

Finally, one can also define the mass and scalar radius of the proton:

$$\langle r_m^2\rangle_g = 6\frac{1}{A_g(0)}\frac{dA_g(t)}{dt}\bigg|_{t=0} - 6\frac{1}{A_g(0)}\frac{C_g(0)}{M_N^2} = \frac{18}{m_A^2} - 6\frac{1}{A_g(0)}\frac{C_g(0)}{M_N^2}, \quad (29)$$

$$\langle r_s^2\rangle_g = 6\frac{1}{A_g(0)}\frac{dA_g(t)}{dt}\bigg|_{t=0} - 18\frac{1}{A_g(0)}\frac{C_g(0)}{M_N^2} = \frac{18}{m_A^2} - 18\frac{1}{A_g(0)}\frac{C_g(0)}{M_N^2}. \quad (30)$$

4. *Open-charm and pentaquark contributions*

The interpretation of the J/ψ differential cross-section in terms of gluon GFFs is valid if the process can indeed be described by the exchange of two gluons. However, one should also include an open-charm loop and potential pentaquark contributions (see Fig.19) to properly describe the process near threshold. A lot of work has been done to estimate the impact of both of these contributions and their potential signal in the data (see for example [88, 89] for open-charm results, and [90–94] for discussions on potential pentaquark contributions).

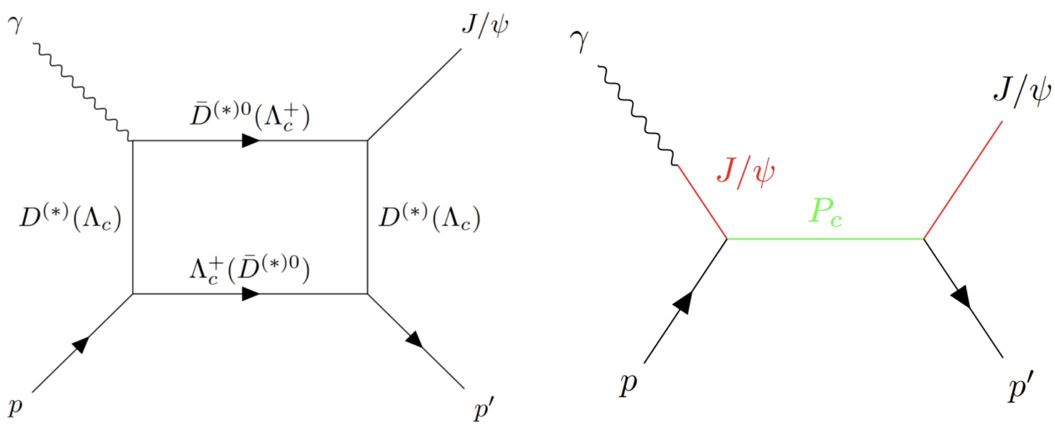

FIG. 19: Additional diagrams which have to be considered when describing the photoproduction of J/ψ near threshold.

The result suggests that VMD might not be applicable and calls for more data, especially as a function of the incoming photon energy in the range of the $\Lambda_C \bar{D}^{(*)}$ thresholds at 8.7 and 9.4 GeV.

III. DETECTOR CONFIGURATION

The μCLAS12 setup will utilize a modified CLAS12 detector, optimized for operation at luminosities $\geq 10^{37}$ cm^{-2} sec^{-1}, with enhanced muon detection capabilities. The CLAS12 detector, shown in Fig. 20, has been in operation since 2018, successfully collecting data with cryogenic, solid, and polarized targets using electron beams up to 10.6 GeV, operating close to its design luminosity of 10^{35} cm^{-2} sec^{-1}. The success of running such an open acceptance detector at high luminosities lies in effectively shielding sensitive detector elements from electromagnetic background (EM-background). Möller scattered electrons create a significant part of the EM-background. The CLAS12 forward detector (FD) is shielded from this background with the help of the 5 T field of the CLAS12 solenoid magnet and a so-called Möller cone, made of tungsten, that covers forward angles up to 2.5°. A well-shielded FD is the core element of the proposed detector for the DDVCS experiment.

The performance of CLAS12 in terms of efficiencies and resolutions is well understood and supported by a validated GEANT4-based Monte Carlo (MC) model, GEMC [95]. Since its inception, significant efforts have been made to enhance reconstruction and particle identification (PID) algorithms, particularly by implementing Machine Learning based methods. One significant advancement is ML-aided forward tracking, which has now achieved over 90% efficiency, even at luminosities exceeding design specifications. Future tracking detector upgrades are expected to enable CLAS12 to operate efficiently at twice the design luminosity.

ML methods have also been successfully applied to PID, significantly improving particle identification in the kinematic regions outside the reach of traditional methods. As demonstrated in [19, 96], ML-enhanced electron identification (e-ID) has enabled a clean separation of electrons and positrons from pions with momenta above the pion threshold in the High Threshold Cherenkov Counter (HTCC), $p_{thr} > 4.7$ GeV/c. For the μCLAS12 program, the ML tool using the Boosted Decision Tree (BDT) method for muon identification, developed for CLAS12 J/ψ studies, is particularly valuable. The existing algorithm leverages forward calorimeter (fECal) information to enhance muon sample purity. In Fig.21, the implementation of the ML μ-ID in J/ψ photoproduction is demonstrated. In the left plot of the figure, the invariant mass distribution of two minimum ionizing particles (MIP), dominated by pion pairs, is shown, assuming these are muons. No peak is visible at the J/ψ mass peak. With a cut on the BDT classifier, a clear peak at J/ψ mass, ~ 3.09 GeV, is visible, right plot. The classifier cut eliminates more than 90% of events, reducing single pion contamination in the muon sample by a factor of > 5.

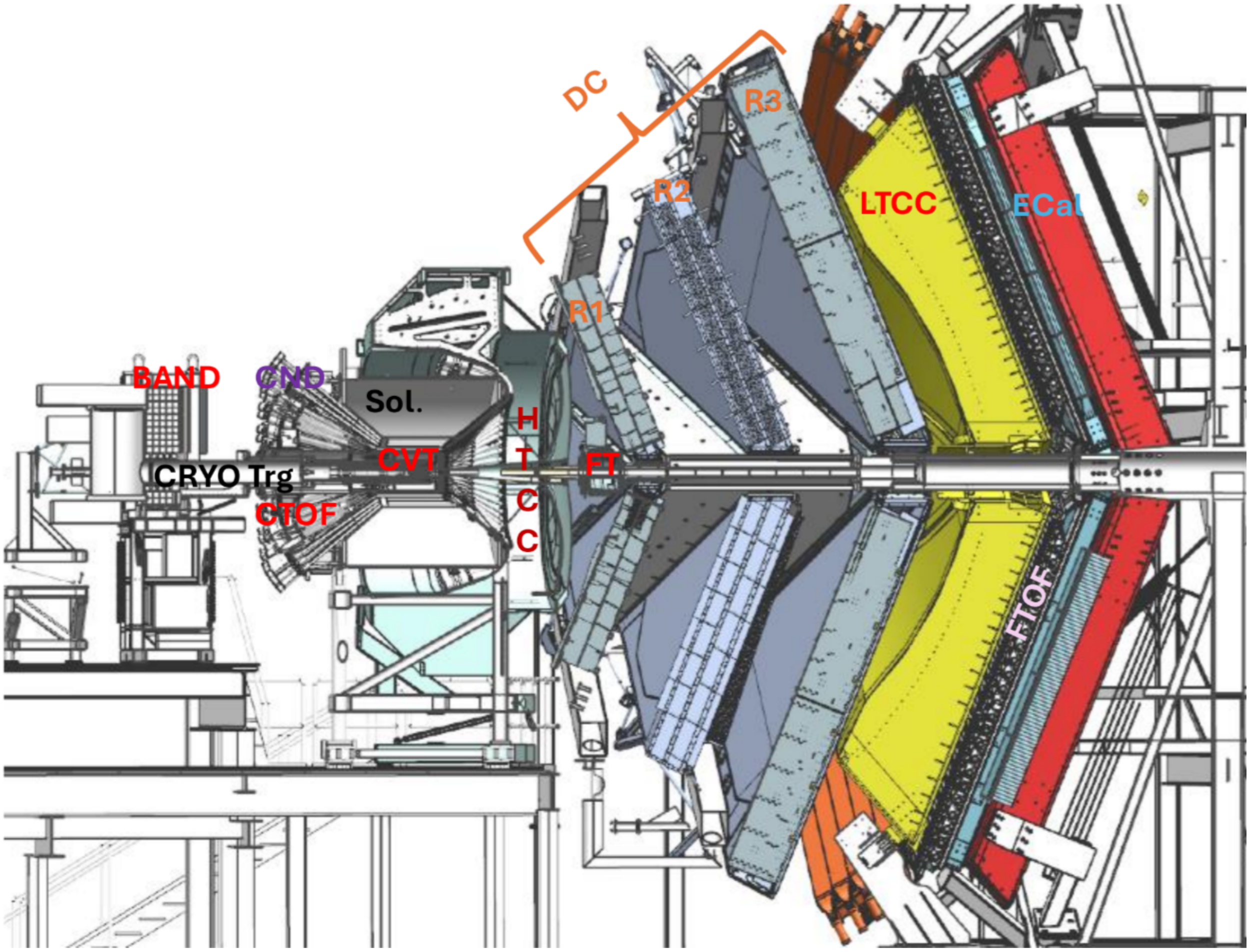

FIG. 20: The CLAS12 detector in Hall-B, mid-plane cut view. The detectors that will be removed/replaced are noted in red.

A. The μCLAS12 detector

With the physics final states in mind, $e'\mu^+\mu^-(p')$ and $\mu^+\mu^-p'(e')$, the modifications to CLAS12 for DDVCS measurement have the following goals:

- Shield the forward detector (FD) from the electromagnetic background to enable high-luminosity operation,
- Enhance muon identification in the forward detector, reaching more than $\times 100$ suppression of charged pions,
- Provide electron reconstruction and vertex determination,
- Detect the recoil proton in a high background environment.

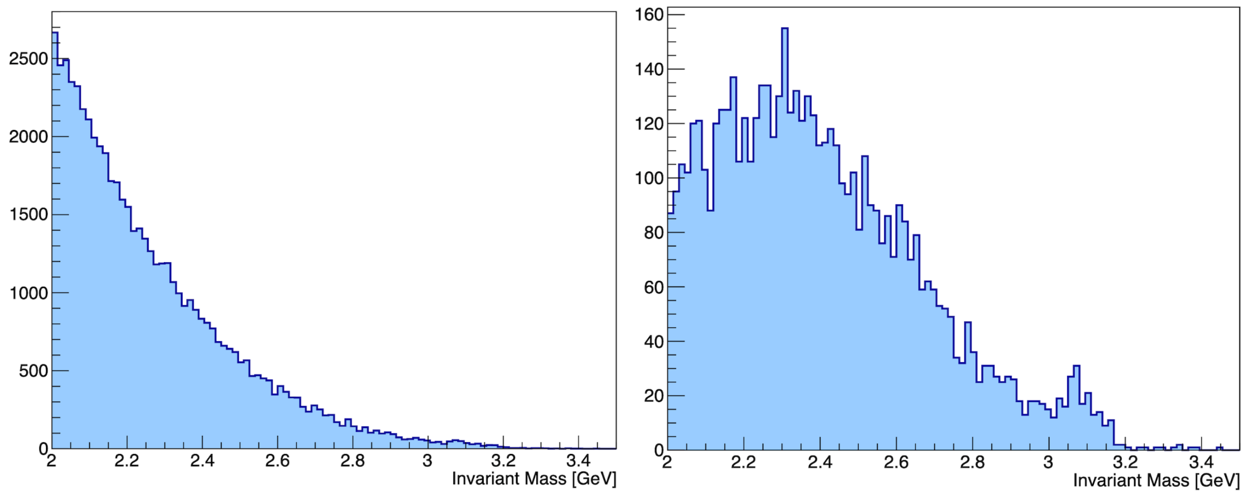

FIG. 21: On the left, the invariant mass distribution of two minimum ionizing particles (MIP), dominated by pion pairs. The right plot is the invariant mass of pairs after the BDT cluster cut.

These goals will be achieved by replacing the CLAS12 High Threshold Cherenkov Counter (HTCC) with a $PbWO_4$ calorimeter surrounded by a tungsten shield (wECal). Before the calorimeter/shield, a high-rate vertex tracker (FVT) will replace the existing forward MicroMegas detectors. A new MPGD detector for recoil proton tracking in the solenoid field will replace the central detector tracking system (CVT) and the central time-of-flight counters (CTOF). Other changes for converting CLAS12 to μ-CLAS12 include removing the forward tagger system (FT) and extending the Möller cone coverage to up to 7° in polar angle. The new $PbWO_4$ calorimeter and a 30 cm thick W-shield will cover the 7° to 35° polar angular range with 2π azimuthal coverage. Other detectors that will not be part of μCLAS12 are the backward neutron detector (BAND) and the low threshold Cherenkov counter (LTCC).

The conceptual design of the μCLAS12 setup is modeled in CAD as shown in Fig.28. While some engineering details are still being worked out, the CLAS12 GEANT4 model has been modified to create a model of μCLAS12 based on the CAD model. Together with the CLAS12 event reconstruction algorithm, COATJAVA [97], this tool-set is used to study backgrounds, occupancies, and rates in μCLAS12 and event reconstruction. As will be shown below, the detector will be operable at luminosities of $\geq 10^{37}$ cm^{-2} s^{-1} and support the proposed studies, producing high-quality results with wide kinematical coverage.

The following presents details of new detectors, beamline, and the target.

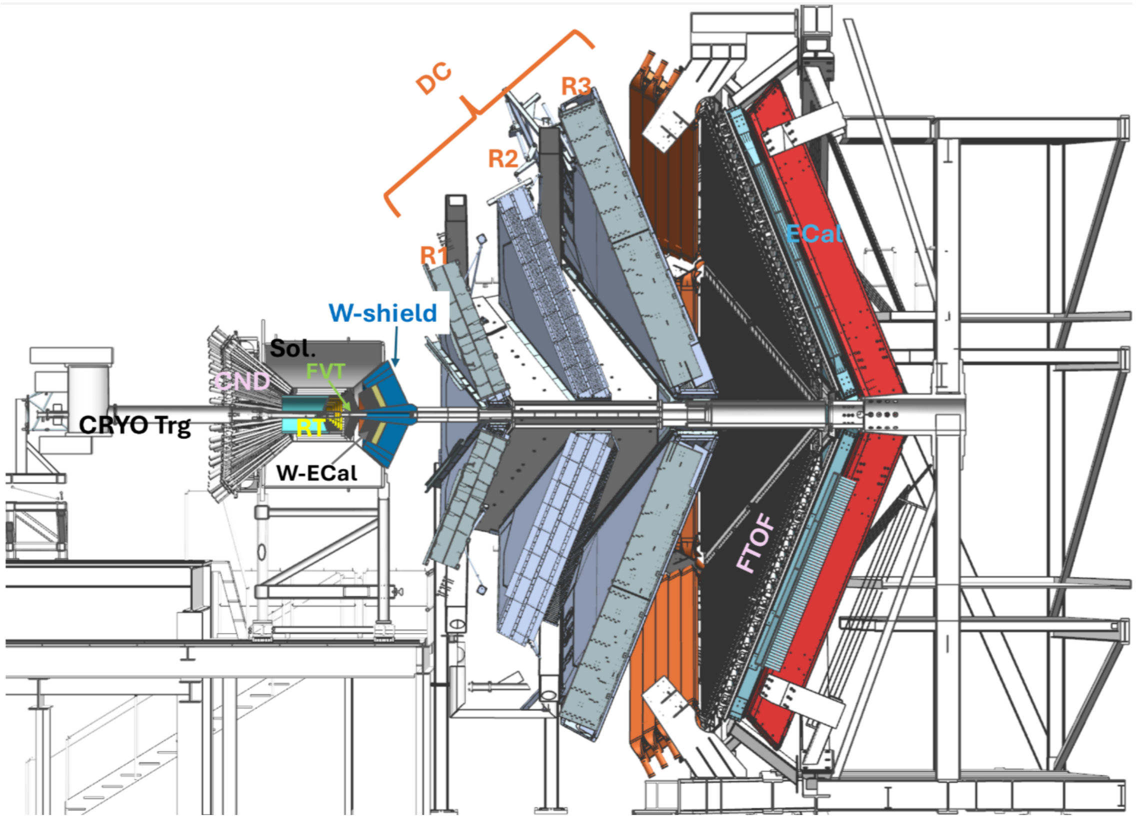

FIG. 22: The concept of the proposed DDVCS setup. The W-shield and $PbWO_4$ calorimeter are installed in the place of HTCC. The FVT and the recoil tracker are inside the solenoid.

1. $PbWO_4$ calorimeter and W-shield

The calorimeter for the detection of electrons will be mounted at 60 cm from the target center and will consist of about 1320, 20 cm long $PbWO_4$ modules. The CAD rendering and engineering layout of the wECal (lead-tungsten calorimeter and the tungsten shield) is shown in Fig.23. We intend to use tapered crystals arranged to form a ring around the beamline with a hole in the center, similar to the Inner Calorimeter (IC) of the Hall-B DVCS experiment [98]. The central hole will extend to 7°, and the outer perimeter of the ring will be at 30° of the polar angle. In the inner part of the calorimeter, from 7° to 12° degree polar angular range, the cross-section of the front face of crystals will be 1.3×1.3 cm^2, above 12° crystals of 1.5×1.5 cm^2 will be used. Smaller modules at forward angles are needed to keep rates per module at an acceptable level. The readout of modules will be performed with APDs from the downstream face of the crystal.

Such calorimeters have been successfully used at JLAB since the early 2000s. The first implementation of a compact lead-tungsten calorimeter was in Hall-B for the 6 GeV DVCS experiment. The so-called inner calorimeter (IC) had 424 channels made of tapered crystals from CMS with

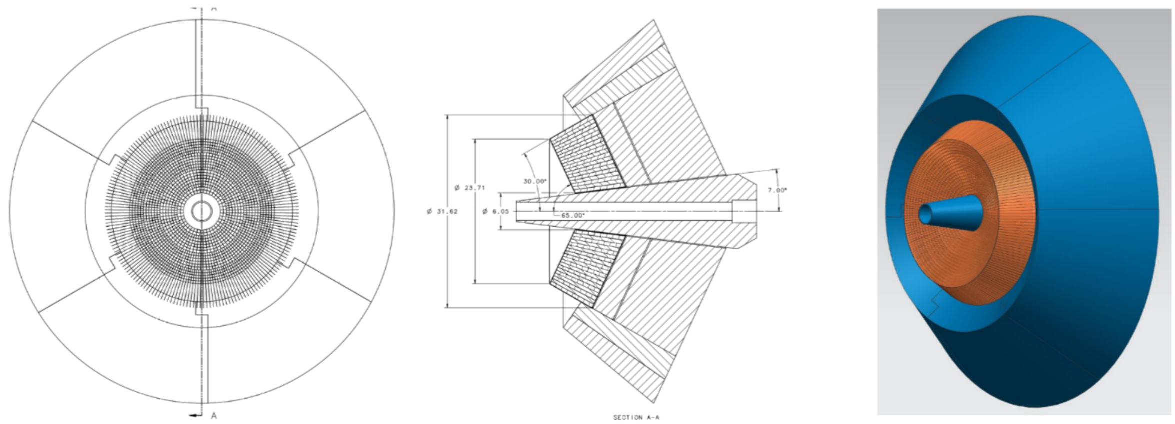

FIG. 23: The W-shield and $PbWO_4$ calorimeter.

APD readout. Later, these modules were re-purposed for the Heavy Photon Search experiment (HPS), 442 channels [99]. Both calorimeters operated at close to 1 MHz rate per channel and had $\sigma/E \simeq 4.5\%/\sqrt{E}$ resolution. Another implementation in Hall B was for the PrimEx calorimeter, where $PbWO_4$ modules are used to replace lead-glass modules at small angles to improve the energy resolution. The modules, in this case, were read out with PMTs. The upgraded calorimeter, HyCal, was successfully used in the PRad experiment and achieved energy resolution of $\sigma/E \leq 2.5\%/\sqrt{E}$. In the 12 GeV era, a few more $PbWO_4$ calorimeters have been built and operated in high-rate environments. The forward tagger calorimeter (FTECal) [100] in Hall-B uses 332, $1.5 \times 1.5 \times 20$ cm^3 crystals read out 1×1 cm^2 LAAPDs. The FTCal runs at 0°C and achieves resolution $\sim 3.5\%/\sqrt{E}$. More recently, two large area $PbWO_4$ calorimeters have been built, commissioned, and used in experiments in Hall C, ~ 1000 channels NPS[101], and a 1600 module upgrade of the Hall-D GluEx forward calorimeter central part. These two detectors use PMTs for light readout. Beam tests of a small prototype of GluEx calorimeter, 140, $2. \times 2. \times 20$ cm^3 modules, demonstrated the expected energy resolution of $\sigma/E \leq 3\%/\sqrt{E}$ [102].

Collaborations at JLAB and Hall-B, in particular, have extensive experience fabricating and running $PbWO_4$ calorimeters.

2. *Forward vertex GEM tracker*

The proposed experiment requires detecting three forward going charged particles: an electron (e^-) in the calorimeter and a muon pair (μ^+, μ^-) in the CLAS12 Forward Detector. All three particles originate from the target and traverse the strong magnetic field of the CLAS12 solenoid before reaching the detectors. Additionally, the muons pass through the calorimeter and shield, undergoing significant energy loss and multiple scattering before their momentum is analyzed. A Forward Vertex Tracking (FVT) detector near the target is essential to ensure precise vertex reconstruction.

We propose using a Micro-Pattern Gaseous Detector (MPGD) tracker downstream of the target, positioned in front of the calorimeter, to reconstruct track vertex parameters. Specifically, we have selected a triple GEM [103] design, which is well-suited for high-rate environments. The GEM technology relies on gas avalanche multiplication within micro-scale holes (50 μm), with multiple cascaded GEM foils providing high gain and operational stability, as illustrated in Fig. 24 (left). GEM-based tracking detectors have been widely used in Jefferson Lab (JLab) experiments since the early 2000s, including Hall B's Bonus [104], eg6 [105], and the Proton Charge Radius [106] experiments. Furthermore, GEM trackers designed for rates of $\sim$ 1 MHz/cm^2 have been successfully fabricated and operated in the Hall A SBS [107] spectrometer.

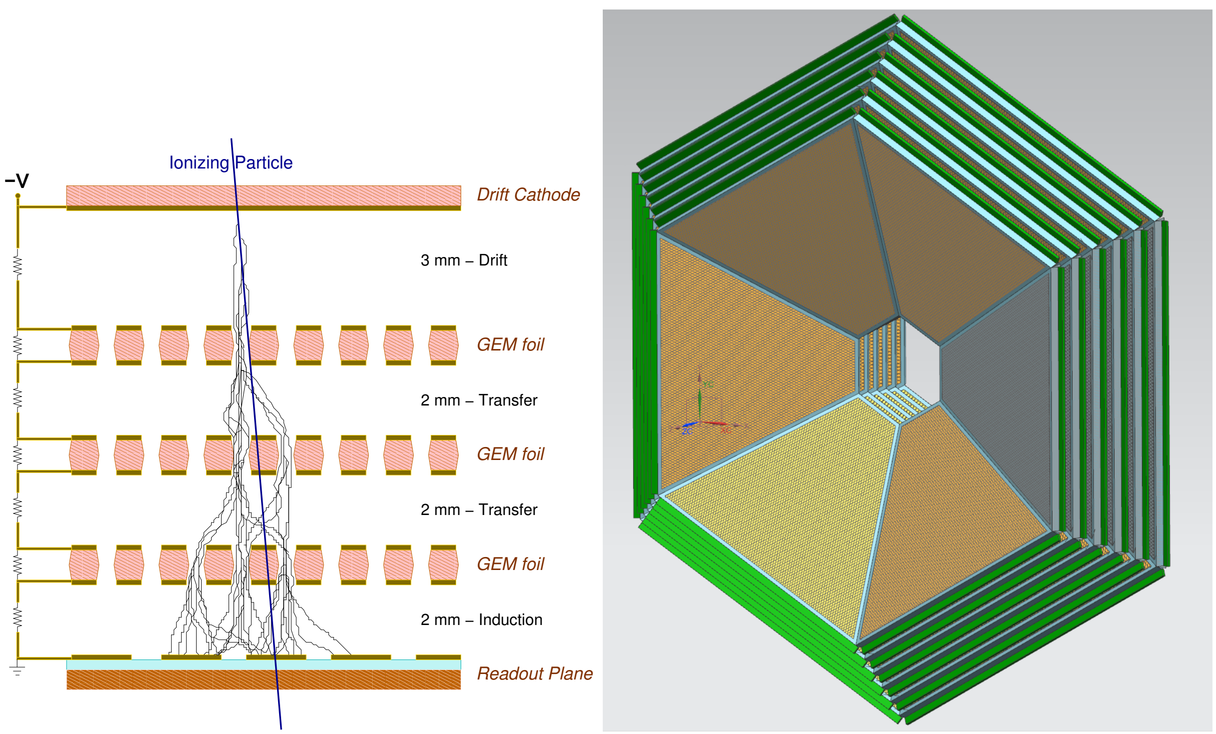

FIG. 24: On the left, the working principle of a triple GEM detector. On the right, rendering of a proposed 6-module GEM vertex tracker for μCLAS12.

We envision a six-station tracking system for μCLAS12 FVT, see Fig.24. Each station comprises six trapezoidal modules covering the 2π of azimuthal acceptance from 7° to 35° in polar angle. We plan to use a 2D COMPASS [108, 109] stereo strip readout, where U and V strips will be oriented parallel to the trapezoid's sides. With the expected pitch size of 0.5 mm, each module will have about 1200 readout channels. This arrangement will allow the readout front-end electronics to be placed at the trapezoid's base, outside of the detector acceptance. The first station will be at ~ 40 cm from the target. In the present concept, the longest strip in this design will be < 25 cm. Given the relatively small detector and short strip lengths and based on operational knowledge of GEM detectors for SBS, the proposed tracker can sustain rates of 250 kHz/cm^2 with expected position resolution better than 100 μm.

The members of our collaboration from the University of Virginia and the JLAB detector group are well-recognized experts in the field and have led the design and construction of several GEM trackers. The detector proposed for this experiment does not pose any challenges in terms of operational conditions or size.

3. Recoil tracker

A recoil detector is essential for tagging protons in quasi-real photoproduction reactions, such as time-like Compton scattering and light vector meson production, within the scattering angle range of 40° to 70°. In the forward region, the material budget of the tracking detector does not significantly impact track reconstruction quality, as the primary energy loss occurs within the shielding. Therefore, high-rate capable GEM detectors can be effectively utilized. In contrast, minimizing the material budget is crucial for low-energy recoil detection.

A promising candidate for recoil tracking detectors is the newly developed Micro Resistive Well (μRWELL) detector [110]. These detectors offer a low material budget and a relatively simple design, making them well-suited for high-precision tracking. Similar to GEM detectors, μRWELL detectors feature a drift region where passing charged particles ionize the working gas. However, unlike GEMs, μRWELL detectors utilize a single amplification stage, reducing material presence along the particle path.

The initial μRWELL prototype detectors had rate capability limitations, above 100 KHz/cm^2 gain drop is observed. This is mainly because the collected charge on the resistive layer could not dissipate fast enough, and the amplification field inside the wells was effectively reduced. In a recent couple of years, more developments in this direction allowed μRWELL detectors to withstand significantly higher rates (> 1 MHz) without compromising the gain [111]. This is achieved by adding more grounding lines on the resistive layer (PEP-groove and PEP-dots), significantly speeding up the charge evacuation. More details can be found in [111]. Currently, independent efforts are also ongoing to test high-rate μRWELL detectors within the CLAS collaboration by several INFN groups and also in Hall-B within the Laboratory Directed Research and Development (LDRD) grant (LD-2507).

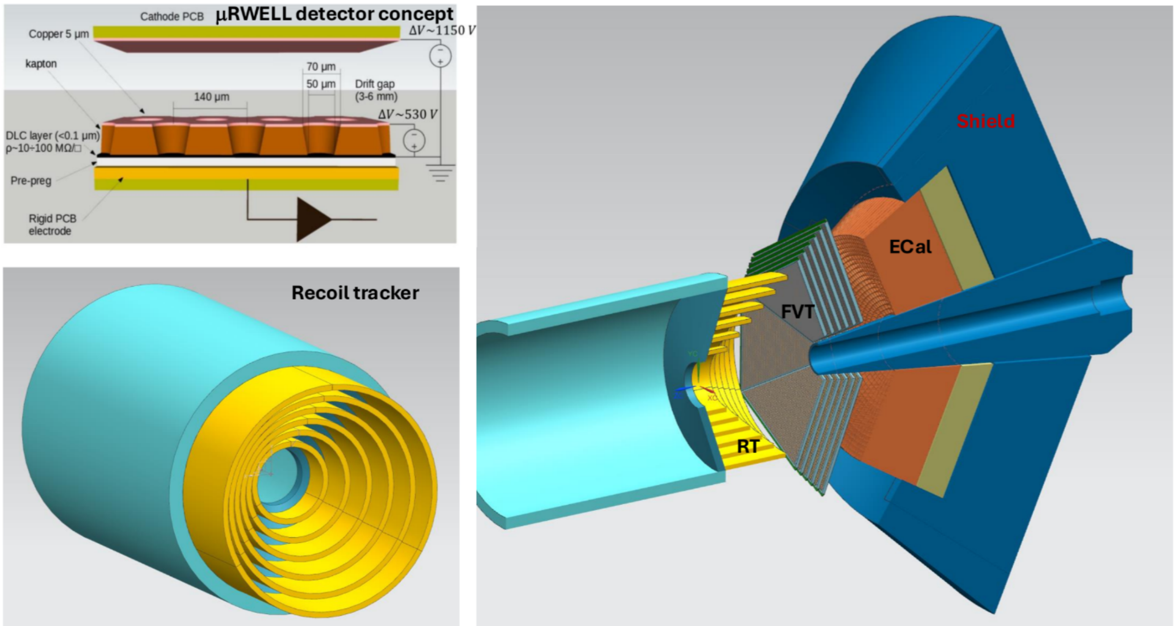

FIG. 25: On the left μRWELL MPGD concept (top) and the rendering of the barrel recoil detector (bottom). On the right, new detector elements of μCLAS12.

We plan to install a 6-layer, barrel-shaped μRWELL detector in place of the CLAS12 CVT, covering polar angles from $40° - 70°$. The conceptual design of the recoil tracker is shown in Fig.25. The top-left plot is a sketch illustrating the key components of the μRWELL detectors, while the bottom-left rendering depicts the barrel recoil tracker. The image on the right shows the new detector elements of μCLAS12.

The recoil tracker will consist of six concentric cylindrical layers, each composed of three sectors and featuring a 2D readout. The 2D strip configuration includes Z-strips (parallel to the beam direction) and C-strips (perpendicular to the Z axis), enabling precise measurement of both azimuthal coordinates and the “Z” coordinate of the hit. The strip pitch for both Z and C strips is 500; μm, ensuring high spatial resolution. The total number of readout channels for the entire detector is under 22K, which is well within practical limits for efficient data acquisition.

The CLAS12 collaboration has substantial experience in building and operating cylindrical Micro-Pattern Gaseous Detectors (MPGDs), including the BONUS GEM tracker and the Barrel Micromegas Tracker (BMT). These systems have been successfully tested and operated with a beam. In addition, ongoing R&D efforts are focused on developing cylindrical μRWELL detectors, as described in [112]. Over the next few years, we aim to validate these cylindrical μRWELL detectors for use in recoil tracking applications. Should technical challenges arise, an alternative option is to construct a GEM-based recoil tracker, leveraging the expertise and existing infrastructure within the CLAS12 collaboration.

B. Beamline and Target

The proposed luminosity of 10^{37} cm^{-2} sec^{-1} will be achieved with a $\sim$ 7.5 cm-long liquid hydrogen (LH_2) target and an electron beam of up to 7 μA. With a few modifications, the Hall-B beamline will support high-current beam operation. The primary upgrade requirement is increasing the beam dump power. In 2021, we started a two-phase upgrade of the Hall-B beam dump. The first phase is completed, enabling the dump to handle a 17 kW beam on an insertable water-cooled beam blocker and up to 1 kW on the Faraday cup. The second phase is planned for the next couple of years. Several options are under consideration and will increase beam dump capacity to up to 100 kW, allowing operation at required beam currents for this experiment.

We will use the Hall-B liquid hydrogen target positioned at the center of the solenoid magnet. The 7.5 cm-long target cell is slightly longer than those used in current CLAS12 experiments. Unlike the current design, which uses a Kapton cell with aluminum windows, the new target cell will be constructed entirely from aluminum to enhance thermal performance and improve heat dissipation from the beam, ensuring stable operation under high beam intensity conditions. While beam heating will not be an issue keeping liquid hydrogen in the cell, it is expected to have some density fluctuations. A density fluctuation because of local boiling is not uncommon for high-power targets, and a typical mitigation is to take luminosity scan data to track density changes as a function of beam current.

C. Background studies and luminosity limits

The CLAS12 GEANT4 simulation software, GEMC [95], has been modified to enable studies of backgrounds, detector occupancies, event reconstruction, and experimental reach for the new configuration. We integrated in GEMC the μCLAS12 CAD model for the new detector components while preserving the existing CLAS12 framework. This approach enabled the use of the CLAS12 event reconstruction framework, COATJAVA [97], for realistic event reconstruction, providing a foundation for conducting physics analyses.

GEMC has been optimized and validated over the years against experimental data across various beam energies and target configurations. The most critical aspects of the Monte Carlo (MC) tool for our study are background rates and detector occupancies from electron-target interactions, particle energy loss (ensuring an accurate material budget for detectors), and energy and time resolutions (e.g., for fECal).

Figure 26 presents a comparison of measured and simulated drift chamber occupancies during the RG-A run, where 50 nA, 10.6 GeV electrons impinged on a 5-cm long LH_2 target. The simulated beam background reproduces the observed occupancies within 15%. Another comparison, shown in Fig. 27, illustrates the energy depositions from charged pions for both data and simulation across the three fECal regions (PCal, ECIn, and ECOut) alongside the simulated muon energy loss. The simulation of the calorimeter energy response demonstrates good agreement with the experimental measurements.

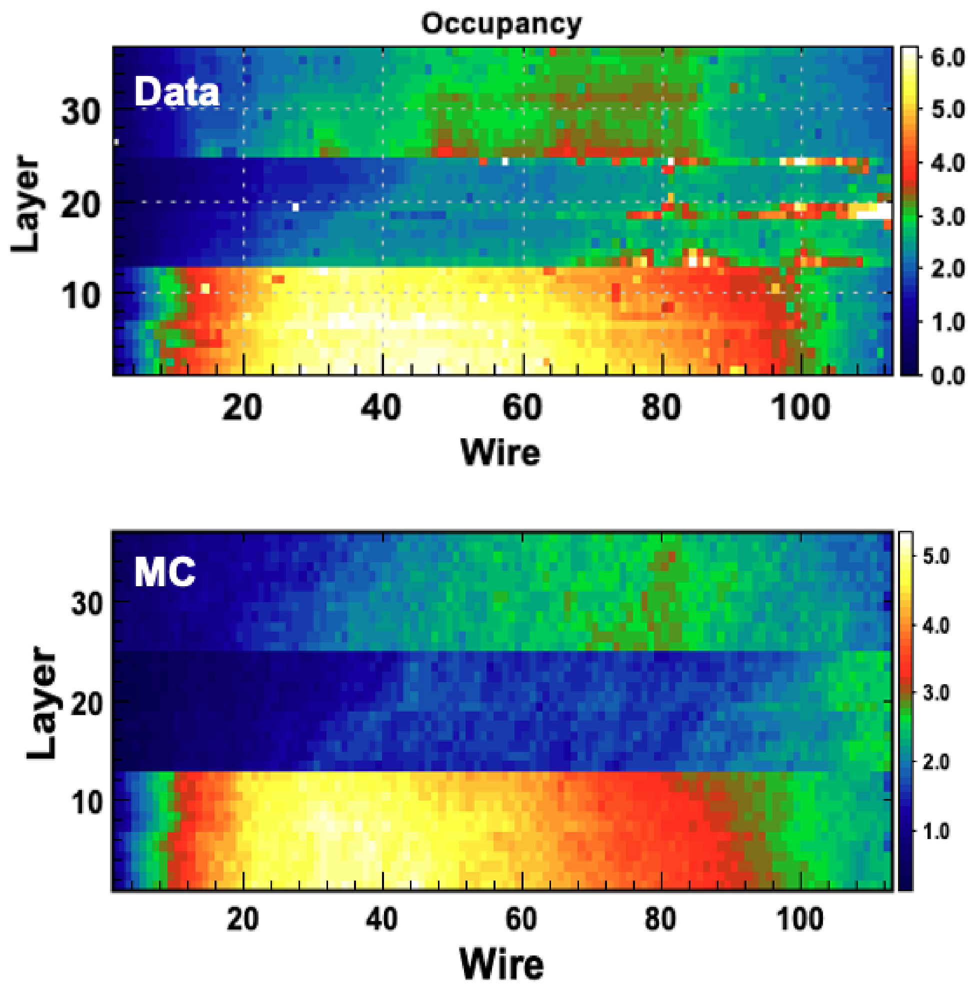

FIG. 26: DC occupancies as measured in CLAS12 and simulated in GEMC.

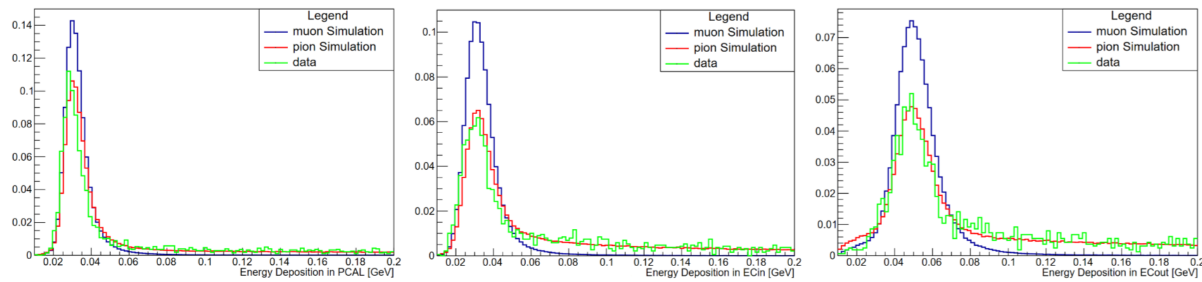

FIG. 27: The energy distribution for minimum ionizing particles ($\pi^{\pm}$) in the fECal module, PCal, ECIn, and ECOut. The green distributions are for data from RG-A, the red histograms are MC for $\pi^{\pm}$, and the blue histograms are for simulated $\mu^{\pm}$. The histograms are normalized to the total number of each sample.

These validations demonstrate that GEMC accurately reproduces CLAS12 detector performance, and the newly created MC tool, μGEMC for μCLAS12, as shown in Fig.28, is well suited to assess the feasibility of the proposed measurements.

Several different material types and thicknesses of the shield downstream of the wECal have been studied to optimize occupancies in DC Regions 1 and 2, π/μ separation, muon energy loss, and the muon momentum resolution. We found a 30 cm thick tungsten or lead acceptable for DC. The lead option is preferable from an engineering point of view as a cost-effective and easy-to-make solution. The final decision will be made after all MC studies are completed[1]. Below, we present the current state of the background simulations with occupancies and rates in the detectors.

1. *DC Occupancies*

The drift chamber occupancies have been studied with both lead and tungsten shielding. Fig.29 shows the occupancies generated from the interaction of a 11 GeV electron beam with LH_2 target at a luminosity of 10^{37} cm^{-2}s^{-1} with a 30 cm thick lead shield. The average occupancies, shown in the top plot, are approximately 9%, 11%, and 15% for Regions 1, 2, and 3, respectively.

In previous CLAS12 experiments with nuclear targets, DCs have been operated with occupancies close to 10%. High occupancies will impact tracking deficiency and momentum resolutions. However, it is important to note that occupancies in Regions 1 and 2 are primarily concentrated in the very forward and very backward areas of these regions, respectively. Region 1 covers the

[1] MC studies of the background and shield optimization are ongoing. We will have a final working solution before the PAC submission deadline

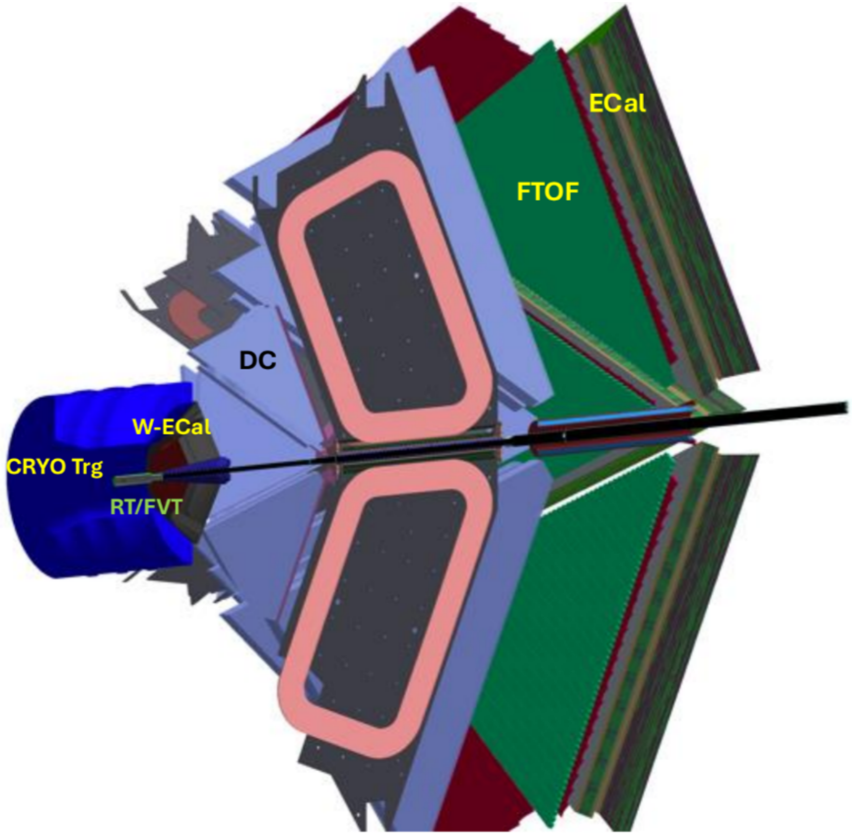

FIG. 28: GEANT4 rendering of the μCLAS12 detector, μGEMC.

angular range starting from 5°, while μCLAS12 aims to detect tracks in the forward detector above 7°. As a result, the high-occupancy area corresponding to the first 15 wires of Region 1 will not significantly affect its performance. Similarly, the high-occupancy area in the backward part of Region 2 corresponds to scattering angles near 40°, which are outside the μCLAS12 acceptance.

The primary challenge lies in Region 3, where the occupancy is the highest and covers a substantial portion of the detector. Ongoing studies aim to better understand the sources and nature of the background, as well as to optimize the shielding configuration. Available MC data indicate that a significant portion of the background originates from electrons produced between the downstream end of the torus magnet and the forward carriage, with a non-negligible contribution from the forward carriage itself. Notably, the energy of these background electrons is low. This is evidenced by the introduction of a 2 mm carbon shell, which effectively reduced the average occupancy in Region 3 from 20% (shown in the right graphs of Fig.29) to 16% (shown in the left graphs).

Further improvements in shielding and background mitigation are being actively investigated to ensure that optimal detector performance in high-occupancy conditions will be achieved.

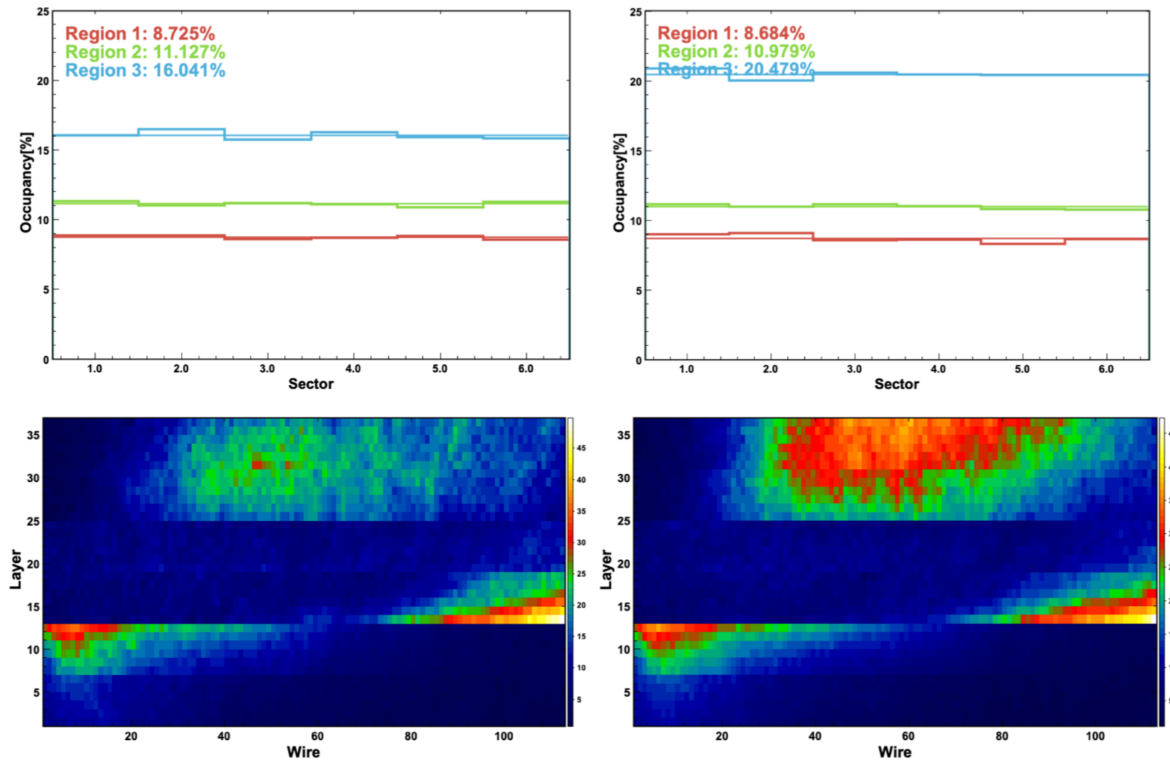

FIG. 29: The drift chamber occupancies at the luminosity of $10^{37}\mathrm{cm}^{-2}\mathrm{s}^{-1}$ with a 30 cm thick lead shield downstream of the $PbWO_4$ calorimeter. Left: occupancies with a 2 mm thick carbon shell on the back of the Region 3 DCs. Right: occupancies without the carbon shell. The top plots show the average occupancies per sector, and the bottom plots are occupancies as a function of the DC write number for three regions.

2. Rates in the forward GEM tracker

A scoring plane was implemented in μGEMC at a distance of 40 cm from the target center to estimate hit rates in the forward GEM tracker. Any particle with energy exceeding 10 keV that crossed the plane within the angular range of 7° to 30° was counted as a hit.

Figure 30 shows the flux distribution of charged and neutral particles at a luminosity of 10^{37} cm^{-2}sec^{-1}. In the region close to the beam, the total rate, predominantly composed of photons, is approximately 20 MHz per cm^2. Extensive studies with GEM detectors indicate that only 0.5% of photons with energies greater than 10 keV will produce a detectable signal in the tracker. Taking this factor into account, along with the charged particle rate of about 450 kHz/cm^2 at the very forward region, we estimated the highest detectable rate to be less than 500 kHz/cm^2.

In the current GEM design, the longest strip covers an area of about 1.2 cm^2, stretching from very small angles with the highest rates to larger angles where rates decrease to around 50 kHz/cm^2. Averaging the rates over the entire tracker area yields a detectable hit rate of less than 300 kHz/cm^2 per GEM module.

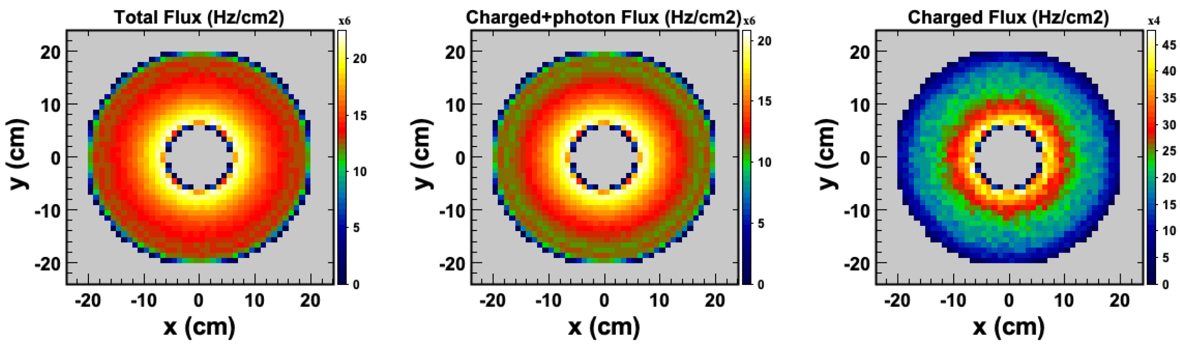

FIG. 30: Rates of particles with more than 10 keV energy at a luminosity of 10^{37} $\text{cm}^{-2}\text{sec}^{-1}$ crossing the scoring plane at 40 cm from the target center. Left: total rate; Middle: the rate charged particles and photons; and Right: the rate from charged particles only.

3. Rates in the $PbWO_4$ calorimeter

The rates in the calorimeter were estimated using data from a scoring plane positioned at 60 cm from the target center. Figure 31 shows the flux distribution of charged and neutral particles at a luminosity of 10^{37} $\text{cm}^{-2}\text{sec}^{-1}$ within the acceptance range of wECal, considering particles that deposit at least 15 MeV of energy in the calorimeter.

The highest observed rate is approximately 1 MHz/cm^2 in the region close to the beam, predominantly driven by photons. In contrast, the rate of charged particles in this region is about 200 kHz/cm^2. The forward calorimeter module, made of $PbWO_4$, has dimensions of $1.3 \times 1.3 \times 20$ cm^3, covering an area of approximately 1.7 cm^2. Therefore, the highest hit rate in a single module with a 15 MeV energy threshold is estimated to be less than 2 MHz.

This rate is considered manageable, as similar calorimeters (e.g., the HPS calorimeter) have operated efficiently under comparable rates in modules situated close to the beam.

4. Rates in the recoil tracker

The rates in the recoil tracker were estimated using data from a cylindrical scoring plane positioned at a radius of 30 cm from the beam. Figure 32 shows the flux distribution of charged and

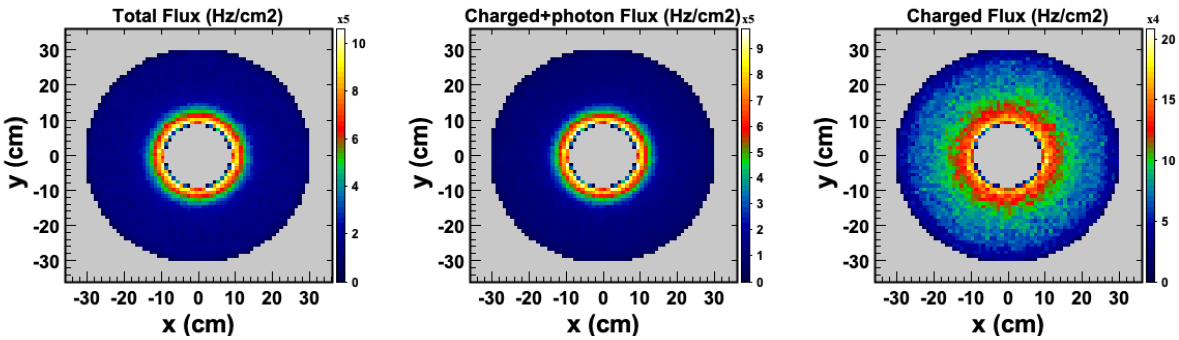

FIG. 31: Hit rates at the scoring plane before wECal at the luminosity of 10^{37} cm^{-2}sec^{-1}. Left: the rate for different particles as a function of polar angle with 15 MeV energy cut in the wECal. Right: the rate from charged particles with the same energy cut.

neutral particles at a luminosity of 10^{37} cm^{-2}sec^{-1}. The left panel of the figure presents the rates for different particle types with a 10 keV energy threshold as a function of polar angle.

The highest flux is attributed to photons, reaching approximately 300 MHz at small angles (30°). Neutrons contribute the next highest rate, while charged particles exhibit a rate of about 10 MHz. The longest strips in the recoil tracker are Z-strips with a pitch size of 500 μm, covering an area of approximately 3 cm^2 at a 30 cm radius.

Taking into account a 0.5% detection efficiency for photons, the estimated rate per cm^2 for the recoil tracker is less than 250 kHz/cm^2, which remains within the acceptable operational range.

D. Trigger rates and DAQ

The trigger for the proposed experiment is a charged track with Minimum Ionizing Particle (MIP) energy deposition in the forward electromagnetic calorimeter (fECal). To estimate the rate of a single MIP trigger in μCLAS12, we utilized data from the CLAS12 RG-A experiment (a 10.6 GeV electron beam impinging on a 5 cm long LH_2 target), where data were collected using multiple trigger settings. One of these settings involved a single fECal hit with energy greater than 10 MeV. The raw rate of this trigger (TB8) at a luminosity of approximately 0.6×10^{35} cm^{-2} sec^{-1} was about 250 kHz, and data from TB8 were recorded with a pre-scale factor of 2049.

Analyzed data sample with the TB8 yielded around 11000 events containing at least one positively or negatively charged track with energy in the fECal below the MIP energy threshold of 300 MeV. To estimate the rate in μCLAS12, this number must be corrected for the pre-scale factor (×2049) and accounting for the luminosity difference between the analyzed data and the proposed

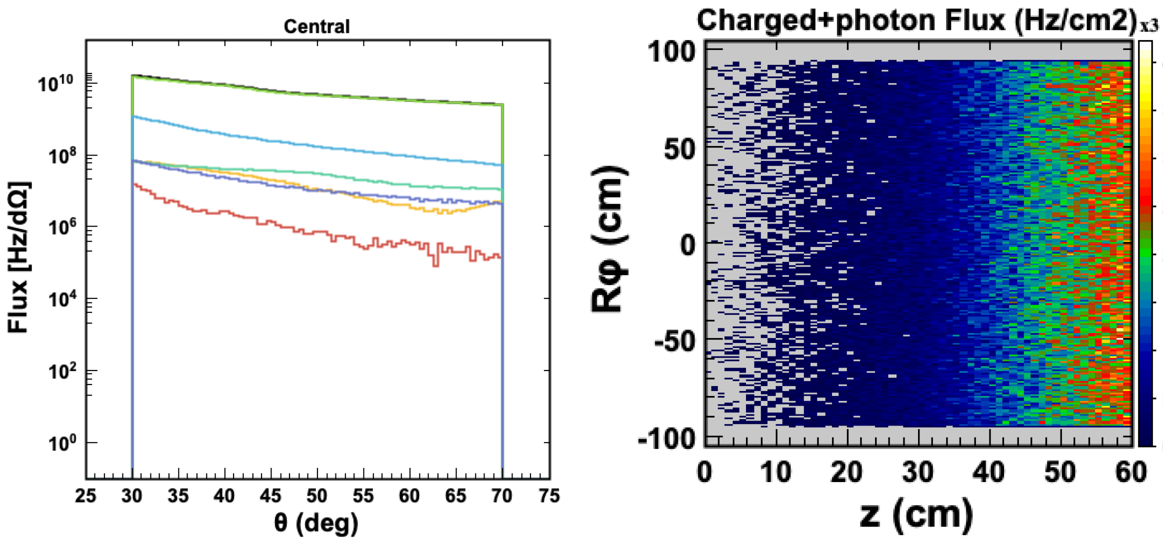

FIG. 32: Rates of particles at the cylindrical scoring plane located at 30 cm radius from the beam at the luminosity of 10^{37} cm^{-2}sec^{-1}. Left: the rates for different particle types with 10 keV energy cut as a function of polar angle. Right: azimuthal and z distribution of rates of photons and charged particles.

luminosity of 10^{37} cm^{-2} sec^{-1} ($\div 52.7$). We also considered the survival fraction of charged hadrons through the wECAL and the shield from GEANT4 MC, which is approximately 0.01. Based on these corrections and considerations, we estimated a single trigger rate of 21 kHz.

The CLAS12 Data Acquisition (DAQ) system currently achieves a trigger acceptance rate of 30 kHz with a live time greater than 90%, significantly exceeding the proposed experiment's expected trigger rate. During routine operations, the CLAS12 DAQ typically runs at rates exceeding 20 kHz, with a data throughput of approximately 800 MByte/sec. The transition from CLAS12 to μCLAS12 will result in a nearly unchanged total channel count since the additional channels from new detectors will be compensated by those that are removed or replaced.

Furthermore, the CLAS12 DAQ system is undergoing a major upgrade to support Streaming Readout (SRO), which will enable triggered DAQ operation at up to 70 kHz. If SRO becomes available by the time of the experiment, we will leverage it to record a broader range of physics final states, enhancing the scientific output.

E. Event reconstruction and muon identification

1. *Pion survival rates*

The electromagnetic background generated in the target is effectively absorbed by wECal and the shield, significantly reducing the background on the forward detector. The primary background in the forward detector and the true muon sample will originate from charged pions. Although the calorimeter and shield will absorb a significant fraction of these pions, some will still pass through, make a track in DC, and deposit energy in fECal. Figure 33 illustrates how 6 GeV/c π^+ and μ^+, generated using a GEANT4 particle gun, interact with the calorimeter and shield before being detected in the CLAS12 forward detector. As seen in the left rendering, most pions will shower in wECal, preventing them from leaving a measurable trajectory in the drift chambers or a minimum ionizing particle (MIP) signature in fECal. Only a tiny fraction, $\lesssim 1\%$, will be detected in the forward detector, either directly or through secondaries. In contrast, $> 80\%$ of muons will pass through wECal with some energy loss and remain detectable in the drift chamber and fECal.

The strategy for muon identification relies on their characteristic energy deposition signature in the forward calorimeter modules, as shown in Fig.27. Another key distinguishing feature is the transverse profile of the energy distribution, specifically the number of calorimeter strips involved in the energy reconstruction. Pions, which can shower in the calorimeter, produce a wider transverse shower profile and involve many strips. A limit imposed on the number of strips involved in calorimeter hit reconstruction will further suppress pion contamination. Figure 34 demonstrates the effect of this cut, showing the distribution of the fECal sampling fraction ($SF = E_{cal}/p$) as a function of momentum (p) for positively charged particles reconstructed from generated π^+s at the target. After applying the strip-count cut, only particles with a clear MIP energy signature remain. In the future, more sophisticated algorithms with the inclusion of ML techniques will be employed for π-μ separation.

To estimate pion contamination in the MIP (muon) sample, 3 million pions of both charges were simulated with uniform momentum and angular distributions using the GEANT4 particle gun. The CLAS12 event reconstruction framework was then used to reconstruct and identify particles reaching the forward calorimeters. Figures 35 and 36 display the fraction of positively and negatively charged tracks reconstructed as MIP particles originating from the initial π^+s and π^-s samples, respectively. Overall, the survival rate of pions is $< 0.8\%$. Due to secondary particles generated in wECal, a negatively (positively) charged MIP track can occasionally be reconstructed from the original π^+ (π^-) sample, albeit with very low efficiency ($< 0.2\%$). We require pairs of

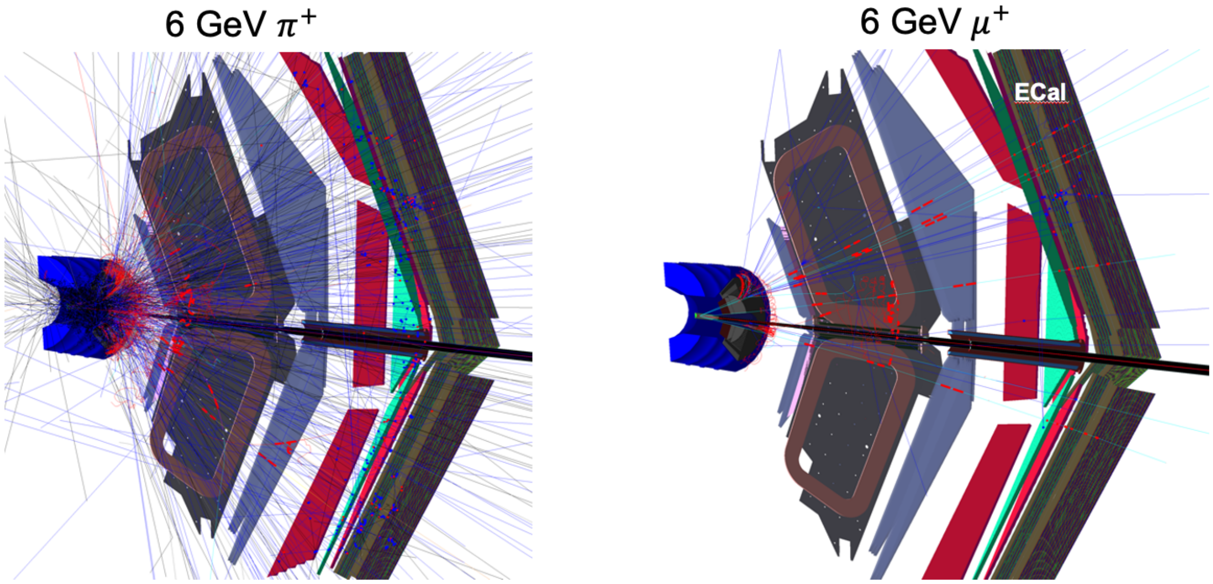

FIG. 33: Simulation of 6 GeV/c π^+s and μ^+ through the μCLAS12 GEANT4 model. Almost all pions interact in the wECal while muons punch through and get reconstructed in DC and fECal.

MIP tracks for physics analysis, and the above results ensure that pion pairs are suppressed in the muon pair sample by at least 5×10^{-5}.

2. *Muon energy loss and momentum resolution*

Muons with momentum above approximately 1.5 GeV/c will penetrate the wECal and shielding, albeit with significant ionization energy loss that can reach up to a GeV, as shown in Fig. 37. After passing through the wECal and shield, muons that retain enough energy to traverse the torus field and reach the fECal will undergo momentum analysis in the drift chambers. However, the reconstructed momentum will correspond to the momentum after energy loss. Therefore, momentum corrections are necessary to restore the muon momentum at the production vertex. These corrections are crucial for accurate vertexing of the track and for determining the angles and position at the production point as the particles pass through a 5 T solenoid field.

The momentum corrections are derived from simulations by examining the dependence of the energy loss on the reconstructed momentum, where the energy loss is defined as a difference between reconstructed and generated momenta, $\Delta P = P_{rec} - P_{mc}$. The bottom row of Fig. 37 shows the relative energy loss of negatively (left) and positively (right) charged muons as a function of reconstructed momentum. The distributions of $\Delta P/P_{rec}$ versus P_{rec} were parametrized as polynomial functions and used for the muon energy loss corrections. These functions are depicted

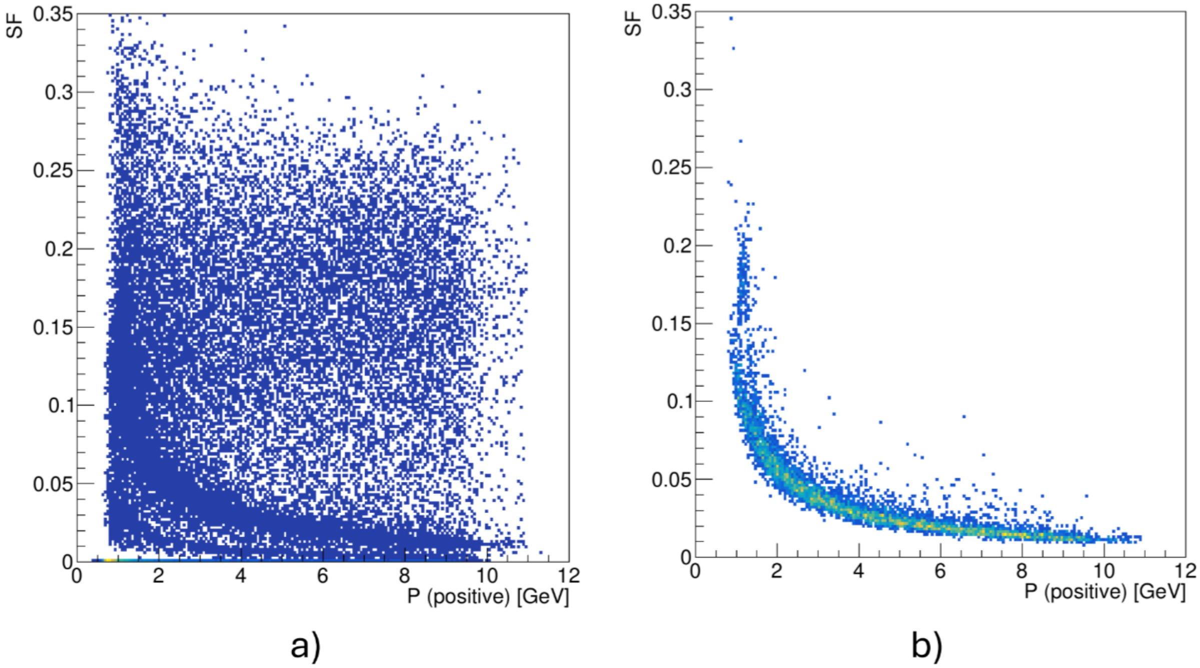

FIG. 34: A forward-ECal sampling fraction ($SF = E_{cal}/p$) vs. momentum for π^+s that passed the calorimeter-shield and end up in fECal. Distribution in a) is for all pions, and b) those who survived a number of fECal strip cuts to select true MIP particles.

as red curves in the bottom row of Fig. 37.

One of the key kinematic variables for identifying the reaction ep $\rightarrow$ e$'\mu^-\mu^+$p is the missing mass of the final state e$'\mu^-\mu^+$X, where the missing proton must be identified through missing momentum analysis. In Fig. 38, the missing mass squared distributions of the reconstructed e$'\mu^-\mu^+$ final state from the simulation of Bethe-Heitler (BH) events through μCLAS12 are presented. The black distribution corresponds to the missing mass calculated with the reconstructed momenta of muons, while the red distribution shows the result after applying muon energy loss corrections. A significant improvement in the missing mass squared distribution of the missing proton is evident after implementing momentum corrections.

In addition to energy loss, multiple scattering significantly degrades the angular resolution. The FVT's primary purpose is to measure precisely the vertex angles of muons and electrons. It is expected that the reconstructed angles, aided by the FVT, will be sufficiently accurate that no further corrections would enhance the resolution of kinematic variables. Therefore, at this stage, the angles of the reconstructed muons are corrected by assigning the corresponding generated values. This angular correction significantly improves the missing mass distribution, as demonstrated by

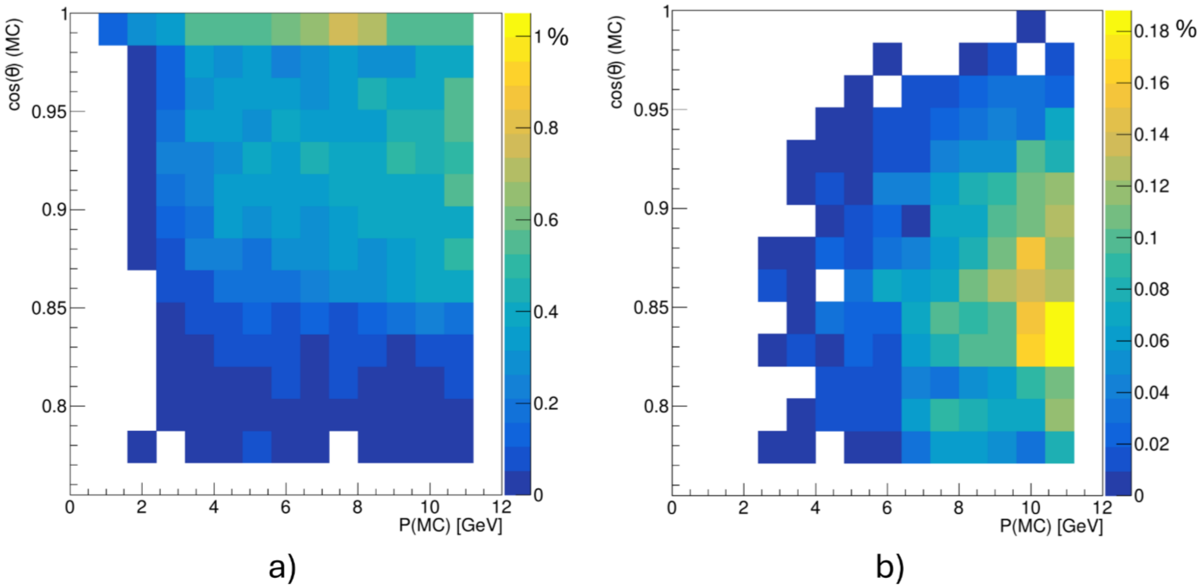

FIG. 35: A distribution of the fraction of positively (a) and negatively (b) charged MIP particles from simulated 3M π^{+}s after cuts on the number strips in fECal. The original sample of pions was generated uniformly in momentum and $\cos\theta$ using a GEANT particle gun.

the green histogram in Fig. 38.

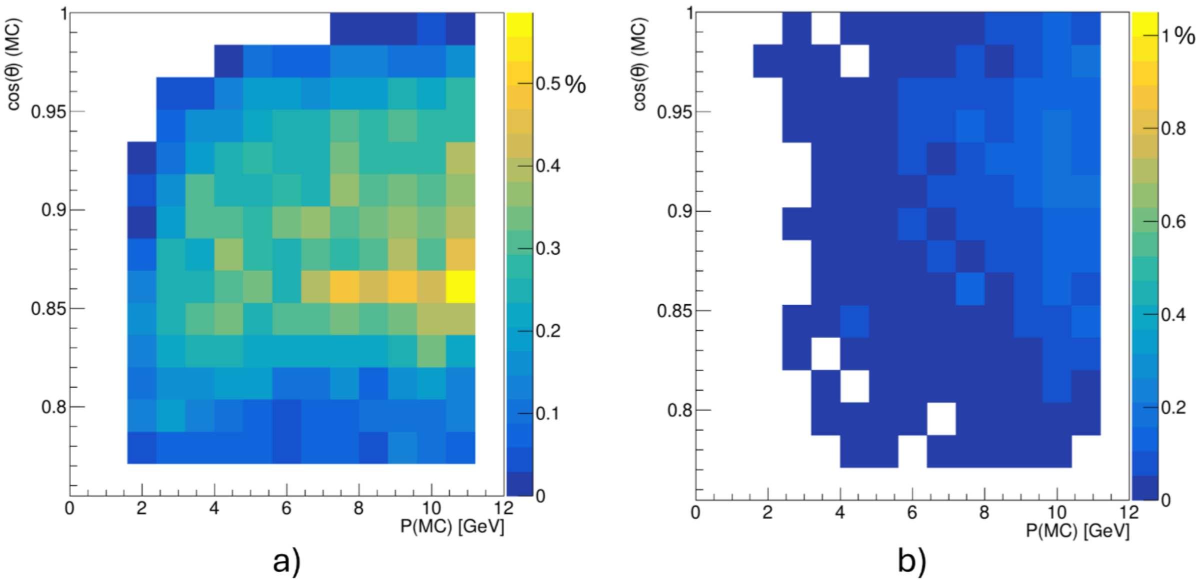

FIG. 36: A distribution of the fraction of negatively (a) and positively (b) charged MIP particles from simulated 3M π^{-}s after cuts on the number strips in fECal. The original sample of pions was generated uniformly in momentum and $\cos\theta$ using a GEANT particle gun.

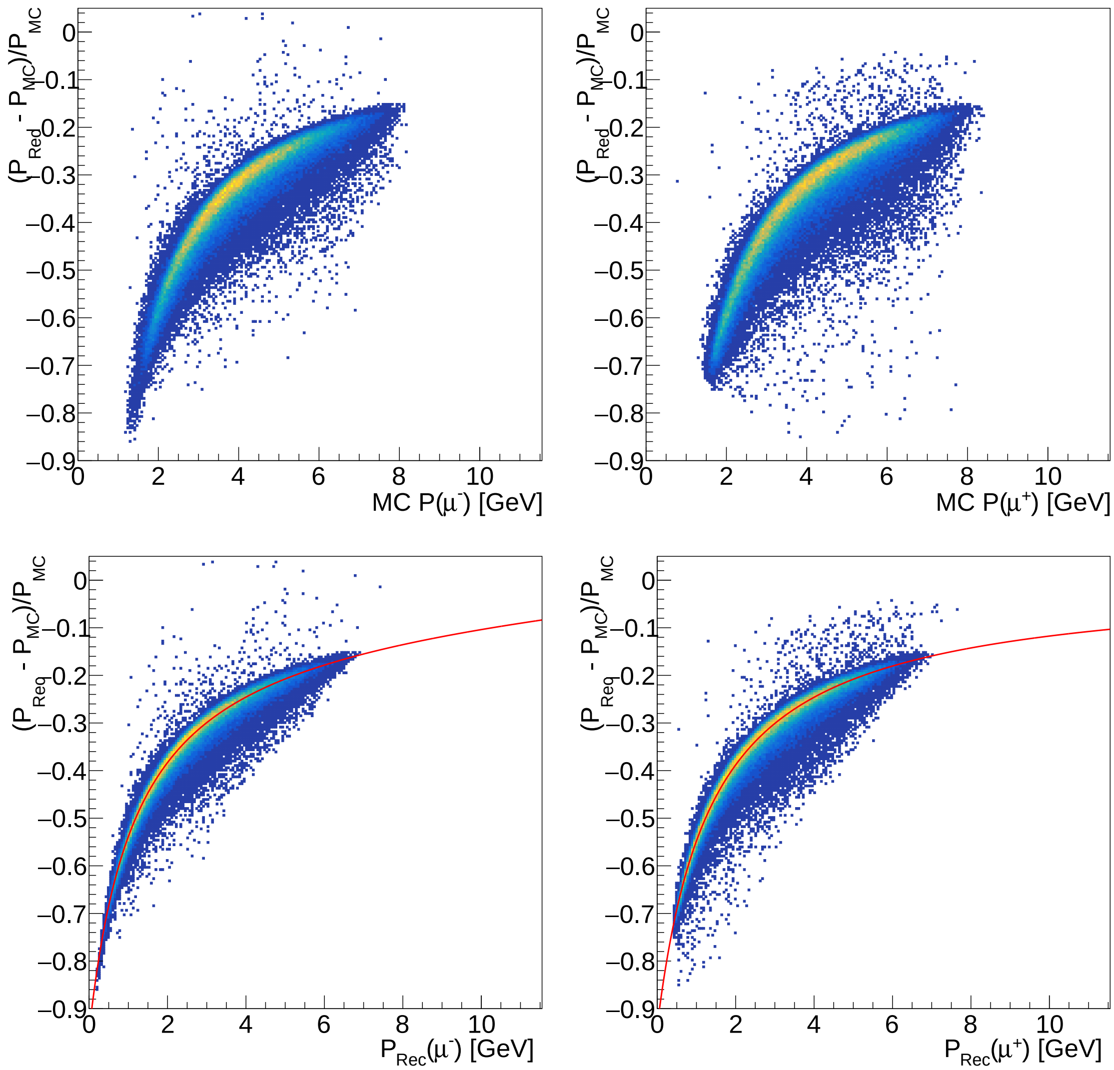

FIG. 37: Relative momentum loss (ΔP/P) as a function of generated momenta (top row) and reconstructed momenta (bottom row). correspond to negatively charged muons, while those on the right correspond to positively charged muons. The red curves in the bottom plots indicate the corresponding correction functions..

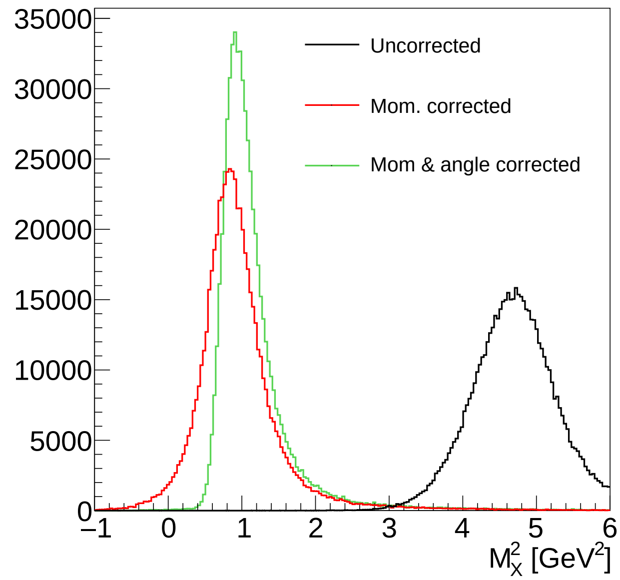

FIG. 38: The missing mass squared distribution of the reaction ep $\rightarrow$ e$'\mu^-\mu^+$X. The black distribution corresponds to the uncorrected data, the red distribution is obtained after applying momentum corrections to both muons, and the green distribution shows the result after additionally correcting the polar and azimuthal angles. .

F. Physics backgrounds

There are multiple sources of background reactions that can generate the desired final state particles and can potentially contribute to the measurement of the main physics reaction, $ep \to e'\mu^-\mu^+(p)$. The most significant background sources are listed below:

- **Inelastic muon pair production:**

  Reactions of the type $ep \to e'\mu^-\mu^+(X)$, where $X \neq p$. These are di-muon final states where the missing hadronic mass is close to the proton mass, allowing them to pass the missing mass cuts defined by the detector resolution. An example of such a background reaction is $ep \to e'\mu^-\mu^+(\pi N)$,

- **Pion pair production:**

  Reactions such as ep $\to$ e$'\pi^-\pi^+$(X), where both pions pass the MIP selection cuts, lead to a final state that also passes the missing mass cut.

- **Accidental coincidences:**

  These occur when two MIP events coincide in the forward detector along with an electron-like hit in wECal, which is associated with an inclusive electron. This situation arises when $\mu^+\mu^-$ or $\pi^+\pi^-$ pairs are produced by an electron scattered at a small angle (close to 0°) and escape detection, while another electron from the same beam bunch is detected along with the MIP pair.

1. *Inelastic muon pair production*

The di-lepton event generator GRAPE [113], extensively utilized in HERA data analysis, is capable of generating both elastic ep $\to$ e$'\mu^-\mu^+$p and inelastic ep $\to$ e$'\mu^-\mu^+$X (X $\neq$ p) reactions. To estimate the contribution from inelastic muon pair production, events were generated with an invariant mass cut of M($\mu^-\mu^+$) $>$ 1.2 GeV, corresponding to the region of interest for this proposal. These events were passed through μGEMC and subsequently reconstructed using CLAS12 reconstruction tools.

The contribution of inelastic events to the elastic final state was evaluated by analyzing the missing mass distribution of $e'\mu^-\mu^+$ events after applying momentum corrections for muons and smearing electron momentum for the expected resolution of wECal $\sigma/\sqrt{E} = 4\%$. Figure 39 shows normalized missing mass squared distributions for both elastic (blue) and inelastic (red) events. The dashed vertical lines indicate cuts on the missing mass squared to identify elastic scattering, defined as $0.4\ \mathrm{GeV}^2 < \mathrm{M}_\mathrm{X}^2 < 1.5\ \mathrm{GeV}^2$. The fraction of inelastic reactions within this cut is approximately 5.5%.

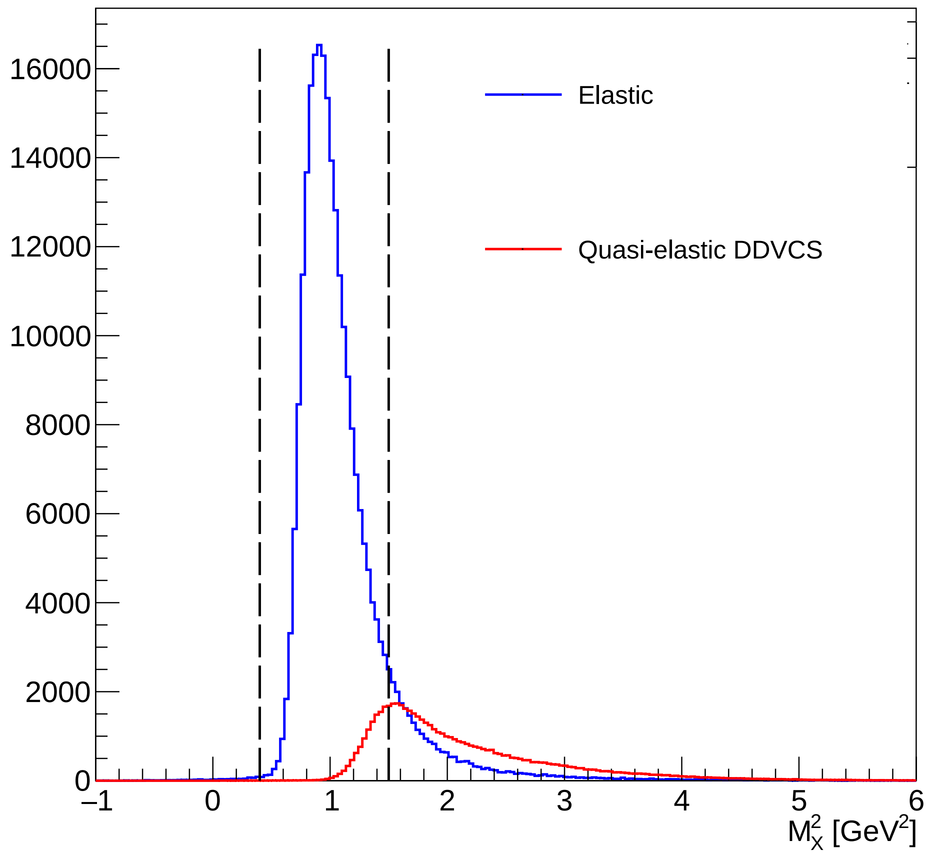

FIG. 39: Missing mass squared distribution for elastic (blue) and inelastic (red) muon pair production. Vertical dashed lines represent the missing mass cut.

2. Pion pair production

To estimate the pion pair background, we analyzed CLAS12 electroproduction data from 10.6 GeV electron scattering on a 5 cm long liquid hydrogen target. Data corresponding to about 4.27 fb^{-1} integrated luminosity is examined, and events containing at least one $\pi^-\pi^+$ pair were selected (approximately 180 million events). This corresponds to about 41 nb of detection cross-section. These events were processed through μGEMC and reconstructed using the CLAS12 event reconstruction tool. This approach provides the best approximation for pion pair electroproduction in our study since any pions that can be detected as MIPs with μCLAS12 will also be detected in CLAS12.

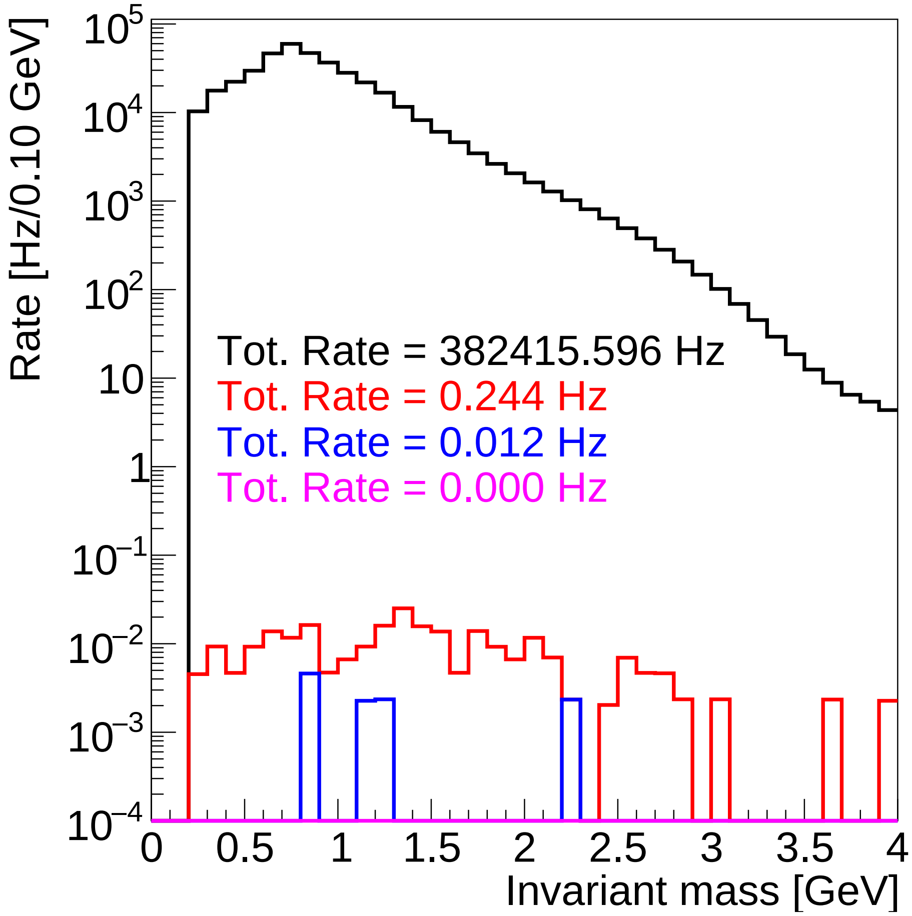

FIG. 40: Rates of pion pairs as a function of 2-MIP particle invariant mass. The black distribution represents all initial pairs selected from CLAS12 data, the red represents events when at least one pair of oppositely charged MIP particles is detected, and the blue histogram corresponds to evens when an electron is detected in the μCLAS12 calorimeter. Pink, with no events, is from the three-particle final state that satisfies the missing mass cut. The numbers in the figure represent the total integrated rates for the corresponding histogram.

Figure 40 shows the expected rates as a function of the invariant mass of two MIP particles at various analysis stages, normalized to a luminosity of 10^{37} cm^{-2} sec^{-1}. The black histogram represents all initial pion pairs, while the red histogram corresponds to events where both pions are reconstructed as MIPs in μCLAS12. The blue histogram shows events where an electron is identified in wECal in addition to the MIPs. Finally, the pink histogram (with zero events) corresponds to events that pass the missing mass squared cut on the $ep \to e'\mathrm{MIP}^-\mathrm{MIP}^+X$ final

	Inclusive	Dilepton elastic	Dilepton quasi-elastic
cross-section [pb]	152004	4.3633	0.6959
e^- momentum range	0.5 GeV - 10.6 GeV	No cut	No cut
e^- θ range	7 deg - 38 deg	No cut	No cut
$\mu^{-/+}$ momentum range	N/A	0.5 GeV - 10.6 GeV	0.5 GeV - 10.6 GeV
$\mu^{-/+}$ θ range	N/A	5 deg - 40 deg	5 deg - 40 deg

TABLE I: summary information for inclusive and dilepton generated events before the merging.

state.

The analyzed statistics did not produce any pion pair events with a detected electron that could be reconstructed as $e'\mu^-\mu^+$ and pass the missing mass squared cut. However, with the rate of reconstructed $e'\mathrm{MIP}^-\mathrm{MIP}^+$ events, we can confidently conclude that the contribution from the pion pair production to the $e'\mu^-\mu^+$ final state is a few times smaller than the true rate of the $ep \to e^-\mu^-\mu^+$ reaction, 0.03 Hz, and the implementing the missing mass squared cut is expected to reduce this background by an additional order of magnitude.

3. *Accidental coincidence with inclusive electron*

Accidental coincidences occur when a reconstructed MIP particle pair and an electron from an unrelated event are detected within the time window of a single beam bunch. To estimate the fraction of these coincidences, we generated inclusive electrons separately using the IncEG generator [114], which accurately reproduces CLAS12 inclusive electron scattering data [115]. Additionally, we generated muon pairs with GRAPE [113] (both elastic and inelastic) without imposing any constraints on the scattered electron momentum.

The inclusive electron events from IncEG and all particles from the GRAPE generator were combined to form new mixed events. These events were then processed through the μGEMC simulation and reconstructed using the CLAS12 reconstruction framework.

We use the known cross sections for di-muon production and inclusive electron scattering to calculate the coincidence rate. The coincidence rate is given by:

$$\mathrm{R_C} = \sigma_{\mathrm{Incl}} \times \mathrm{L} \times \sigma_{\mathrm{dilepton}} \times \mathrm{L} \times 4\ \mathrm{ns} \quad (31)$$

where $\mathrm{R_C}$ is the coincidence rate, L is the luminosity, σ_{Incl} is the inclusive cross-section, and $\sigma_{\mathrm{dilepton}}$ is the dilepton production cross-section from GRAPE.

Cross sections and kinematic cuts applied to particles in the IncEG and GRAPE simulations are summarized in Table I. While the rate of accidental coincidence muons is comparable to the rate of pure BH electroproduction events, energy and momentum conservation cuts suppress those accidentals significantly.

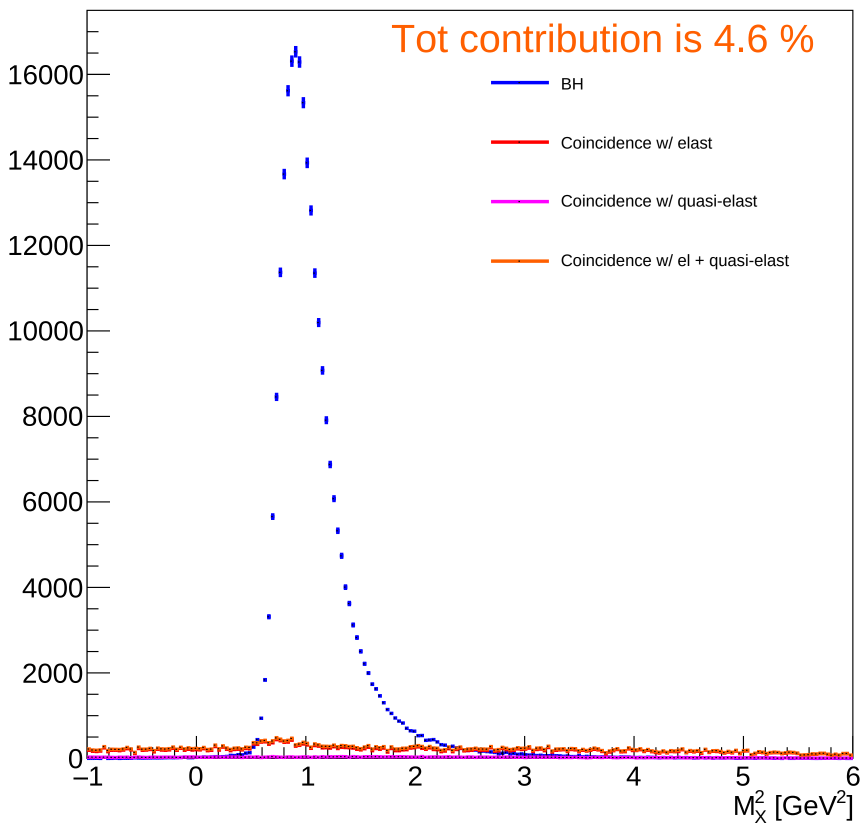

FIG. 41: Missing mass squared distribution electron-2MI P events for 200 days of running at $10^{37}\mathrm{cm}^{-2}\mathrm{s}^{-1}$ luminosity. The blue distribution represents BH events, red represents the accidental coincidence of inclusive electrons and elastically produced muon pairs, pink is the coincidence with inelastic muon pairs, and orange is the sum of elastic and inelastic coincidences.

Figure 41 shows the missing mass squared distribution of electron/di-muon final states for 200 days of running at a luminosity of $10^{37}\mathrm{cm}^{-2}\mathrm{s}^{-1}$. The distribution includes both true electroproduction of BH di-muons and accidental coincidences. The blue histogram corresponds to pure BH events, the red points show accidental coincidences of inclusive electrons with elastic muon pairs, the pink points represent coincidences with inelastic muon pairs, and the orange histogram is the sum of elastic and inelastic contributions. In the missing mass squared range $0.4\ \mathrm{GeV}^2 < \mathrm{M}_\mathrm{X}^2 < 1.5\ \mathrm{GeV}^2$, the total contribution from accidentals is under 5%.

IV. PROPOSED MEASUREMENTS

The experiment will measure the production of muon pairs in electron-proton scattering (see Fig.42) with longitudinally polarized electrons at 11 GeV. Multiple reactions of interest will be studied with the exclusive reaction:

$$\vec{e}p \rightarrow e'\mu^+\mu^-p'. \tag{32}$$

Physics observables in DDVCS, TCS, and J/ψ production include cross-sections and beam and angular asymmetries, measured in a wide range of the center-of-mass energies, $s \equiv \mathrm{W}^2 = (q+p)^2$, the squared four-momentum transfer $t = (p' - p)^2$, and the spacelike and timelike virtualities of incoming and outgoing photons, $\mathrm{Q}^2 = -q^2 = -(k-k')^2$ and $\mathrm{Q}'^2 \equiv \mathrm{M}^2_{\mu\mu} = (p_{\mu^+} + p_{\mu^-})^2$, respectively. Here $k(k')$ is the four-momentum vector of the incoming (scattered) electron, $p(p')$ is the four-vector of the target (recoil) proton, and p_{μ^+} and p_{μ^-} are the four-momentum vectors of the decay muons.

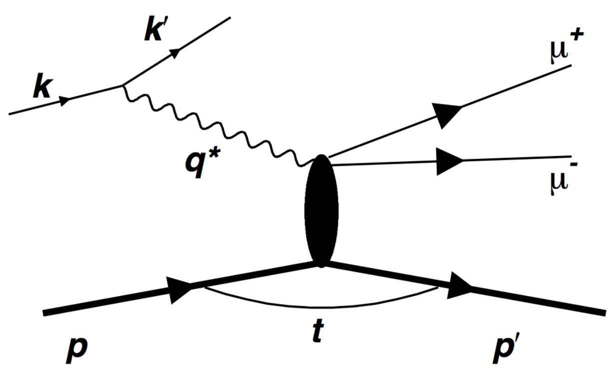

FIG. 42: Diagram of the muon pair electroproduction.

For DDVCS and J/ψ analyses, we plan to detect the scattered electron and the muon pairs from the timelike photon decay, where the recoil proton will be identified in the missing momentum analysis as:

$$\begin{aligned} &\vec{e}p \rightarrow e'\mu^+\mu^-X, \\ M_X^2 &= (k + p - k' - p_{\mu^+} - p_{\mu^-})^2 \approx M_p^2. \end{aligned} \tag{33}$$

The TCS studies use the reaction, where the missing scattered electron will be identified and its the kinematics will be deduced through missing momentum analysis, similar to the CLAS12 TCS analysis:

$$\begin{aligned} &\vec{e}p \to \mu^+\mu^- p' X, \\ &M_X^2 = (k + p - p' - p_{\mu^+} - p_{\mu^-})^2 \approx M_e^2, \\ &P_X^\perp \approx 0. \end{aligned} \tag{34}$$

Additionally, semi-exclusive ($e'\mu^{+(-)}p'$) and exclusive ($e'\mu^+\mu^-p'$) final state that will be analyzed to perform systematic checks.

A. DDVCS measurement

1. *Kinematic coverage*

Fig.43 illustrates the kinematic coverage of the experiment for electroproduction of di-muons in terms of W, Q^2, t, and $M(\mu^+\mu^-)$. The distributions are obtained with full Monte-Carlo simulation of Bethe-Heitler events, using the GRAPE event generator[116], processed through the GEANT4-based model of μCLAS12 and followed by particle reconstruction using the CLAS12 event reconstruction tool, COATJAVA[97]. The simulation assumes a proton target and an 11 GeV electron beam. The scattered electrons are reconstructed in the $PbWO_4$ calorimeter, with a detection threshold of $k'_0 > 0.5$ GeV in the angular range $8^\circ < \theta_{e'} < 30^\circ$. Muon kinematics is defined by the μCLAS12 Forward Detector (FD) acceptance, accounting for the energy loss in the calorimeter and the shield in front of it.

The accessible phase space in ξ and ξ' is shown in Fig.45. The μCLAS12 acceptance predominantly favors the time-like region largely due to the statistical limit at large $Q^2 \gg Q'^2_{min} \geq 1.4$ GeV^2. Nevertheless, expected statistics will allow us to explore DDVCS in the space-like region of $\xi' < 0.1$.

Figure 44 shows the coverage in transferred momentum t, demonstrating reasonably good coverage in the relevant region of $-t < 1$ GeV^2 for both space-like and time-like DDVCS measurements. We expect to collect more than 0.5 M events for the DDVCS analysis.

2. *Observables to be measured*

The primary goal for DDVCS studies is to measure Beam Spin Asymmetries (A_{LU}) as a function of the angle between leptonic and hadronic planes, ϕ_L, in a wide range of skewness (ξ) and the generalized Bjorken variable (ξ'). The A_{LU}, defined as:

$$A_{LU} = \frac{1}{P_b}\frac{N^+ - N^-}{N^+ + N^-}, \tag{35}$$

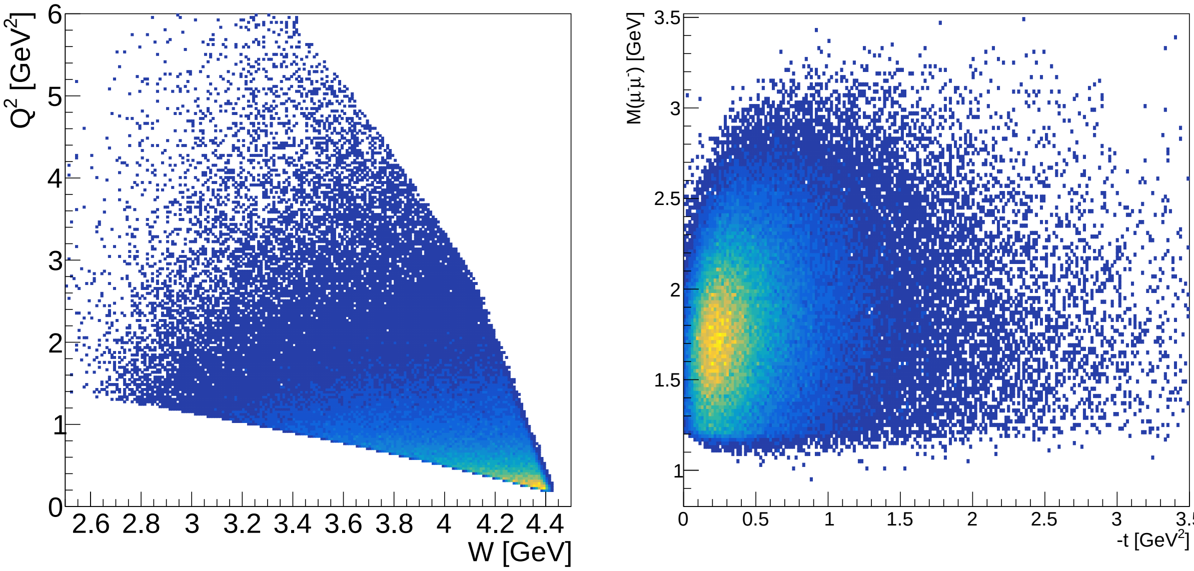

FIG. 43: Kinematic coverage of μCLAS12 for di-muon electroproduction with an 11 GeV electron beam. Left: Q^2 vs. $W = \sqrt{s}$ distribution, where limits are defined by detecting the scattered electron in the μCLAS12 $\mathrm{PbWO_4}$ calorimeter. Right: Distribution of the invariant mass of lepton pairs detected in the μCLAS12 forward detector as a function of squared momentum transferred.

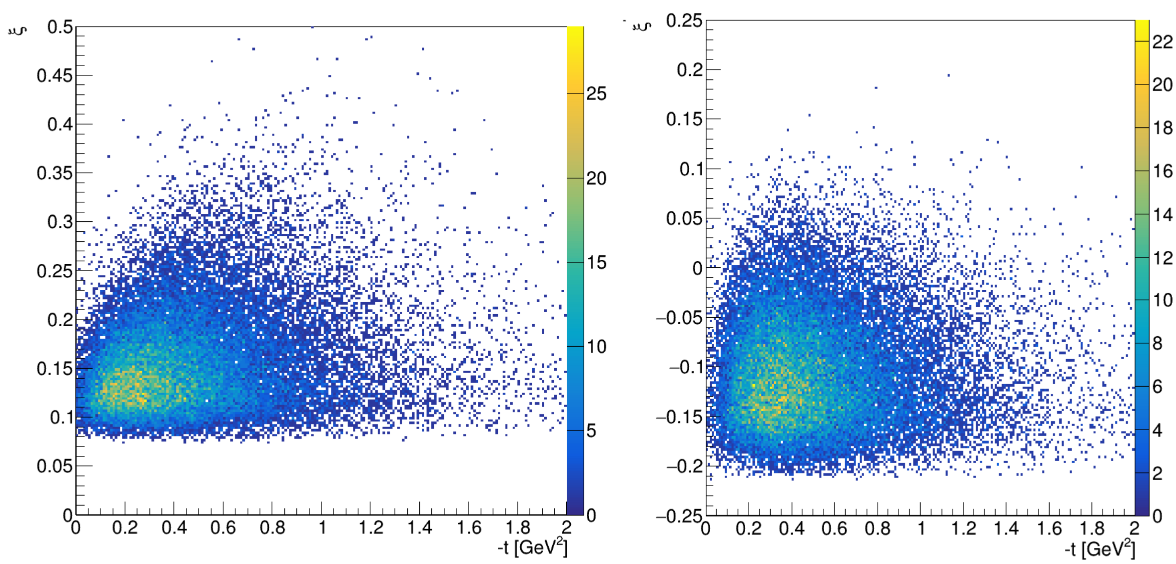

FIG. 44: Coverage in transferred momentum squared t for the DDVCS measurements in the time-like region. Left: ξ vs. $-t$ for $-0.1 < \xi' < -0.06$. Right: ξ' vs. $-t$ for $0.17 < \xi < 0.23$.

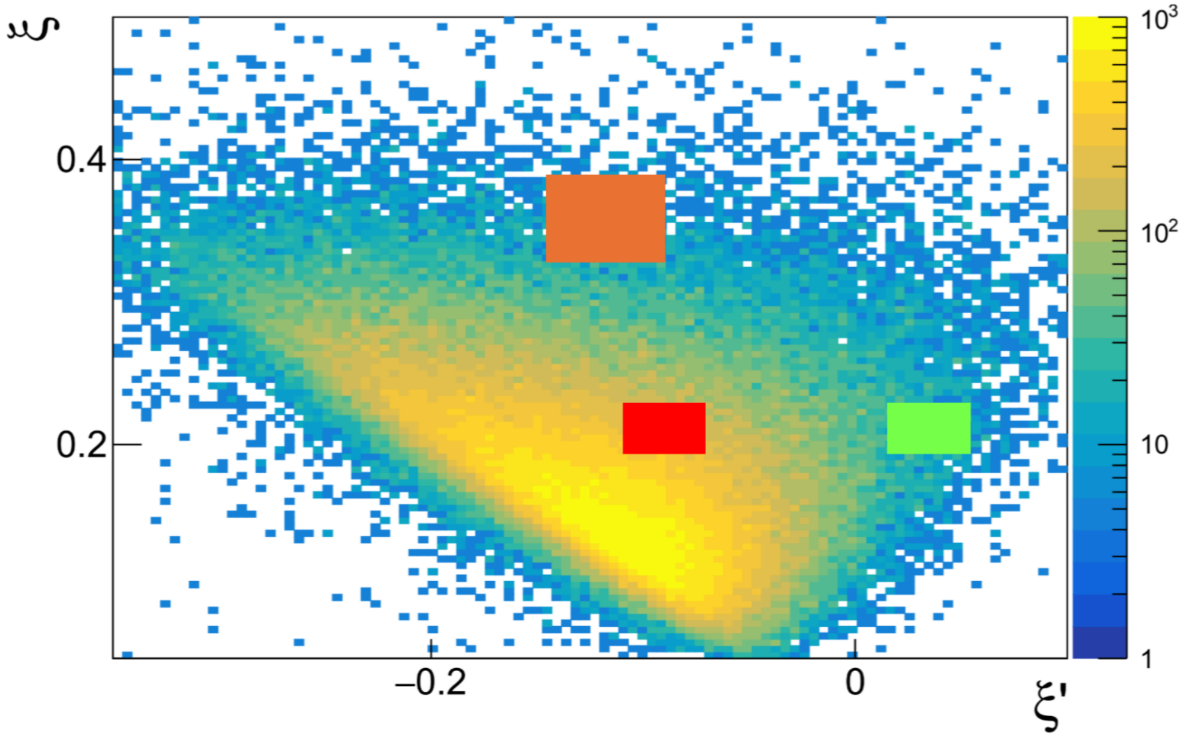

FIG. 45: ξ vs. ξ' distribution for reconstructed DDVCS+BH events. The boxes represent kinematic bins used to illustrate expected beam spin asymmetries in the time-like, $Q'^2 > Q^2$, and space-like, $Q'^2 < Q^2$, regions.

where N^- and N^+ are the number of events with positive and negative beam helicities, respectively, and P_b is the beam polarization as measured with Hall B Möller polarimeter. The asymmetry will be measured in multiple bins, covering both the space-like ($Q'^2 < Q^2$) and time-like ($Q'^2 > Q^2$) regions. A key objective is to observe the sign change of the asymmetry during the transition between these regions.

Figure 45 shows the kinematic coverage in (ξ', ξ) after 200 days of beam running with μCLAS12, utilizing a liquid hydrogen target and an 11 GeV electron beam. The boxes drawn on the plot represent kinematic bins we used to illustrate expected results on A_{LU} in 200 days of beam running with μCLAS12 using a liquid hydrogen target and a 11 GeV electron. For each (ξ', ξ) bin, shown as red and green boxes in Fig.45, the asymmetry A_{LU} was extracted from simulated data for two different average values of Q'^2 and Q^2 points as depicted in the left panel of Fig.46. The right panel of the figure displays the corresponding kinematics of the scattered electron.

The obtained A_{LU} values, along with the expected statistical uncertainties for four kinematic bins (as indicated in Figs.45 and 46 with color coding), are shown in Fig.47. The beam spin

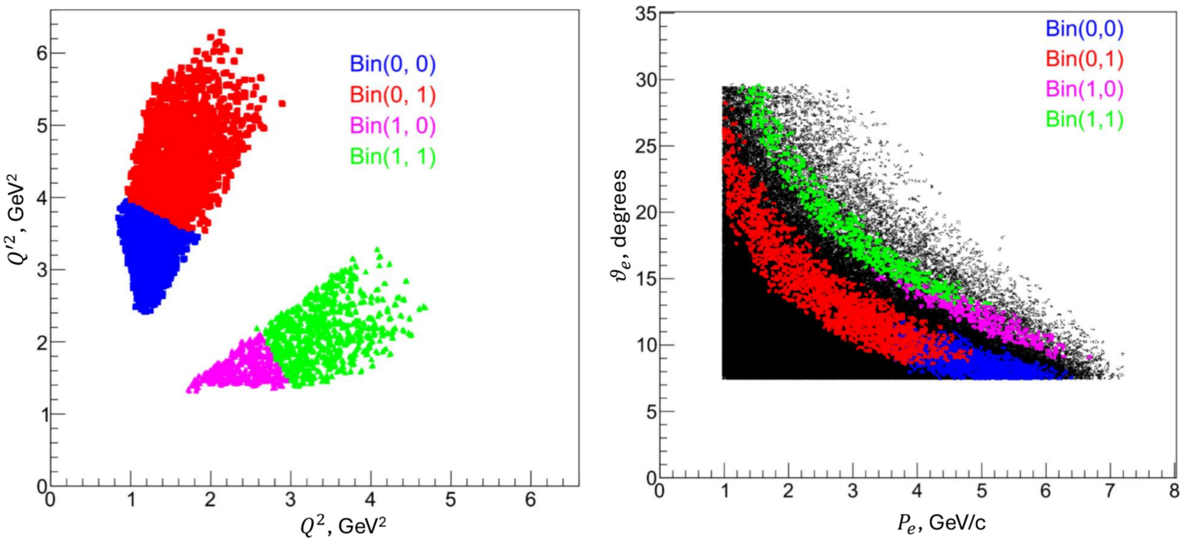

FIG. 46: The Q'^2 vs. Q^2 distribution of events for red and green (ξ, ξ') bins in Fig.45. For each (ξ, ξ') bin, the A_{LU} is studied in two different average $\bar{Q}'^2$ and $\bar{Q}^2$ points.

asymmetry for DDVCS was generated using the VGG model [117]. In the space-like region, the statistical uncertainties of A_{LU} are larger than those in the time-like region. Nonetheless, the expected uncertainties are sufficient to accurately extract the $\sin\phi_L$ moment, $A_{LU}^{\sin\phi}$, with sufficient accuracy, as indicated in the plots.

3. Beam Spin Asymmetry and shadow GPD

As discussed in the motivation, observables in DVCS and TCS can only access two of the three variables that define GPDs. The variable x effectively drops out in CFFs for these processes, leading to non-unique solutions when reconstructing GPDs from experimental data. Consequently, a large number of functions, so-called shadow GPDs (SGPDs), added to the regular GPDs will explain the experimental data, complicating the interpretation. In contrast, DDVCS observables retain sensitivity to the variable x, allowing all three GPD parameters to vary independently. This makes mapping GPDs in three dimensions possible, providing a more comprehensive and precise understanding of the nucleon structure.

Figure 48 shows an example of the proposed A_{LU} measurement, where it is possible to distinguish between asymmetries generated using GPD parametrization in the Goloskokov-Kroll model (GK19) from *PARTONS* [21] and asymmetries generated with the same model incorporating an additional NLO SGPD. This demonstrates the potential of DDVCS to resolve ambiguities arising

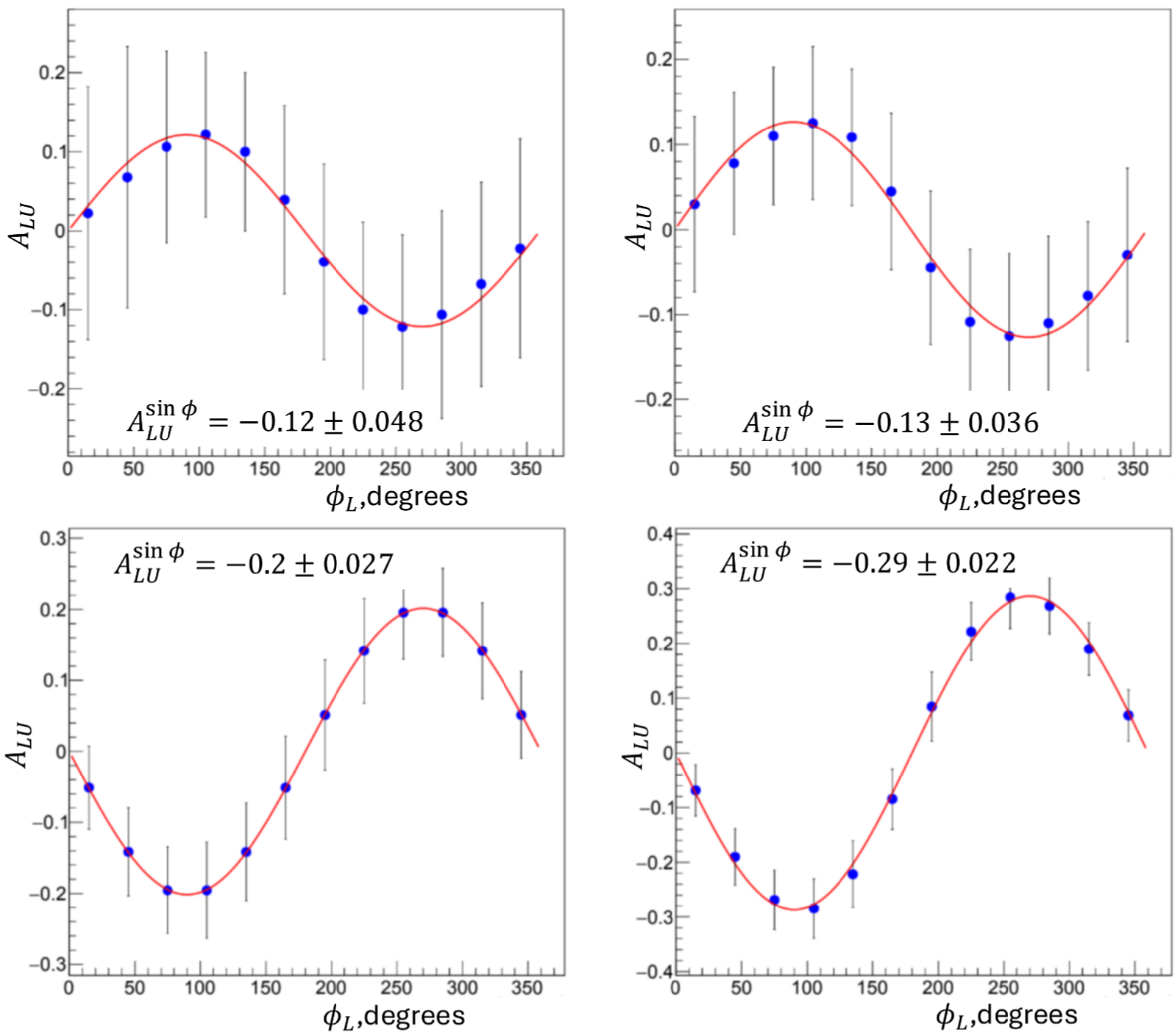

FIG. 47: The top two plots show expected beam spin asymmetry in the space-like region for two kinematic points: on the left - $\bar{Q}^2 = 2.4$ GeV^2, $\bar{Q}'^2 = 1.64$ GeV^2, $\bar{x}_B = 0.21$, and $-\bar{t} = 0.33$ GeV^2; on the right - $\bar{Q}^2 = 3.38$ GeV^2, $\bar{Q}'^2 = 2.14$ GeV^2, $\bar{x}_B = 0.21$, and $-\bar{t} = 0.34$ GeV^2. The bottom two plots are A_{LU}s for two bins in the time-like region: on the left - $\bar{Q}^2 = 1.24$ GeV^2, $\bar{Q}'^2 = 3.3$ GeV^2, $\bar{x}_B = 0.11$, and $-\bar{t} = 0.33$ GeV^2; on the right - $\bar{Q}^2 = 1.63$ GeV^2, $\bar{Q}'^2 = 4.55$ GeV^2, $\bar{x}_B = 0.1$, and $-\bar{t} = 0.34$ GeV^2.

from SGPD contributions, aiding accurate GPD extraction.

However, our measurements alone will not fully resolve the problem of SGPDs. The separation of SGPD contributions will not be possible in every bin of the accessible phase space and may not be feasible for all classes of SGPDs, as illustrated in Fig.8. Nevertheless, the measurements will significantly reduce the number of possible SGPDs and enable more reliable modeling of regular GPDs.

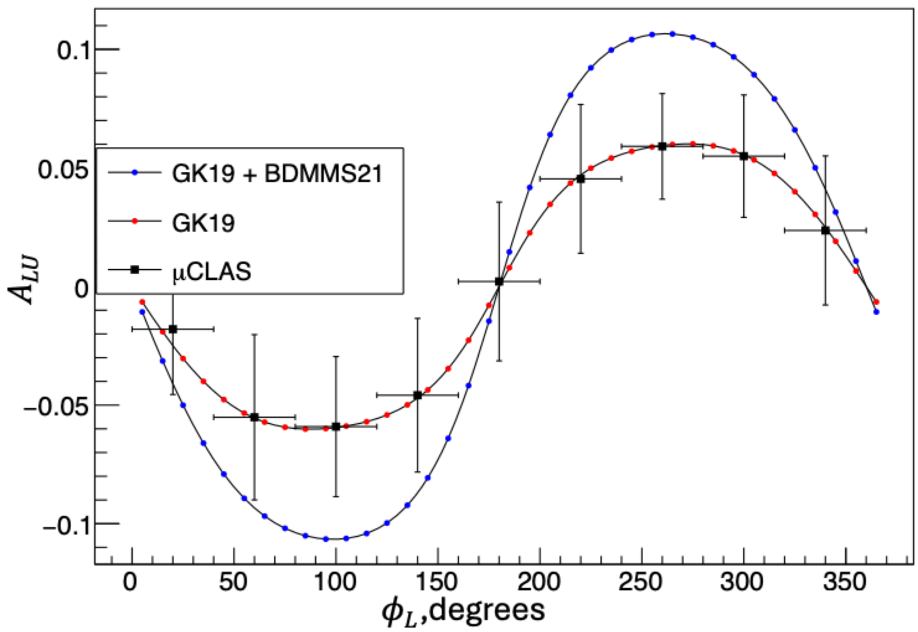

FIG. 48: A comparison of the expected A_{LU} generated with GPD parametrization from the Goloskokov-Kroll model, GK19 from *PARTONS*, and with asymmetry predicted with the addition of an NLO shadow GPD (module GPDBDMMS21 in [118]). The kinematics of the bin is $\bar{\xi} = 0.36$, $\bar{\xi}' = -0.0820637$, and $-\bar{t} = 0.82$ GeV^2.

B. Electro-production of J/ψ near the production threshold

1. Overview

The exclusive production of vector mesons has long been identified as one of the primary ways to access the gluon content of the nucleon. Measurements performed in recent years at JLab [28–30] have provided the very first cross-section results on the photoproduction of J/ψ near its production threshold. Since then, these results have led to extensive theoretical interpretations. In the following, we demonstrate that the experimental setup presented in this document is capable of measuring the electroproduction of J/ψ with a pair of muons in the final state.

The expected statistics for the total proposed integrated luminosity will be up to 20 times larger than the statistics accumulated by any of the J/ψ experiments at JLab. Additionally, this measurement will provide data for large initial photon virtuality up to 1 GeV^2, providing another leverage to understand the gluon content of the proton.

2. Kinematic coverage and yield estimation

For this proposal, we used the model developed in [119], and implemented in the the *elSpectro* event generator [120], to simulate J/ψ events produced with a 10.6 GeV beam (the typical beam energy delivered to CLAS12). Additionally, Monte-Carlo samples describing the various backgrounds of these measurements were produced, particularly to describe the mass continuum at lower invariant mass. The generated events were passed through the μGEMC simulation framework, and events with two detected muons and a generated electron within the geometrical acceptance of the wECal (polar angle in the $8°$ to $30°$ range) were kept for the rest of the analysis. The energy of the electron is smeared by a resolution factor $4\%/\sqrt{E}$, which mimics the expected performances of the wECal. Finally, the momentum of the electron is required to be above 0.5 GeV, which is the estimated threshold above which the pion and electron will be distinguishable in the new wECal.

Fig.49 shows the kinematic reach of the μCLAS12 setup for the selected J/ψ events. In particular, a large range of t, from 0.5 GeV^2 to 5 GeV^2, is accessible as we do not need to detect the scattered proton. This will allow us to measure the t-dependence of the cross-section, which is a key element in understanding the gluons distribution in the proton. The range of initial photon virtuality will go from approximately 0.1 GeV to almost 2 GeV. This allows us to explore the dependence of gluon content of the proton with respect to Bjorken x. Finally, the hadronic mass W range will extend up to 4.45 GeV, allowing the electro-production of pentaquarks to be probed (see next section).

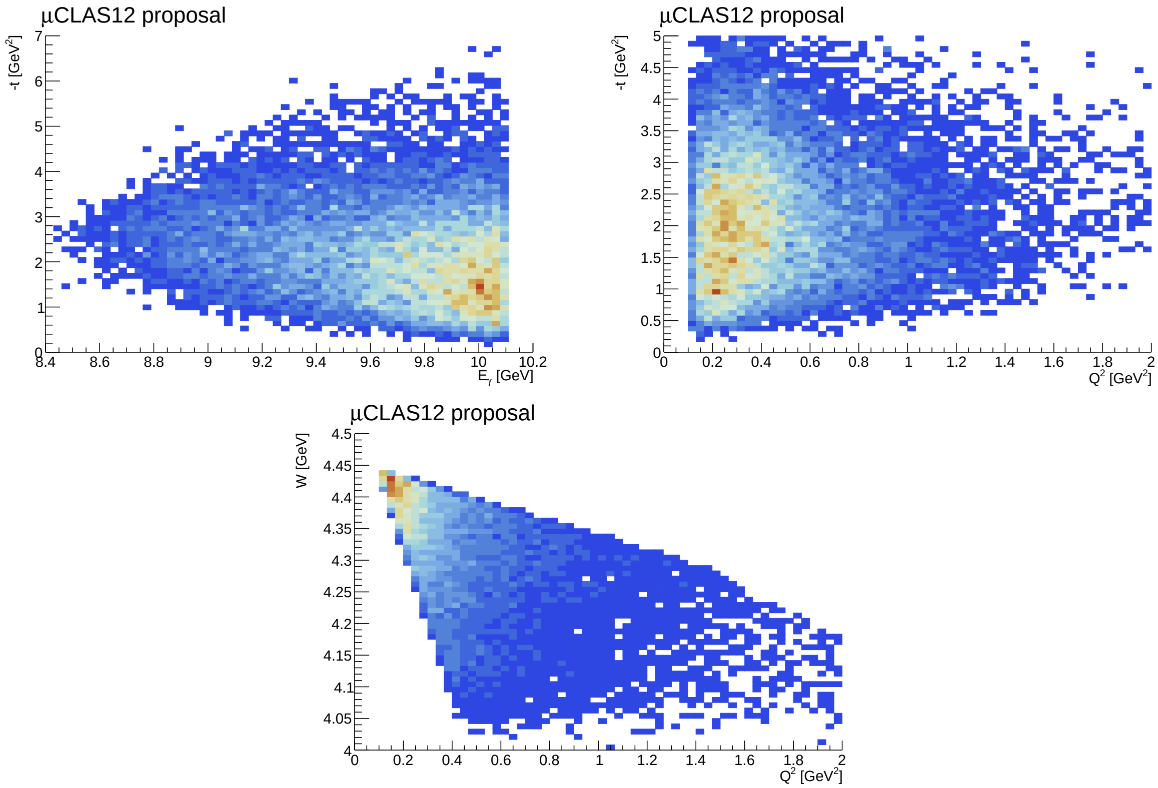

FIG. 49: Kinematics of J/ψ electroproduction with 10.6 GeV beam. Top left: $-t$ vs E_γ, top right: $-t$ vs Q^2, bottom: W vs Q^2. All distributions are produced using J/ψ events with final state particles in the acceptance of the proposed experimental setup.

The proposed experiment will run for 200 days with a luminosity of $10^{37}\mathrm{s}^{-1}\mathrm{cm}^{-2}$. We estimated that in these conditions, the total expected J/ψ yield will be of the order of 45k. This projection assumes an electron detection efficiency in the calorimeter fiducial volume close to 100%. With a realistic identification efficiency of 90%, the expected yield is still above 40k, which is 20 times larger than the statistics published by GlueX and the Hall C-007 experiments, respectively. Furthermore, the backgrounds under the J/ψ peak have also been estimated. The contributions from the elastic and inelastic Bethe-Heilter process and coincidence background have been evaluated. As seen in Fig.50, the J/ψ peak is well visible above the background. Although it was not used in this projection, an additional leverage to lower the background is the use of the missing mass of the system peaking at the mass of the proton. As shown on the right panel of Fig.50, one could apply a cut on the missing proton mass to reduce both inelastic and accidental backgrounds. Figures 51 and 52 show the distributions in t, Q^2, and W of all events with an invariant mass above 2.2

GeV. In particular, the t-coverage is clearly visible, with consequent statistics at high-t above 2 GeV, where current experiments have accumulated only a small amount of data. The coverage in W extends up to 4.45 GeV. This limit is mainly given by the beam energy and the minimum momentum for the detected electron. In section IV C, we demonstrate that the proposed setup is sufficient to study the production of pentaquarks above W=4.4 GeV.

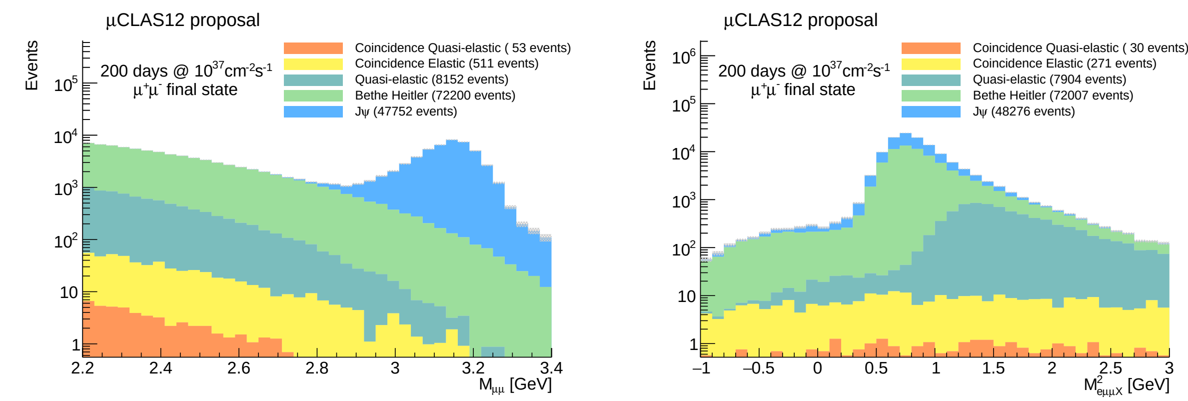

FIG. 50: Left: Invariant mass of reconstructed muons pairs in the J/ψ mass region. The expected J/ψ yield is about 45k events.

Right: Missing mass of the undetected proton in the 2.2 to 3.4 GeV invariant mass region. The width of the distribution is mostly dominated by the muons' momentum resolution.

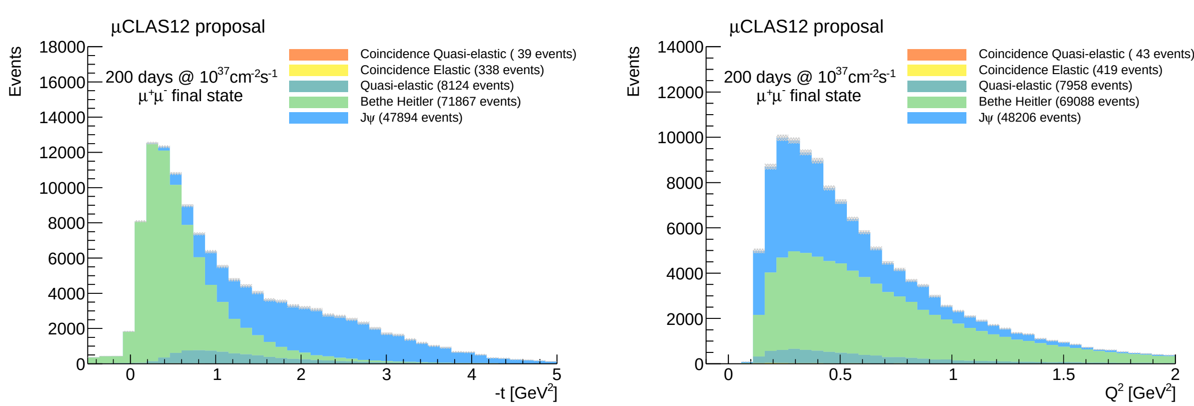

FIG. 51: Left: Square of the transferred momentum to the proton t of events in the 2.2 to 3.4 GeV invariant mass region.

Right: Virtuality of the photon Q^2 in the 2.2 to 3.4 GeV invariant mass region. The μCLAS12 acceptance for electrons allows to cover a range of virtuality from 0.1 to 1 GeV^2.

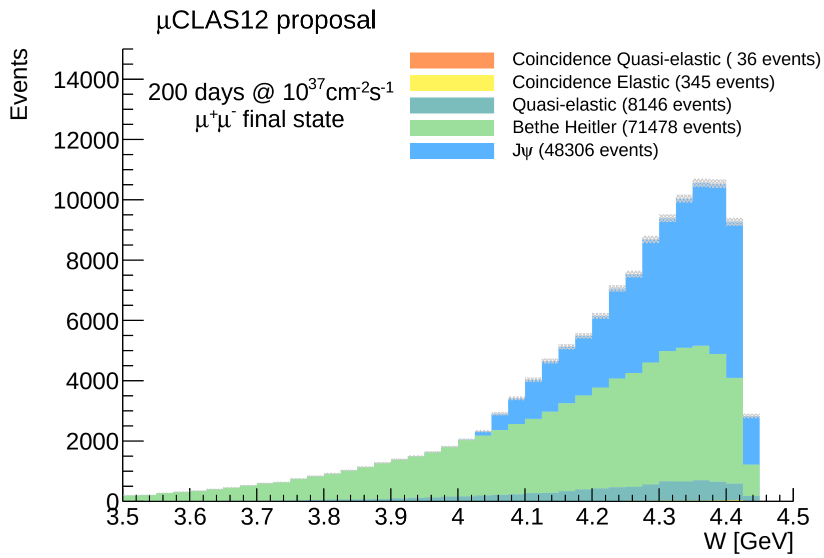

FIG. 52: Hadronic mass W in the 2.2 to 3.4 GeV invariant mass region and in the μCLAS12 acceptance. The experimental setup presented in this proposal allows to study the electro-production of $J/\psi$from its threshold production and potentially investigate the production of charmed pentaquarks of mass below 4.45 GeV. This last point is described in detail in the following section.

3. Observables to be measured

The deliverables of this measurement are the following:

- Cross section of J/ψ electro-production as a function of the photon energy (or equivalently W) in bins of photon virtuality.

  The experiment E12-12-001 has measured the W-dependence near the threshold at $\mathrm{Q}^2 = 0$ GeV^2 using data taken by CLAS12 during the 2018 and 2019 run period. The total number of J/ψ collected for this analysis is 700, and the results obtained for this measurement are shown in Fig.17. With the suggested measurement, we can perform a similar extraction with much larger statistics as seen in Fig.53. This measurement will also cover the energy range where open charm contributions are expected to be the largest (from 8.7 to 9.4 GeV). Finally, we will be able to study the Q^2 dependence of the cross-section, up to 1.5 GeV^2.

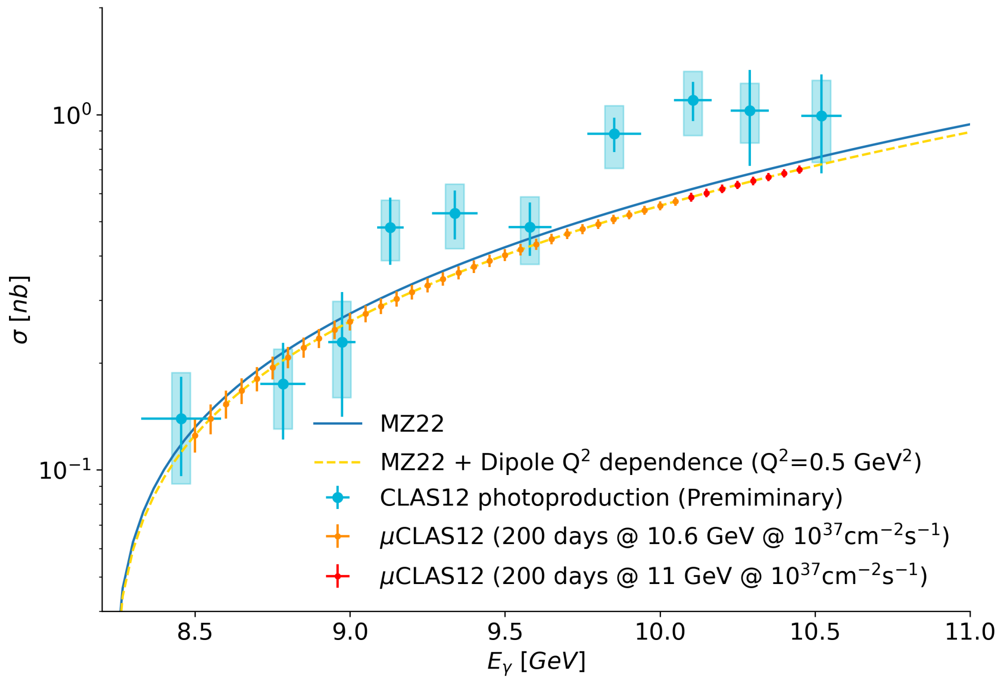

FIG. 53: Error bars projection for extracting the cross-section as a function of the photon energy. The orange points represent the statistical error, which can be achieved with the proposed beam time luminosity at a beam energy of 10.6 GeV. The red points show the statistical error expected in the additional phase space covered if the experiment runs with an 11 GeV beam. The maximum energy is determined by the minimum momentum of the electron, which can be reconstructed in the new calorimeter. The model used for the prediction is from [68]. These error bars are compared to the preliminary ones obtained using data taken by CLAS12 in 2018 and 2019.

- The t-dependence of the differential cross section, $d\sigma/dt$

  The E12-12-001 data presented in 17 have also been used to extract the t-dependence of the cross-section at $Q^2 = 0$ GeV^2. With μCLAS12, we will be able to perform a similar extraction with improved error bars and extended t coverage. Extracting the t-dependence of the cross-section is critical in understanding the gluon distribution in the proton and is closely related to the mass radius of the proton. Figure 54 shows the expected error bars of this measurement. As for the cross-section extraction as a function of E_γ, we tested two scenarios: a 10.6 GeV and an 11 GeV electron beam. The obtained errors are compared with the preliminary ones obtained using the CLAS12 E12-12-001 data, demonstrating the relevance of the measurement.

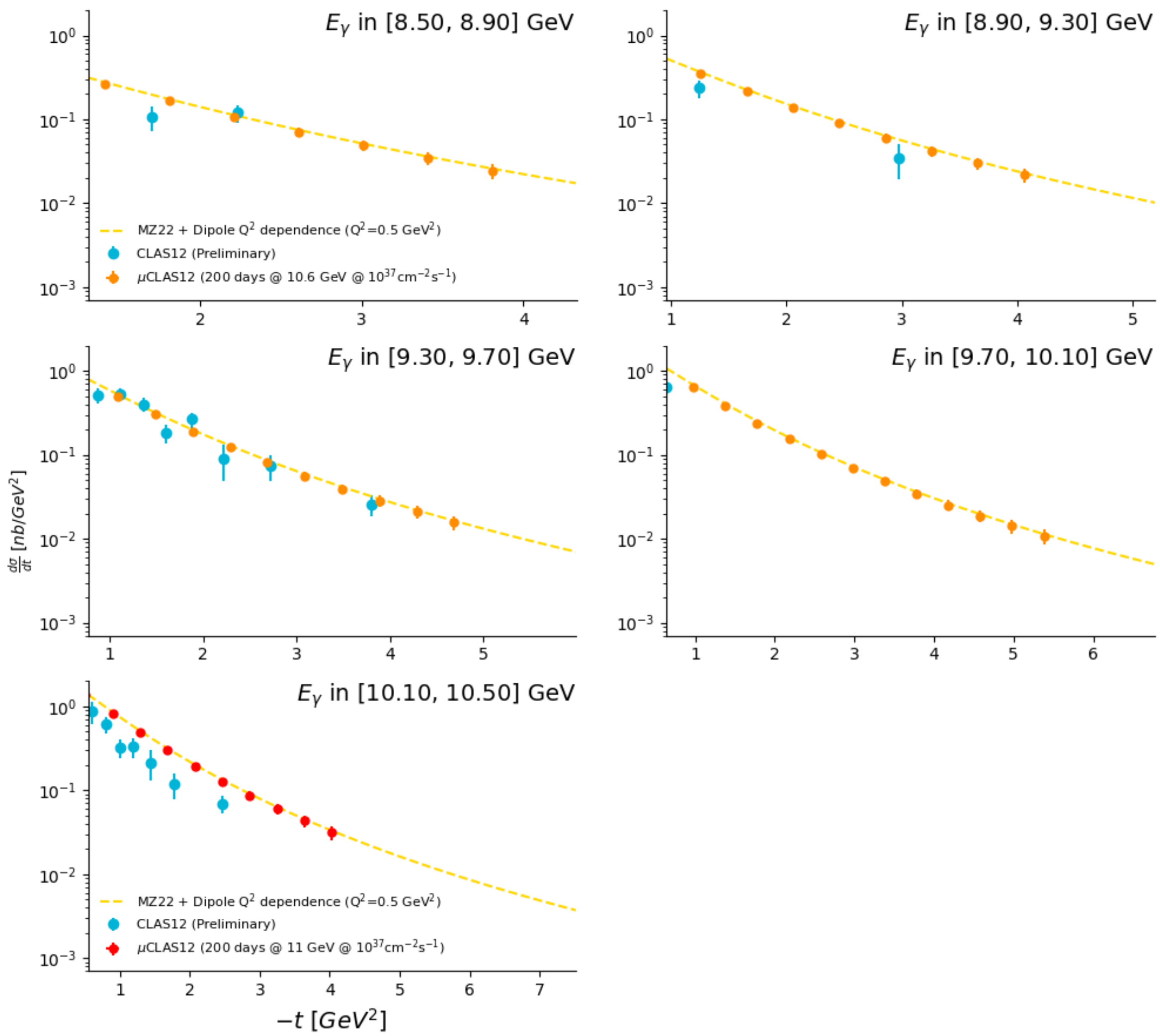

FIG. 54: Error bars projection for extracting the cross-section as a function of t. The orange points represent the statistical error, which can be achieved with the proposed beam time luminosity at a beam energy of 10.6 GeV. The red points show the statistical error expected in the additional phase space covered if the experiment runs with an 11 GeV beam. The model used for the prediction is from [68]. These error bars are compared to the preliminary ones obtained using data taken by CLAS12 in 2018 and 2019.

From the t and E_γ dependence of the cross-section, it is possible to extract the gluons GFFs, the mass and scalar radius, and the pressure profiles in the proton, as described in section II E 3. We plan to extract all these quantities, and given the error bars shown in Fig.54, we expect our measurement to have a great impact on this extraction. To illustrate this statement, we extracted the mass radius of the proton using a simpler dipole model, as introduced in [67]. In this model, the t-dependence of the cross-section is fitted as:

$$\frac{d\sigma}{dt} = \left.\frac{d\sigma}{dt}\right|_0 \cdot \frac{1}{(1 - t/m_S^2)^4}, \tag{36}$$

and the m_S parameter can be related to the mass radius of the proton as:

$$\sqrt{\langle r_m^2 \rangle} = \frac{\sqrt{12}}{ms}. \tag{37}$$

The dipole parameter is extracted as a function of photon energy, and the projected errors on these measurements are shown in Fig.55. As stated previously, the J/ψ data collected by μCLAS12 will allow us to probe the gluon content of the proton with the best accuracy to date.

- Decay angular distributions and ratio $R = \sigma_L/\sigma_T$

The angular distributions of muons in the J/ψ rest frame provide information about the photon and J/ψ polarization states. Under the assumption of SCHC [121], the normalized angular distribution can be expressed in the form

$$\frac{1}{N}\frac{dN}{d\cos\theta_h} = \frac{3}{8}\left[1 + r_{00}^{04} + (1 - 3r_{00}^{04})\cos^2\theta_h\right], \tag{38}$$

$$\frac{1}{N}\frac{dN}{d\psi_h} = \frac{1}{2\pi}\left[1 - \epsilon r_{1-1}^{1}\cos 2\psi_h\right]. \tag{39}$$

Assuming SCHC and natural spin-parity exchange (NPE) [121], the matrix elements r_{00}^{04} and r_{1-1}^{1} are related by

$$r_{1-1}^{1} = \frac{1}{2}\left(1 - r_{00}^{04}\right), \tag{40}$$

and the ratio of the longitudinal to transverse cross section, $R = \sigma_L/\sigma_T$, is related to r_{00}^{04} as:

$$R = \frac{1}{\epsilon}\frac{r_{00}^{04}}{1 - r_{00}^{04}}. \tag{41}$$

μCLAS12 will allow to measure the production of J/ψ up to Q^2=1.5 GeV^2. Thus, we propose to study the ratio R as a function of Q^2.

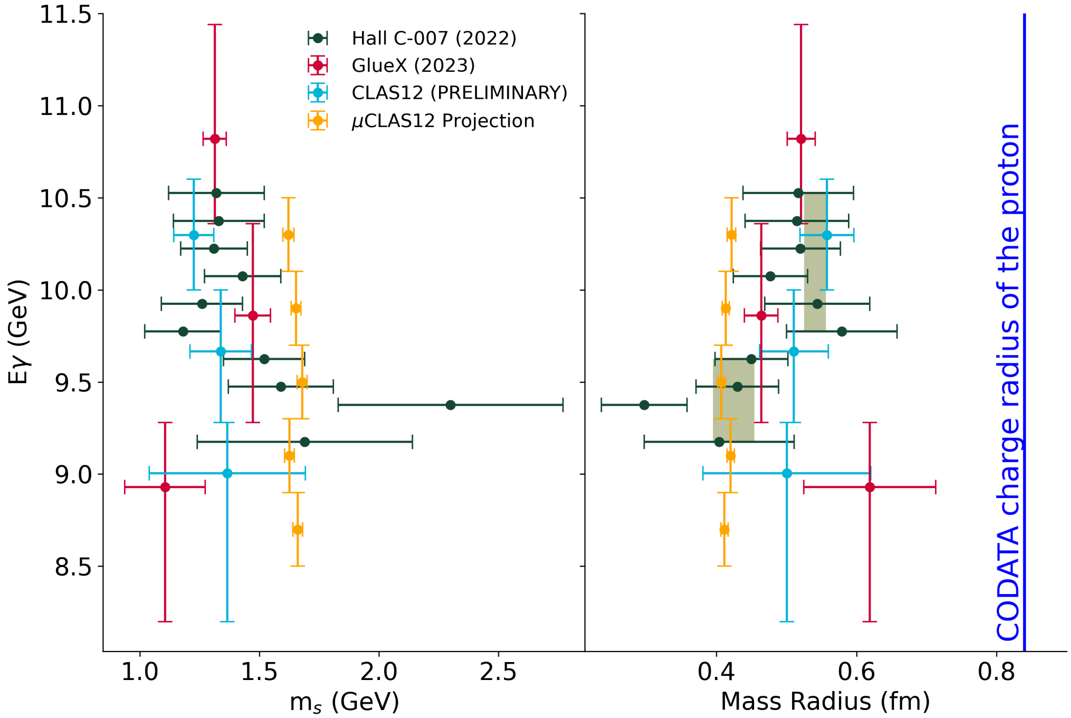

FIG. 55: Error bars projection for extracting the mass radius of the proton as a function of the real photon energy, following the model in [67]. The orange points represent the statistical error, which can be achieved with the proposed beam time luminosity at a beam energy of 10.6 GeV (the highest energy bin is accessible with an 11 GeV beam). These projections are compared with extractions performed using HallC-007, GlueX, and preliminary CLAS12 data. For readability, the projected radius values have been shifted to the left of the figure.

C. Search for LHCb pentaquarks

1. Overview

The LHCb collaboration published the discovery of three exotic structures in the $J/\psi + p$ decay channel, which have been referred to as charmonium-pentaquark states [122]. They labeled these states as $P_c(4312)$, $P_c(4440)$, and $P_c(4457)$. The minimum quark content of these states is $c\bar{c}uud$. The pentaquarks were observed in the decay $\Lambda_b^0 \to K^- P_c^+$, $P_c^+ \to J/\psi p$.

Since these states were observed in the decay mode $J/\psi + p$, it is natural to expect that they can be produced in the photoproduction process $\gamma^* + p \to P_c \to J/\psi + p$, where these states will appear as s-channel resonances at photon energy around 10 GeV [91, 119, 123, 124].

With the setup detailed in this proposal, we will search directly for these pentaquarks in the W spectrum of events tagged with a J/ψ. The pentaquarks manifest themselves as peaks in the spectrum at their respective mass. To assess whether the proposed setup will produce enough statistics and that the electron momentum resolution will allow to distinguish the peaks, we performed extensive simulation with the *elSpectro* event generator [120], which implements the pentaquark model of [119], with a 2% branching ratio. Two electron beam energy scenarios have been tested: 10.6 GeV or 11 GeV beam on target.

In the left panel of Fig.56, the W spectrum obtained in the 10.6 GeV electron beam configuration is shown for events where a J/ψ has been identified. The $P_c(4312)$ is visible, as the electron momentum resolution in wECal is sufficient not to smear the peak. It is estimated that about 2k $P_c(4312)$ will be produced over the 200 days of the experiment.

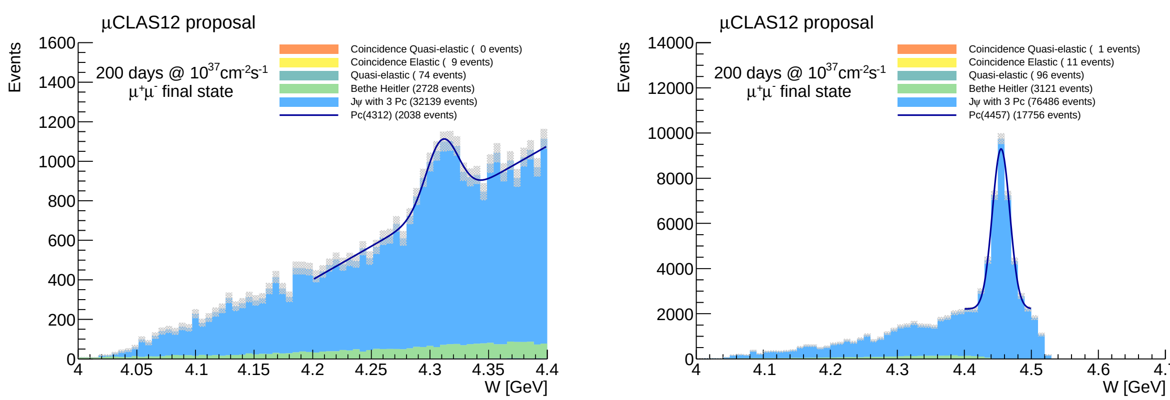

FIG. 56: Left: Hadronic mass W in the μCLAS12 acceptance, below 4.4 GeV. The invariant mass of the muon pair is restricted in the 2.7 to 3.2 GeV range. With the proposed integrated luminosity according to the model in [119], we expect to produce approximately 2000 $P_c(4312)$. Right: With the proposed integrated luminosity and an 11 GeV electron beam, we expect to produce approximately 18000 $P_c(4457)$, 90 per day.

In the right panel of Fig.56, the W spectrum obtained with an 11 GeV electron beam configuration is shown for events where a J/ψ has been identified. In this case, the additional energy provided by the beam allows us to reach the mass of the $P_c(4440)$ and $P_c(4457)$, which are expected to have a larger cross-section. We expect to produce around 18k $P_c(4440-4457)$ in this configuration. Note that the expected resolution of the wECal does not allow us to distinguish between the two contributions. The $P_c(4312)$ is also produced at this beam energy, with the same yield as for the 10.6 GeV beam configuration.

3. *Observables to be measured*

The resolution in W and the expected event rate of the proposed experiment will be sufficient to see pentaquark states if they exist, with both 10.6 or 11 GeV beam-on-target configurations. However, an 11 GeV electron beam is preferable to detect the $P_c(4457)$ which is expected to have a larger production rate. We plan to measure the pentaquarks production cross-section (or an upper limit of it).

D. Importance of the J/ψ measurement to understand DDVCS data

Since the final states for DDVCS and J/ψ are identical, the detector efficiency and resolution for exclusive J/ψ production is very similar to that of DDVCS events in the proposed range of lepton invariant mass. The narrow peak of the J/ψ will make identifying the reaction easier and more suitable for a reliable yield extraction than the DDVCS-BH continuum. The J/ψ electroproduction reaction can thus serve as an important benchmark, allowing us to better understand the systematic uncertainties. The $\phi(1020)$ could, in principle, also be used in a similar way at the lower end of the invariant mass range.

A measurement of the J/ψ cross section in parallel with DDVCS will thus be very beneficial for understanding the DDVCS data and help addressing the two main sources of systematic uncertainty, such as acceptance and muon identification.

E. Timelike Compton Scattering measurement

1. *Overview*

The Timelike Compton Scattering reaction will be measured in the quasi-real photoproduction regime, where the beam electron radiates a quasi-real photon as in:

$$ep \to (e')p'\mu^+\mu^-. \tag{42}$$

The reaction will be identified by requiring a pair of muons in the Forward CLAS12 detector and a proton in the recoil detector. It is then possible to reconstruct the kinematic of the undetected scattered electron. To select the quasi-real events, the missing mass of the undetected scattered electron and the virtuality of the initial photon can be constrained to be small. This analysis strategy has been used in the first ever TCS measurement using CLAS12 data in [19].

With the proposed experiment, we aim to measure the beam spin asymmetries (BSA) and the Forward-Backward asymmetry of TCS, in a wide range of E_γ, t, and Q'^2, and with a very large collected statistics compared to the published CLAS12 results.

2. *Kinematic coverage and yield estimation*

To estimate the kinematic coverage and the rates of the TCS measurement in the proposed experimental setup, a sample of 10M Bethe-Heitler events has been run in the GEANT4 simulation of the experiment. Events with two identified muons in the forward detector are selected, and the kinematics of the generated recoil proton is restricted to the active area of the planned recoil detector. Figure 57 shows the polar angle of the proton as a function of the invariant mass of the muon pair. In the case of the TCS measurement, an invariant mass above 1.5 GeV is selected to ensure the GPD formalism applies. In the current CLAS12 configuration, the central detector can detect protons above 0.35 GeV. Considering that the proposed recoil tracker will have a similar geometry, we required a minimum momentum of 0.35 GeV for protons. Figure 57 shows the generated proton's angle and momenta and the phase space the recoil detector will cover. The total accumulated statistics for 200 days with a luminosity of $10^{37}\mathrm{s}^{-1}\mathrm{cm}^{-2}$ is estimated to be 7.7 M events. Thus, this measurement will have a three-order-of-magnitude increase in statistics with respect to the first CLAS12 TCS publication.

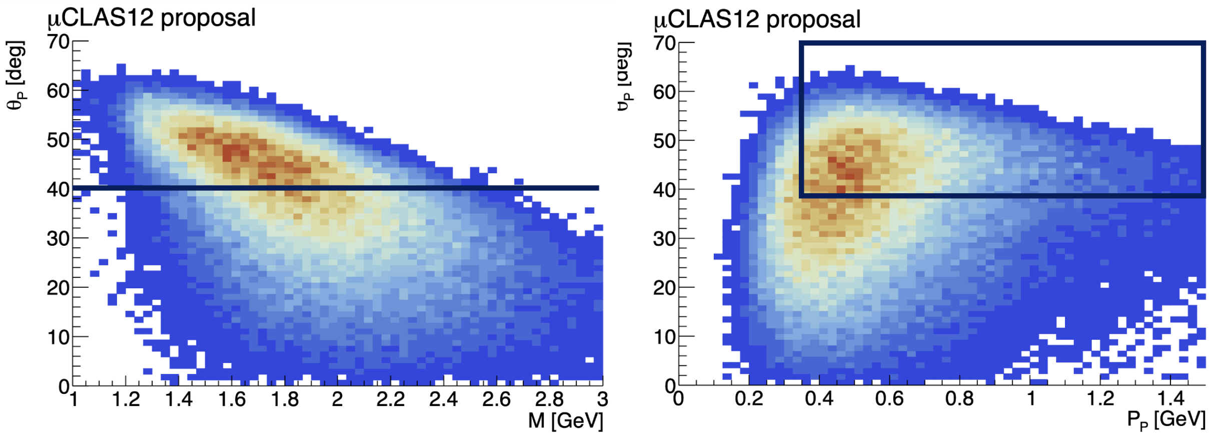

FIG. 57: Left: Proton polar angle as a function of the invariant mass of the muon pair. Right: Polar angle as a function of momentum for the proton. Events displayed are required to have a muon pair detected in μCLAS12. The black line shows the acceptance limit of the recoil detector. Events within this region are used to estimate the measurement yield.

Figure 58 shows the Mandelstam t as a function of the invariant mass for events with a proton in the acceptance limit of the recoil tracker. With the proposed setup, we will be able to access a wide range of invariant masses, up to 2.3 GeV, with a large coverage of t, especially in the region below 0.4 GeV^2, where measurement will be most relevant for the extraction of GPDs.

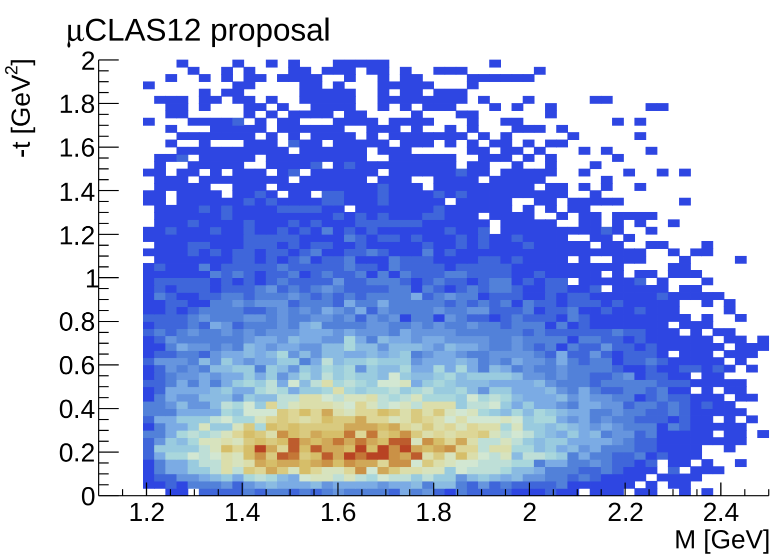

FIG. 58: Mandelstam t as a function of the invariant mass of the muon pair, for proton within the acceptance of the recoil detector.

We also plan to develop a proton identification algorithm based on Boosted Decision Trees, which would use information provided by the new calorimeter. Such algorithms have already been developed for electron and muon pairs in the current CLAS12 calorimeters. This would allow us to extend the proton detection range below 30° and thus reach a larger invariant mass up to 2.8 GeV.

3. Observables to be measured

- Beam spin asymmetry:

  In the case of the BSA, the experimental asymmetry reads:

$$BSA = \frac{1}{P_b}\frac{N^+ - N^-}{N^+ + N^-}, \tag{43}$$

  where P_b is the average polarization of the beam, and N^+ and N^- are respectively the right-handed and left-handed transverse polarization of the initial real photon. The polarization of the real photon will be estimated using the polarization of the initial beam electron and the well-known polarization transfer given by QED [125].

  As the phase space covered by this experiment is similar to the one covered by CLAS12, we expect to be able to cross-check our results with those published by CLAS12.

- Forward/Backward asymmetry:

  For the TCS measurement using CLAS12 data [19], it was shown that the Forward-Backward asymmetry (A_{FB}, exchange of decay leptons momenta) of TCS allows direct access to the real part of the CFF $\mathcal{H}$. Similarly, we can measure the TCS A_{FB} using μCLAS12.

  The Forward-Backward asymmetry is given by:

$$A_{FB} = \frac{N_F - N_B}{N_F + N_B}, \tag{44}$$

  where N_F and N_B are the number of events in the forward and backward bins, respectively. The angular range of these two bins is related as $\phi_B = 180^\circ + \phi_F$ and $\theta_B = 180^\circ - \theta_F$. As the angular acceptance of μCLAS12 is the same as the one of CLAS12, we will be able to measure this asymmetry in the same bin as CLAS12 ($-40^\circ < \phi_F < 40^\circ$, $50^\circ < \theta_F < 80^\circ$), with a much improved precision.

  As for the BSA, we will be able to cross-check our results with the one published by CLAS12, as the phase spaces mostly overlap.

- Cross-section:

  Finally, considering the large amount of data that this experiment will collect for this reaction, the extraction of the total and polarized cross-section will be done.

V. SUMMARY AND BEAM TIME REQUEST

We propose to study Double Deeply Virtual Compton Scattering (DDVCS) and J/ψ electroproduction on the proton using an 11 GeV electron beam and the modified CLAS12 detector in Experimental Hall B at Jefferson Lab. The proposed modifications to the CLAS12 detector serve two primary purposes: (a) to enable the CLAS12 Forward Detector (FD) to operate at luminosities two orders of magnitude higher than the design luminosity and (b) to convert the CLAS12 FD into a muon detector. In this upgraded configuration, scattered electrons will be detected and identified using a new, compact, $PbWO_4$ electromagnetic calorimeter. Additionally, a new vertex tracking system and a compact central detector will be incorporated to vertex forward-going tracks and measure recoil protons. A preliminary cost estimate for these modifications is approximately 6 million USD.

The beam spin asymmetry in DDVCS will be measured at multiple values of space-like and timelike virtualities of the incoming and outgoing virtual photons, respectively. DDVCS uniquely enables the decoupling of the two variables, x and ξ, allowing access to x independently of ξ and providing valuable new information on Generalized Parton Distributions (GPDs) that is otherwise inaccessible.

In the same reaction, J/ψ electroproduction cross sections as a function of the total center-of-mass energy, W, and the squared transferred momentum, t, at various Q^2 values will be measured. Using an 11 GeV electron beam, our measurement will cover the energy range where the LHCb collaboration has observed charmed pentaquarks. If these pentaquark states exist, they will be formed as s-channel resonances in ep scattering and will be evident in the W distribution. Based on existing theoretical estimates, our experiment will detect a sufficient number of pentaquarks to perform Partial Wave Analysis (PWA) and extract their quantum numbers. Furthermore, analyzing the decay angular distributions of muons will enable the extraction of σ_L/σ_T for the first time near the J/ψ production threshold region.

The proposed measurements will also produce substantial Timelike Compton Scattering (TCS) data. We plan to extend the ongoing CLAS12 TCS program with this new data set, extracting observables such as beam helicity and forward-backward asymmetries in significantly finer kinematic bins than currently possible with existing CLAS12 data.

To accomplish the objectives of this proposal, we request 200 days of beam time for production running at a luminosity of 10^{37} cm^{-2} s^{-1}, 30 days for low-luminosity calibration runs, and 15 days for commissioning the μCLAS12 detector.

[1] D. Mueller, D. Robaschik, B. Geyer, F-M. Dittes, and J. Hořejši. Wave functions, evolution equations and evolution kernels from light-ray operators of QCD. *Fortschritte der Physik/Progress of Physics*, 42(2):101–141, 1994.

[2] X.D. Ji. Deeply virtual Compton scattering. *Phys. Rev. D* **55** *7114*, 1997.

[3] A. V. Radyushkin. Asymmetric gluon distributions and hard diffractive electroproduction. *Phys. Lett. B***385** *333*, 1996.

[4] J.C. Collines, L. Frankfurt, and M. Strikman. Factorization for hard exclusive electroproduction of mesons in qcd. *Phys. Rev. D* **56**, *2982*, 1997.

[5] J. Arrington et al. Physics with cebaf at 12 GeV and future opportunities. *Progress in Particle and Nuclear Physics*, 127:103985, 2022.

[6] S. Stepanyan et al. (CLAS Collaboration). First observation of exclusive deeply virtual compton scattering in polarized electron beam asymmetry measurements. *Phys. Rev. Lett.* **87**, *182002*, 2001.

[7] C. Muñoz Camacho et al. (Hall A Collaboration). Scaling tests of the cross section for deeply virtual compton scattering. *Phys. Rev. Lett.* **97**, *262002*, 2006.

[8] F.-X. Girod et al. (CLAS Collaboration). Deeply Virtual Compton Scattering Beam-Spin Asymmetries. *Phys. Rev. Lett.* **100**, *162002*, 2008.

[9] M. Defurne et al. (Hall A Collaboration). "E00-110 experiment at Jefferson Lab Hall A: Deeply virtual Compton scattering off the proton at 6 GeV". *Phys. Rev. C92 055202*, 2015.

[10] H. S. Jo *et al. (CLAS Collaboration).* "Cross sections for the exclusive photon electroproduction on the proton and Generalized Parton Distributions". *Phys. Rev. Lett* **115** *212003*, 2015.

[11] E. Seder et al. (CLAS Collaboration). Longitudinal Target-Spin Asymmetries for Deeply Virtual Compton Scattering. *Phys. Rev. Lett.* **114** *3*, 2015.

[12] S. Pisano et al. (CLAS Collaboration). Single and double spin asymmetries for deeply virtual Compton scattering measured with CLAS and a longitudinally polarized proton target. *Phys. Rev. D* **91** *052014*, 2015.

[13] F. Georges et al. (Hall A Collaboration). "Deeply Virtual Compton Scattering Cross Section at High Bjorken x_B". *Phys. Rev. Lett.* **128**, *252002*, 2022.

[14] G. Christiaens et al. (CLAS Collaboration). First CLAS12 Measurement of DVCS Beam-Spin Asymmetries in the Extended Valence Region. *Phys. Rev. Lett.* **130**, *211902*, 2023.

[15] E. R. Berger, M. Diehl, and B. Pire. Timelike Compton scattering: exclusive photoproduction of lepton pairs. *Eur. Phys. J. C* **23** *675*, 2002.

[16] A. T. Goritschnig, B. Pire, and J. Wagner. Timelike compton scattering with a linearly polarized photon beam. *Phys. Rev. D* **89**, *094031*, 2014.

[17] M. Boër, M. Guidal, and M. Vanderhaeghen. Timelike compton scattering off the proton and generalized parton distributions. *Eur. Phys. J. A* **51**, *103*,, 2015.

[18] Boër M., Guidal M., and Vanderhaeghen M. Timelike compton scattering off the neutron and generalized parton distributions. *Eur. Phys. J. A* **52** *33*, 2016.

[19] P. Chatagnon et al. (CLAS Collaboration). First-time measurement of timelike compton scattering. *Phys. Rev. Lett.* **127** *262501*, 2021.

[20] H. Moutarde. Extraction of the Compton form factor H from deeply virtual Compton scattering measurements at Jefferson Lab. *Phys. Rev. D* **79***, 094021*, 2009.

[21] B. Berthou et al. PARTONS: PARtonic Tomography Of Nucleon Software. *Eur. Phys. J. C* **78***, 478*, 2009.

[22] V. Bertone et al. Deconvolution problem of deeply virtual compton scattering. *Phys. Rev. D* **103***, 114019*, 2021.

[23] E. Moffat et al. Shedding light on shadow generalized parton distributions. *Phys. Rev. D* **108***, 036027*, 2023.

[24] M. Guidal and M. Vanderhaeghen. Double deeply virtual Compton scattering off the nucleon. *Phys. Rev. Lett.* **90** *012001*, 2003.

[25] A. V. Belitsky and D. Mueller. Exclusive Electroproduction of Lepton Pairs as a Probe of Nucleon Structure. *Phys. Rev. Lett.* **90***, 022001*, 2003.

[26] A. V. Belitsky and D. Mueller. Probing generalized parton distributions with electroproduction of lepton pairs off the nucleon. *Phys. Rev.D* **68***, 116005*, 2003.

[27] V.D. Burkert et al. (CLAS Collaboration). The CLAS12 Spectrometer at Jefferson Laboratory. *Nucl. Inst. and Meth. A*, 959:163419, 2020.

[28] A. Ali et al. (GlueX Collaboration). First measurement of near-threshold j/ψ exclusive photoproduction off the proton. *Phys. Rev. Lett.* **123***, 072001*, 2019.

[29] S. Adhikari et al. (GlueX Collaboration). Measurement of the j/ψ photoproduction cross section over the full near-threshold kinematic region. *Phys. Rev. C* **108***, 025201*, 2023.

[30] B. Duran et al. Determining the gluonic gravitational form factors of the proton. *Nature* **615***, 813*, 2023.

[31] M. Burkardt. Impact parameter dependent parton distributions and off-forward parton distributions for zeta $\rightarrow$ 0. *Phys. Rev. D* **62** *071503 (2000).*

[32] Andrei V. Belitsky, Xiang-dong Ji, and Feng Yuan. Quark imaging in the proton via quantum phase space distributions. *Phys. Rev. D*, 69:074014, 2004.

[33] Xiang-Dong Ji. "Gauge-Invariant Decomposition of Nucleon Spin". *Phys. Rev. Lett.* **78** *610*, 1997.

[34] Xiangdong Ji. Proton mass decomposition: naturalness and interpretations. *Front. Phys. (Beijing)*, 16(6):64601, 2021.

[35] Maxim V. Polyakov and Peter Schweitzer. Forces inside hadrons: pressure, surface tension, mechanical radius, and all that. *Int. J. Mod. Phys. A*, 33(26):1830025, 2018.

[36] V. D. Burkert, L. Elouadrhiri, and F. X. Girod. The pressure distribution inside the proton. *Nature* **557***, 396*, pages 396–399, 2018.

[37] V. D. Burkert, L. Elouadrhiri, F. X. Girod, C. Lorcé, P. Schweitzer, and P. E. Shanahan. Colloquium: Gravitational form factors of the proton. *Rev. Mod. Phys.* **95, 041002**, 2023.

[38] A. Airapetian and et al. (HERMES Collaboration). Measurement of the beam spin azimuthal asymmetry associated with deeply virtual Compton scattering. *Phys. Rev. Lett.* **87***, 182001*, 2001.

[39] A. Airapetian and et al. (HERMES Collaboration). The Beam-charge azimuthal asymmetry and deeply virtual Compton scattering. *Phys. Rev. D* **75***, 011103*, 2007.

[40] A. Aaron and H1 Collaboration et al. Measurement of deeply virtual compton scattering and its t-dependence at hera. *Physics Letters B* **659***, 796*, 2008.

[41] ZEUS collaboration. A measurement of the Q2, W and t dependences of deeply virtual Compton scattering at HERA. *Journal of High Energy Physics* **05***, 108*, 2009.

[42] R. Akhunzyanov and et al. (COMPASS Collaboration). Transverse extension of partons in the proton probed in the sea-quark range by measuring the DVCS cross section. *Physics Letters B* **793***, 188*, 2019.

[43] Kumerički, K. and Müller, Dieter. Description and interpretation of dvcs measurements*. *EPJ Web of Conferences*, 112:01012, 2016.

[44] S. V. Goloskokov and P. Kroll. An attempt to understand exclusive π^+ electroproduction. *The European Physical Journal C*, 65(1):137–151, 2010.

[45] Michel Guidal, Hervé Moutarde, and Marc Vanderhaeghen. Generalized parton distributions in the valence region from deeply virtual compton scattering. *Reports on Progress in Physics* **76, 066202**, 2013.

[46] M. Guidal. A Fitter Code for Deep Virtual Compton Scattering and Generalized Parton Distributions. *Eur. Phys. J. A* **37***, 319*, 2008.

[47] M. Guidal and H. Moutarde. Generalized Parton Distributions from Deeply Virtual Compton Scattering at HERMES. *Eur. Phys. J. A* **42***, 71*, 2009.

[48] M. Guidal. Generalized Parton Distributions from Deep Virtual Compton Scattering at CLAS. *Phys. Lett. B* **689***, 156*, 2010.

[49] M. Guidal. Constraints on the $\tilde{H}$ Generalized Parton Distribution from Deep Virtual Compton Scattering Measured at HERMES. *Phys. Lett. B* **693** *17*, 2010.

[50] K. Kumerički, D. Müller, and M. Murray. HERMES impact for the access of Compton form factors. *Phys. Part. Nucl.* **45***, 723*, 2014.

[51] K. Shiells, Y. Guo, and X. Ji. On extraction of twist-two Compton form factors from DVCS observables through harmonic analysis. *Journal of High Energy Physics* **08***, 048*, 2022.

[52] H. Moutarde, P. Sznajder, and Wagner. Border and skewness functions from a leading order fit to DVCS data. *Eur. Phys. J. C* **78***, 890*, 2018.

[53] K. Kumerički, D. Müller, and K. Passek-Kumerički. Towards a fitting procedure for deeply virtual compton scattering at next-to-leading order and beyond. *Nuclear Physics* **B** *794, 244-323*, 2008.

[54] K. Kumerički and D. Müller. Deeply virtual Compton scattering at small x_B and the access to the

GPD H. *Nucl. Phys. B* **841***, 1*, (2010).

[55] K. Kumerički, D. Müller, and A. Schäfer. Neural network generated parametrizations of deeply virtual Compton form factors. *J. High Energ. Phys, 73*, 2011.

[56] H. Moutarde, P. Sznajder, and Wagner. Unbiased determination of DVCS Compton form factors. *Eur. Phys. J. C* **79***, 614*, 2019.

[57] M. Čuić, K. Kumerički, and A. Schäfer. Separation of quark flavors using deeply virtual compton scattering data. *Phys. Rev. Lett.* **125***, 232005 (2020).*

[58] V. Guzey and T. Teckentrup. Dual parametrization of the proton generalized parton distribution functions H and E, and description of the deeply virtual Compton scattering cross sections and asymmetries. *Phys. Rev. D* **74, 054027**, Sep 2006.

[59] M. Constantinou. The x-dependence of hadronic parton distributions: A review on the progress of lattice QCD. *Eur. Phys. J. A* **57***, 77*, 2021.

[60] A.V. Belitsky, D. Müller, and A. Kirchner. Theory of deeply virtual Compton scattering on the nucleon. *Nuclear Physics* **B** *629, 323*, 2002.

[61] S. Zhao, A. Camsonne, D. Marchand, M. Mazouz, N. Sparveris, S. Stepanyan, E. Voutier, and Z. W. Zhao. Double deeply virtual Compton scattering with positron beams at SoLID. *The European Physical Journal* **A** *57, 240*, 2021.

[62] K. Deja, V. Martínez-Fernández, B. Pire, P. Sznajder, and J. Wagner. Phenomenology of double deeply virtual compton scattering in the era of new experiments. *Phys. Rev. D*, 107:094035, May 2023.

[63] J. S. Alvarado, M. Hoballah, and E. Voutier. Sensitivity of Double Deeply Virtual Compton Scattering observables to Generalized Parton Distributions, 2025.

[64] D. Kharzeev, H. Satz, A. Syamtomov, and G. Zinovjev. J/ψ-photoproduction and the gluon structure of the nucleon. *Nuclear Physics A*, 661(1):568–572, 1999.

[65] Yoshitaka Hatta, Abha Rajan, and Di-Lun Yang. Near threshold j/ψ and Υ photoproduction at jlab and rhic. *Phys. Rev. D*, 100:014032, Jul 2019.

[66] Yuxun Guo, Xiangdong Ji, and Yizhuang Liu. Qcd analysis of near-threshold photon-proton production of heavy quarkonium. *Phys. Rev. D*, 103:096010, May 2021.

[67] Dmitri E. Kharzeev. Mass radius of the proton. *Phys. Rev. D*, 104:054015, Sep 2021.

[68] Kiminad A. Mamo and Ismail Zahed. J/ψ near threshold in holographic QCD: A and D gravitational form factors. *Phys. Rev. D*, 106(8):086004, 2022.

[69] Yuxun Guo, Xiangdong Ji, Yizhuang Liu, and Jinghong Yang. Updated analysis of near-threshold heavy quarkonium production for probe of proton's gluonic gravitational form factors. *Phys. Rev. D*, 108(3):034003, 2023.

[70] I. Yu. Kobzarev and L. B. Okun. GRAVITATIONAL INTERACTION OF FERMIONS. *Zh. Eksp. Teor. Fiz.*, 43:1904–1909, 1962.

[71] Heinz Pagels. Energy-Momentum Structure Form Factors of Particles. *Phys. Rev.*, 144:1250–1260,

1966.

[72] P. E. Shanahan and W. Detmold. Gluon gravitational form factors of the nucleon and the pion from lattice QCD. *Phys. Rev. D*, 99(1):014511, 2019.

[73] Dimitra A. Pefkou, Daniel C. Hackett, and Phiala E. Shanahan. Gluon gravitational structure of hadrons of different spin. *Phys. Rev. D*, 105(5):054509, 2022.

[74] Daniel C. Hackett, Dimitra A. Pefkou, and Phiala E. Shanahan. Gravitational Form Factors of the Proton from Lattice QCD. *Phys. Rev. Lett.*, 132(25):251904, 2024.

[75] Cédric Lorcé, Andreas Metz, Barbara Pasquini, and Simone Rodini. Energy-momentum tensor in QCD: nucleon mass decomposition and mechanical equilibrium. *JHEP*, 11:121, 2021.

[76] V. D. Burkert, L. Elouadrhiri, F. X. Girod, C. Lorcé, P. Schweitzer, and P. E. Shanahan. Colloquium: Gravitational form factors of the proton. *Rev. Mod. Phys.*, 95(4):041002, 2023.

[77] S. Chekanov et al. Exclusive photoproduction of J / psi mesons at HERA. *Eur. Phys. J.*, C24:345–360, 2002.

[78] C. Alexa et al. Elastic and Proton-Dissociative Photoproduction of J/psi Mesons at HERA. *Eur. Phys. J. C*, 73(6):2466, 2013.

[79] P. A. Adderley et al. The Continuous Electron Beam Accelerator Facility at 12 GeV. *Phys. Rev. Accel. Beams*, 27(8):084802, 2024.

[80] S. Adhikari et al. Measurement of the j/ψ photoproduction cross section over the full near-threshold kinematic region. *Phys. Rev. C*, 108:025201, Aug 2023.

[81] B. Duran, Z.-E. Meziani, S. Joosten, et al. Determining the gluonic gravitational form factors of the proton. *Nature*, 615(7954):813–816, Mar 2023.

[82] Kazuhiro Tanaka. Three-loop formula for quark and gluon contributions to the QCD trace anomaly. *JHEP*, 01:120, 2019.

[83] Kazuhiro Tanaka. Twist-four gravitational form factor at NNLO QCD from trace anomaly constraints. *JHEP*, 03:013, 2023.

[84] Kiminad A. Mamo and Ismail Zahed. Electroproduction of heavy vector mesons using holographic qcd: From near threshold to high energy regimes. *Phys. Rev. D*, 104:066023, Sep 2021.

[85] Kiminad A. Mamo and Ismail Zahed. Diffractive photoproduction of j/ψ and Υ using holographic qcd: Gravitational form factors and gpd of gluons in the proton. *Phys. Rev. D*, 101:086003, Apr 2020.

[86] Kiminad A. Mamo and Ismail Zahed. Nucleon mass radii and distribution: Holographic qcd, lattice qcd, and gluex data. *Phys. Rev. D*, 103:094010, May 2021.

[87] Zein-Eddine Meziani. Gluonic gravitational form factors of the proton, 2024.

[88] Meng-Lin Du, Vadim Baru, Feng-Kun Guo, Christoph Hanhart, Ulf-G Meißner, Alexey Nefediev, and Igor Strakovsky. Deciphering the mechanism of near-threshold J/ψ photoproduction. *Eur. Phys. J. C*, 80(11):1053, 2020.

[89] D. Winney, C. Fernández-Ramírez, A. Pilloni, A. N. Hiller Blin, M. Albaladejo, Ł. Bibrzycki, N. Hammoud, J. Liao, V. Mathieu, G. Montaña, R. J. Perry, V. Shastry, W. A. Smith, and A. P. Szczepaniak.

Dynamics in near-threshold j/ψ photoproduction. *Phys. Rev. D*, 108:054018, Sep 2023.

[90] Michael I. Eides, Victor Yu. Petrov, and Maxim V. Polyakov. Narrow nucleon-$\psi(2S)$ bound state and LHCb pentaquarks. *Phys. Rev.*, D93(5):054039, 2016.

[91] V. Kubarovsky and M. B. Voloshin. Formation of hidden-charm pentaquarks in photon-nucleon collisions. *Phys. Rev.*, D92(3):031502, 2015.

[92] Feng-Kun Guo, Ulf-G. Meißner, Wei Wang, and Zhi Yang. How to reveal the exotic nature of the $P_c(4450)$. *Phys. Rev.*, D92(7):071502, 2015.

[93] A. N. Hiller Blin, C. Fernández-Ramírez, A. Jackura, V. Mathieu, V. I. Mokeev, A. Pilloni, and A. P. Szczepaniak. Studying the $P_c(4450)$ resonance in $J\psi$ photoproduction off protons. *Phys. Rev.*, D94(3):034002, 2016.

[94] Igor Strakovsky, William J. Briscoe, Eugene Chudakov, Ilya Larin, Lubomir Pentchev, Axel Schmidt, and Ronald L. Workman. Plausibility of the LHCb Pc in the GlueX total cross sections. *Phys. Rev. C*, 108(1):015202, 2023.

[95] M. Ungaro. The CLAS12 Geant4 simulation. *Nuclear Instruments and Methods in Physics Research Section A: Accelerators, Spectrometers, Detectors and Associated Equipment*, 959:163422, 2020.

[96] M. Tenorio-Pita. Enhancing Lepton Identification in CLAS12 using Machine Learning Techniques. *CLAS-NOTE 2024-005*, 2004.

[97] V Ziegler and et al. The CLAS12 software framework and event reconstruction. *Nuclear Instruments and Methods in Physics Research Section A: Accelerators, Spectrometers, Detectors and Associated Equipment*, 959:163472, 2020.

[98] R. Niyazov and S. Stepanyan. *CLAS-NOTE 2005-021 (2005).*

[99] I Balossino and et al. The hps electromagnetic calorimeter. *Nuclear Instruments and Methods in Physics Research Section A: Accelerators, Spectrometers, Detectors and Associated Equipment*, 854:89–99, 2017.

[100] A. Acker and et al. The clas12 forward tagger. *Nuclear Instruments and Methods in Physics Research Section A: Accelerators, Spectrometers, Detectors and Associated Equipment*, 959:163475, 2020.

[101] Tanja Horn and (forthe JLab Neutral Particle Spectrometer Collaboration). *Journal of Physics: Conference Series*, 587(1):012048, feb 2015.

[102] A Asaturyan and et al. Electromagnetic calorimeters based on scintillating lead tungstate crystals for experiments at jefferson lab. *Nuclear Instruments and Methods in Physics Research Section A: Accelerators, Spectrometers, Detectors and Associated Equipment*, 1013:165683, 2021.

[103] F. Sauli. Gem: A new concept for electron amplification in gas detectors. *Nuclear Instruments and Methods in Physics Research Section A: Accelerators, Spectrometers, Detectors and Associated Equipment*, 386(2):531–534, 1997.

[104] H. Fenker et al. BoNuS: Development and Use of a Radial TPC Using Cylindrical GEMs. *Nucl. Inst. and Meth. A 592, 273 (2008).*

[105] R Dupré and et al. A radial time projection chamber for α detection in CLAS at JLab. *Nuclear*

Instruments and Methods in Physics Research Section A: Accelerators, Spectrometers, Detectors and Associated Equipment, 898:90–97, 2018.

[106] K. Gnanvo et al. https://wiki.jlab.org/pcrewiki/images/f/ff/KG_pRadReadinessReview_20160325.pdf.

[107] K. Gnanvo. *https://indico.cern.ch/event/1110129/contributions/4714241/attachments/2386731/4079118/KG_RD51_MiniWeek20210208.pdf*, 2024.

[108] C. Altunbas, M. CapÃ©ans, K. Dehmelt, J. Ehlers, J. Friedrich, I. Konorov, A. Gandi, S. Kappler, B. Ketzer, R. De Oliveira, S. Paul, A. Placci, L. Ropelewski, F. Sauli, F. Simon, and M. van Stenis. "Construction, test and commissioning of the triple-gem tracking detector for compass". *Nucl. Instrum. Meth.*, A490(1):177 – 203, 2002.

[109] K. Gnanvo and et *al.* "Performance in test beam of a large-area and light-weight GEM detector with 2D stereo-angle (UV) strip readout". *Nucl. Instrum. Meth.*, A808:83–92, 2016.

[110] G. Bencivenni, R. De Oliveira, G. Morello, and M. Poli Lener. The micro-Resistive WELL detector: a compact spark-protected single amplification-stage MPGD. *JINST*, 10(02):P02008, 2015.

[111] G. Bencivenni et al. The μ-RWELL for future HEP challenges. *Nucl. Instrum. Meth. A*, 1069:169725, 2024.

[112] Marcus Hohlmann Pietro Iapozzuto. Design, prototyping, and construction of a cylindrical µ resistive-well detector.

[113] Tetsuo Abe. GRAPE dilepton (Version1.1): A Generator for dilepton production in e p collisions. *Comput. Phys. Commun.*, 136:126–147, 2001.

[114] Valery Klimenko et all. Inclusive electron generator. `https://github.com/ValeriiKlimenko/IncEG/tree/master`.

[115] V. Klimenko et al. Inclusive Electron Scattering in the Resonance Region off a Hydrogen Target with CLAS12. 1 2025.

[116] Tetsuo Abe. GRAPE-Dilepton (version1.1), A Generator for Dilepton Production in ep Collisions. *arXiv:hep-ph/0012029.*

[117] M. Vanderhaeghen, P.A.M. Guichon, and M. Guidal. Deeply virtual electroproduction of photons and mesons on the nucleon: Leading order amplitudes and power corrections. *Phys. Rev. D* **60***, 094017 (1999).*

[118] *https://drf-gitlab.cea.fr/partons/core/partons.*

[119] D. Winney, C. Fanelli, A. Pilloni, A. N. Hiller Blin, C. Fernández-Ramírez, M. Albaladejo, V. Mathieu, V. I. Mokeev, and A. P. Szczepaniak. Double polarization observables in pentaquark photoproduction. *Phys. Rev. D*, 100:034019, Aug 2019.

[120] Derek Glazier. The elspectro generator. https://github.com/dglazier/elSpectro.

[121] K. Schilling and G. Wolf. *Nucl. Phys.* **B 61***, 381 (1973).*

[122] LHCb collaboration R. Aaij et al. *Phys. Rev. Lett. 115, 072001 (2015).*

[123] Q. Wang, X.-H. Liu, and Q. Zhao. *Phys. Rev. D92, 034022 (2015).*

[124] Marek Karliner and Jonathan L. Rosner. Photoproduction of Exotic Baryon Resonances. *Phys. Lett.*,

B752:329–332, 2016.

[125] Haakon Olsen and L. C. Maximon. Photon and electron polarization in high-energy bremsstrahlung and pair production with screening. *Phys. Rev.*, 114:887–904, May 1959.